

**Studies on the rare earth elements- and calcium-
dependent quinoproteins in *Pseudomonas putida* KT2440**

Dissertation

zur Erlangung des Grades eines

Doktor der Naturwissenschaften

(Dr. rer.nat.)

des Fachbereichs Chemie der Philipps-Universität Marburg

Vorgelegt von

Eslam Mohsen Ahmed Gabr, Elsayed

Master of pharmaceutical sciences (Microbiology and Immunology), Msc.
(Pharmacy).

Aus Gizeh, Ägypten

Marburg, 2021

Die Untersuchungen zur vorliegenden Arbeit wurden von 2018 bis 2021 am LOEWE Zentrum für synthetische Mikrobiologie (SYNMIKRO) der Philipps-Universität Marburg unter der Leitung von Prof. Dr. Gert Bange durchgeführt.

Vom Fachbereich Chemie

der Philipps-Universität Marburg (Hochschulkennziffer 1180)

als Dissertation am _____ angenommen.

Erstgutachter: Prof. Dr. Gert Bange

(Fachbereich Chemie der Philipps-Universität Marburg)

Zweitgutachter: Prof. Dr. Peter Graumann

(Fachbereich Chemie der Philipps-Universität Marburg)

Tag der Einreichung:

Tag der Disputation:

Statutory Declaration

I hereby declare that this work is entirely of my own except where due to acknowledgement explicitly stated and to the best of my knowledge has not been submitted, either in part or as a whole, to this or any other educational institution in fulfilment of an academic degree. I declare that no other sources or references except those stated were used in this work.

Elsayed, Eslam Mohsen Ahmed Gabr

Marburg,

Eidesstattliche Erklärung

Ich erkläre, dass eine Promotion noch an keiner anderen Hochschule als der Philipps-Universität Marburg, Fachbereich Chemie, versucht wurde.

Ich versichere, dass ich die hier vorgelegte Dissertation selbst und ohne fremde Hilfe verfasst, keine anderen als die angegebenen Quellen oder Hilfsmittel benutzt, alle vollständig oder sinngemäß übernommenen Zitate als solche gekennzeichnet sowie die Dissertation in der vorliegenden oder einer ähnlichen Form noch bei keiner anderen in- oder ausländischen Hochschule im Rahmen eines Promotionsgesuches oder zu anderen Prüfungszwecken eingereicht habe.

Elsayed, Eslam Mohsen Ahmed Gabr

Marburg,

Acknowledgements

I am very grateful for people made this work possible.

First and foremost, I would like to express my deepest gratitude to **Prof. Dr. Gert Bange** for providing me the opportunity to conduct my doctoral studies in his laboratory. I am very grateful for everything, most importantly for having patience along this lengthy journey to the finish line, for finding encouraging words through many inspiring discussions, Gert gave me many insights into science and beyond.

I am incredibly grateful for **Yousef Jameel Foundation**, such an inspiring agency that funded my Ph.D. studies. I was always proud to be granted such a prestigious program. I would be forever grateful for this opportunity.

I would like to thank **Dr. Alexander Lepak** for many fruitful discussions on various parts of this work. Your cooperation and support are very much appreciated.

I am grateful to **Dr. Wieland Steinchen** for his help with the HDX experiments, its data evaluation and many nice conversations.

I would like to express my gratitude to **Dr. Sven Freibert** who introduced me to analytical aspects of microscale thermophoresis and participated in its data evaluation.

Furthermore, I would like to thank **Dr. Florian Weigend** and **Kevin Reiter** for their support on the quantum chemical calculations of PedH and PedE.

Special thanks for **Dr. Janosch Klebensberger**, **Matthias Wehrmann**, **Sebastian Köbbing**, and **Prof. Dr. Nick Wierckx** for their collaboration on protein engineering of PedH.

Moreover, I am grateful to all former and present members of the **Bange laboratory**. Mainly, I would like to thank Dr. Florian Altegoer and Nils Mais for introducing me into structural biology. Moreover, I am thankful for Dr. Jan Pane-Farre, Mohamed, Gregor, Patty, Pietro, Cyndia, Itzel and Galina for the collaborative atmosphere over the last years and many happy hours in the lab and outside.

Most of all, I am deeply indebted to **my family and my friends** who have been a continuous support throughout my Ph.D. My father, **Mohsen** who passed away 4 months after starting my doctoral studies and literally was dreaming day and night witnessing me a Dr. rer. nat. He did everything he could to support me, with love. My mother, my brother and my sisters who never stopped believing in me.

I am especially grateful to my wife, **Hanan**, for her patience and constant support. My Kids, **Aser**, **Asil**, and **Malak**, whose smiles are always cheering me up. I enjoy being with you every day.

I have survived things I have never thought I could get through. I am proud of myself and I hope made you all proud of me.

Summary

Rare-earth elements (REEs) have long been believed to play a crucial role in a wide variety of several modern technologies, but insignificant roles for biological processes. In recent days, a growing body of evidence shows a variety of enzymes with REEs-dependent activities. For example, the soil-dwelling bacterium *Pseudomonas putida* KT2440 employs the REEs-dependent alcohol dehydrogenase (ADH), PedH (PP_2679), in order to degrade plant-, fungal-, and bacteria-derived volatiles. Mechanistically, PedH resides in the periplasm of *P. putida* and exhibits activity on a similar set of substrates as its strictly calcium-dependent counterpart PedE (PP_2674). As members of quinoproteins family, both enzymes strictly rely on the redox cofactor pyrroloquinoline quinone (PQQ), which plays an essential role in direct electron transfer towards a c-type cytochrome in the electron transport chain for bacterial ATP synthesis during the periplasmic oxidation process.

There is no clear evidence till now why PedH could be REEs-dependent in its ADH activity while its counterpart PedE utilizes calcium to perform the same function. In the first part of this work, I have tried to get in-depth insights into the structural and mechanistic characterization of PedE and PedH. Structure analysis clearly showed that an aspartate amino acid residue (D325PedH) plays a significant role in the optimization of PedH towards the REEs-dependence. The functional analysis of both ADHs revealed that both enzymes use a cognate c-type cytochrome (PedF) in their periplasmic oxidation process where the REEs-dependent PedH has more catalytical efficiency compared to the calcium-dependent PedE. Intriguingly, my data showed that a molecular switch could be in charge of an adaptive mechanism of PedH towards calcium-dependence.

On the other hand, understanding the structure and mechanistic background of PedH enables me in collaboration with 2 research groups to engineer PedH as a novel tool for biocatalysis in the second part of this work. In our publication,

PedH has been established for a biosynthetic pathway of 2,5-furandicarboxylic acid (FDCA), one of the top 12 value-added renewable chemicals that provides a promising alternative to the petroleum-based terephthalic acid to produce polymers, to reach the goal of net-zero greenhouse gas emissions.

Zusammenfassung

Es wird seit langem angenommen, dass Metalle der Seltenen Erden (MSE) eine entscheidende Rolle in einer Vielzahl verschiedener moderner Technologien spielen, für biologische Prozesse jedoch eine unbedeutende Rolle spielen. In den letzten Tagen zeigen immer mehr Beweise eine Vielzahl von Enzymen mit MSE-abhängigen Aktivitäten. Beispielsweise verwendet das bodenbewohnende Bakterium *Pseudomonas putida* KT2440 die MSE-abhängige Alkoholdehydrogenase (ADH) PedH (PP_2679), um von Pflanzen, Pilzen und Bakterien stammende flüchtige Stoffe abzubauen. Mechanistisch gesehen befindet sich PedH im Periplasma von *P. putida* und zeigt Aktivität auf einem ähnlichen Satz von Substraten wie sein streng calcium-abhängiges Gegenstück PedE (PP_2674). Als Mitglieder der Chinoproteinfamilie stützen sich beide Enzyme streng auf den Redox-Cofaktor Pyrrolochinolinchinon (PQQ), der eine wesentliche Rolle beim direkten Elektronentransfer zu einem Cytochrom vom c-Typ in der Elektronentransportkette für die bakterielle ATP-Synthese während des periplasmatischen Oxidationsprozesses spielt.

Bisher gibt es keine eindeutigen Beweise dafür, warum PedH in seiner ADH-Aktivität REEs-abhängig sein könnte, während sein Gegenstück PedE Calcium verwendet, um dieselbe Funktion auszuführen. Im ersten Teil dieser Arbeit habe ich versucht, detaillierte Einblicke in die strukturelle und mechanistische Charakterisierung von PedE und PedH zu erhalten. Die Strukturanalyse zeigte deutlich, dass ein Aspartat-Aminosäurerest (D325PedH) eine signifikante Rolle bei der Optimierung von PedH in Richtung der REEs-Abhängigkeit spielt. Die Funktionsanalyse beider ADHs ergab, dass beide Enzyme in ihrem periplasmatischen Oxidationsprozess ein verwandtes Cytochrom vom c-Typ (PedF) verwenden, bei dem das REEs-abhängige PedH im Vergleich zum calciumabhängigen PedE eine höhere katalytische Effizienz aufweist. Interessanterweise zeigten meine Daten, dass ein molekularer Schalter für

einen adaptiven Mechanismus von PedH zur Calciumabhängigkeit verantwortlich sein könnte.

Andererseits ermöglicht mir das Verständnis der Struktur und des mechanistischen Hintergrunds von PedH in Zusammenarbeit mit zwei Forschungsgruppen, PedH als neuartiges Werkzeug für die Biokatalyse im zweiten Teil dieser Arbeit zu entwickeln. In unserer Veröffentlichung wurde PedH für einen Biosyntheseweg von 2,5-Furandicarbonsäure (FDCA) etabliert, einer der 12 wichtigsten erneuerbaren Chemikalien mit Mehrwert, die eine vielversprechende Alternative zur Terephthalsäure auf Erdölbasis zur Herstellung von Polymeren darstellen. Das Ziel der Netto-Null-Treibhausgasemissionen zu erreichen.

Publications

Parts of the work presented here are published or are in the process of publishing:

Eslam M. Elsayed,[#] Matthias Wehrmann,[#] Sebastian Köbbing, Laura Bendz, Alexander Lepak, Johannes Schwabe, Nick Wierckx, Janosch Klebensberger*, and Gert Bange*. Engineered PQQ-Dependent Alcohol Dehydrogenase for the Oxidation of 5-(Hydroxymethyl)furoic Acid”. ***ACS Catalysis***; **2020**, 10, 7836–7842. <https://doi.org/10.1021/acscatal.0c01789> # Equally contributing authors.

Eslam M. Elsayed, Steinchen W., Kevin Reiter, Sven A. Freibert, Florian Weigend, Alexander Lepak, and Gert Bange. A molecular switch mediates adaptability of rare earth element-dependent alcohol dehydrogenases. ***In preparation***.

Troitsch A, Loi V, Zühlke D, Lalk M, Methling K, Riedel K, Bernhardt J, **Elsayed E. M.**, Bange G, Antelmann H, Pane-Farre J. Carbon source-dependent reprogramming of anaerobic metabolism in *Staphylococcus aureus*. ***Journal of Bacteriology***; (2021). JB.00639-20. DOI: [10.1128/JB.00639-20](https://doi.org/10.1128/JB.00639-20)

Table of Contents

Acknowledgements	VIII
Summary	X
Zusammenfassung	XII
Publications	XIV
Table of Contents	XV
Abbreviations	XIX
List of Figures	XXII
List of Tables	XXIV
Part I. Structural and mechanistic investigation of the rare earth elements- and calcium- dependent quinoproteins in <i>Pseudomonas putida</i> KT2440	1
1. Introduction	2
1.1. Rare earth elements (REEs) are misunderstood.	2
1.1.1. Rare earth elements are not rare.	2
1.1.2. Rare earth elements are not biologically inert.	6
1.1.2.1. Ionic radii of early rare earth elements mimic the ionic radius of calcium, the common biological cofactor.	6
1.1.2.2. Biological role of rare earth elements has been established over the last decade.	8
1.2. <i>Pseudomonas putida</i> is a REEs-utilizing bacterium.	10
1.2.1. <i>Pseudomonas putida</i> is a ubiquitous rhizosphere soil colonizer.	10
1.2.2. Pyrroloquinoline quinone (PQQ)-dependent alcohol dehydrogenases (ADHs) in <i>P. putida</i>	11
1.2.2.1. PQQ is a redox cofactor.	11
1.2.2.2. Proposed mechanisms of PQQ-ADHs	12
1.2.2.3. <i>P. putida</i> expresses 2 different enzymes of the subclass Type I PQQ-ADHs on the same operon with a different metal cofactor.	16
2. Aim of the work.	18
3. Results	19
3.1. Structural analysis of PedE and PedH	19
3.1.1. Purification of PedE and PedH	19

3.1.2. Microscale thermophoresis (MST) of PedE and PedH to different metals.....	22
3.1.3. Crystallization of PedH and PedE	24
3.1.4. Crystal structures of PedE and PedH.....	25
3.1.4.1. PedE and PedH arranged in a propeller-like style.....	28
3.1.4.2. PQQ locates in the center of the active site.....	31
3.1.4.3. Substrate cavity of the active site.....	33
3.1.4.4. Metal ion coordination of PedE and PedH	34
3.2. Functional analysis of PQQ/ADHs	35
3.2.1. PedF is the cognate cytochrome for PedE and PedH.....	35
3.2.1.1. <i>Ped</i> operon has a putative cytochrome-encoding gene (PedF).35	
3.2.1.2. Purification of the c-type cytochrome PedF	36
3.2.1.3. Microscale thermophoresis of PedF towards PedE and PedH..	39
3.2.1.4. Activity measurement of PedE and PedH using PedF as their natural c-type cytochrome.....	39
3.2.2. Kinetics of PedH and PedE towards ethanol as a substrate.....	41
3.2.3. The REEs-dependent PedH can use calcium as a metal cofactor ..	42
3.2.3.1. Crystallization of PedH in presence of calcium shows an active site glutamate switch	44
3.2.3.2. Quantum chemical calculations explain the orientation preference of PedH depending on the metal cofactor.....	48
3.2.3.3. PedH molecular switch changes its electrostatic surface charge at the binding interface with PedF	53
3.2.3.3.1. Change of PedH electrostatic surface charge at the disulfide bridge side.....	53
3.2.3.3.2. The disulfide bridge side of PedH represents the PedH/PedF binding interface.....	55
3.2.3.3.3. Different patterns of PedH/PedF binding depending on the metal cofactor.....	62
3.2.4. Metal dependency and activity of PedE and PedH can be switched.....	64
4. Discussion and Conclusion	67
4.1. REEs-dependent PedH has an extra coordinating residue “D325” completes the geometry required for Ln ⁺³ coordination.	67

4.2. The REEs-dependent PedH has better catalytic efficiency than its Ca-dependent PedE	69
4.3. Molecular switch defines the adaptability of PedH towards the calcium dependent activity.....	71
5. Materials and Methods	76
5.1. Materials	76
5.1.1. Chemicals and consumables	76
5.1.2. Enzymes and cloning equipment	76
5.1.3. Bacterial strains and plasmids.....	76
5.1.3.1. Oligonucleotides.....	76
5.1.3.2. Plasmids.....	77
5.1.3.3. Strains	77
5.1.4. Growth media and buffers	77
5.1.4.1. Growth media	77
5.1.4.2. Antibiotics	77
5.1.4.3. Buffers for protein purification	78
5.1.4.4. Buffers for HDX	79
5.1.4.5. Buffers for agarose gel electrophoresis	79
5.1.4.6. Buffers for sodium dodecyl sulfate polyacrylamide gel electrophoresis (SDS-PAGE).....	80
5.1.5. Protein biochemistry.....	81
5.1.6. Laboratory equipment	82
5.2. Methods.....	84
5.2.1. Molecular cloning.	84
5.2.2. Purification of PedE and PedH.....	86
5.2.3. Protein production and purification for PedF.....	87
5.2.4. SDS-PAGE	88
5.2.5. Heme staining of PedF SDS-PAGE	88
5.2.6. Structural biology.....	89
5.2.6.1. Crystallization	89
5.2.6.2. Data processing and refinement	89
5.2.7. The ferricyanide reductase Kinetics assay.....	90
5.2.8. Quantum chemical computational analysis.....	91

5.2.9. Measurements of affinity in terms of dissociation constants (K_d) by microscale thermophoresis (MST).....	91
5.2.10. Hydrogen-Deuterium Exchange Mass Spectrometry (HDX-MS) ..	92
6. References.....	94
7. Appendix.....	105
7.1. Supporting tables.....	105
7.2. Supporting Figures	109
Part II. Engineered PQQ-Dependent Alcohol Dehydrogenase for the Oxidation of 5-(Hydroxymethyl)furoic Acid.....	114
1. Scientific contribution report.....	115
1.1. Abstract.....	115
1.2. Author contributions	116
2. Publication.....	117
3. Supporting information	S1

Abbreviations

Standardized abbreviations for chemical symbols, SI units and one- or three-letter codes for amino acids are used without further reference. Abbreviations for bacterial species are given in the text. All other abbreviations employed in this work are listed:

Å	Ångström (10^{-10} m)
ADP	Adenosine diphosphate
ADHs	alcohol dehydrogenases
Amp	Ampicillin
ATP	Adenosine triphosphate
AU	Absorption unit
bp	Base pairs
Ca	Calcium
Ca ⁺²	Calcium ion
CV	Column volume
Cm	chloramphenicol
CNs	coordination numbers
COSMO	conductor-like screening model
Da	Dalton (1.660538×10^{-27} kg)
DAB	3,3'-diaminobenzidine tetra-hydrochloride
ddH ₂ O	double-distilled water
DMSO	Dimethyl sulfoxide
DNA	Deoxyribonucleic acid
dNTP	Desoxynucleoside triphosphate
e ⁻	electron
<i>E. coli</i>	<i>Escherichia coli</i>
ECPs	effective core potentials
EDTA	Ethylenediaminetetraacetic acid
ESRF	European Synchrotron Radiation Facility
<i>et al.</i>	<i>et alia</i> ; and others

FDCA	furan-2,5-dicarboxylic acid
FFA	5-formylfuroic acid
FFF	5-(formyl)furfural
hr	Hours
HDX	Hydrogen deuterium ($^1\text{H}/^2\text{H}$) exchange
HDXMS	$^1\text{H}/^2\text{H}$ exchange mass spectrometry
HEPES	4-(2-hydroxyethyl)-1-piperazineethanesulfonic acid
His ₆	Hexahistidine
HMF	5-(hydroxymethyl)furfural
HMFA	5-(hydroxymethyl)furoic acid
HPLC	High Performance Liquid Chromatography
IPTG	Isopropyl- β -D-1-thiogalactopyranoside
IMAC	immobilized metal affinity chromatography
K _d	dissociation constant
K _m	Michaelis constant
Kan	Kanamycin
LB	Lysogeny broth
Ln	Lanthanides or Lanthanoids
Ln ⁺³	Lanthanide ion
MDH	methanol dehydrogenase
MR	Molecular replacement
MS	Mass spectrometry
MST	Microscale thermophoresis
MW	Molecular weight
NAD	β -1,4-nicotinamide adeninedinucleotide
NADP	β -1,4-nicotinamide adeninedinucleotide phosphate
Nd	Neodymium
Ni-NTA	nickel-nitrilotriacetic acid
NTP	Nucleoside triphosphates
OD	Optical density
PAGE	Polyacrylamide gel electrophoresis
PCR	Polymerase chain reaction
PDB	Protein database

PEG	Polyethylene glycol
PEG 2000 MME	Polyethylene glycol monomethyl ether 2000
pH	'potential of hydrogen' or 'power of hydrogen'
<i>P. putida</i>	<i>Pseudomonas putida</i>
PQQ	pyrroloquinoline quinone
PQQ-ADHs	pyrroloquinoline quinone alcohol dehydrogenases
PQQH ₂	Reduced form of pyrroloquinoline quinone
REEs	Rare earth elements
S	Seconds
SDS	Sodium dodecyl sulfate
SDS-PAGE	Sodium dodecyl sulfate polyacrylamide gel electrophoresis
SEC	Size exclusion chromatography
TEMED	Tetramethylethylenediamine
TBE	Tris/Borate/EDTA
TRIS	Tris(hydroxymethyl)aminomethane
V_{\max}	Maximal velocity
UV	Ultraviolet
wt	wild type
λ	lambda / wavelength
σ	Sigma

List of Figures

Figure 1. Rare earth elements and their atomic numbers as shown in Mendeleev's Periodic table.....	3
Figure 2. Abundance of elements in the earth's crust.	5
Figure 3. Lanthanide contraction and ionic radii of REEs.....	8
Figure 4. Structure of pyrroloquinoline quinone (PQQ).	12
Figure 5. Periplasmic oxidation of alcohols by PQQ-ADHs for energy production process.	13
Figure 6. Proposed mechanisms of quinoproteins for alcohol oxidation..	15
Figure 7. Ped gene cluster involved in volatiles oxidation of <i>P. putida</i> ...16	
Figure 8. Immobilized metal affinity chromatography (IMAC) and size-exclusion chromatography (SEC) of PedE (A-D) and PedH (E-H).....	21
Figure 9. Binding affinity of PedE towards calcium using microscale thermophoresis (MST).....	22
Figure 10. Binding affinity of PedH towards different lanthanides.....	23
Figure 11. Crystals of PedE and PedH.....	25
Figure 12. Alignment and overall architecture of PedH and PedE..	29
Figure 13. Interactions stabilizing the β -propeller structure of PedH.....	30
Figure 14. Coordination of PQQ in active site of PedE and PedH.	32
Figure 15. Substrate cavity of PedH.....	33
Figure 16. Comparison of the metal ion coordination in PedE (colored cyan) and PedH (colored brown).....	34
Figure 17. Purification of PedF.	38
Figure 18. Binding affinity of PedF towards PedE (A) and PedH (B) using MST.	39
Figure 19. Graphic explanation of the kinetic characterization of PQQ-ADHs using their natural cytochrome PedF as electron acceptor.	40
Figure 20. Activity measurements of PedE and PedH using PedF as their natural c-type cytochrome.	41
Figure 21. kinetic parameters and catalytic efficiency of PedE and PedH towards ethanol.	42

Figure 22. MST and specific activity of PedH and PedE in different metal conditions.....	44
Figure 23. Comparison of different metal ion coordination in the active site of PedE and PedH.....	48
Figure 24. Models for the active centers of PedH (top row) and PedE (bottom row).....	51
Figure 25. PedH molecular switch changes its electrostatic surface charge at the binding interface with PedF.	54
Figure 26. HDX-MS of PedF..	57
Figure 27. The binding interface of PedF in the PedF/PedH complex.	58
Figure 28. HDX-MS of PedH.....	59
Figure 29. Conformational changes of PedH in the PedF/PedH complex. ..	60
Figure 30. Expected topology of the PedF/PedH complex.	61
Figure 31. Binding affinity of PedH and PedH_C132S variant towards PedF in different metal conditions using MST.	63
Figure 32. Metal Dependency and Activity of ADHs can be switched.....	66
Figure S 1. Relative HDX of PedH.....	109
Figure S 2. Difference in HDX between PedH/PedF and PedH alone..	110
Figure S 3. Relative HDX of PedF.	111
Figure S 4. Difference in HDX between PedH/PedF and PedF alone.....	112
Figure S 5. Binding affinity of PedH and PedE variants towards calcium (Ca) and Neodymium (Nd) using MS	113

List of Tables

Table 1. Different crystallization conditions of PedE and PedH.....	24
Table 2. Data collection and refinement statistics of PedH in presence of La, Ce, and Pr.....	26
Table 3. Data collection and refinement statistics of PedH in presence of Nd and PedE in presence of Ca.....	27
Table 4. Data collection and refinement statistics of PedH in presence of Ca.	47
Table 5. Energy differences ΔE between the two orientations of the glutamate (E199PedH/E195PedE) unit for selected metal ions as well as for no metal ion in the center	52
Table S 1. List of oligonucleotides	105
Table S 2. List of Plasmids.....	107

Part I.

**Structural and mechanistic investigation of the rare earth elements-
and calcium- dependent quinoproteins in *Pseudomonas putida*
KT2440**

1. Introduction

1.1. Rare earth elements (REEs) are misunderstood.

“...*We are made of stardust.* ...” Carl Sagan once famously stated. Indeed, nearly all elements found are derived from cosmic events creating elements in a process called nucleosynthesis [1]. Nevertheless, this process is only efficiently producing elements up to iron in an exothermic fusion reaction and all heavier elements are created in endothermic fusions during supernovae or neutron star collisions which occur more rarely [1], [2]. It is therefore that heavy elements are much more uncommon.

Metal elements are main key players in biology as they represent vital structural and/or catalytic cofactors for up to one-third of all known enzymes to perform their activity [3], [4]. It is noticeable that only lighter elements are involved in biological processes, while heavy elements were always believed to play no vital biological role as dependence on them would restrict organisms to more rare conditions where they could rely on the availability of these elements.

1.1.1. Rare earth elements are not rare.

In the center of Mendeleev's Periodic table or as an additional row below its main body located a series of 17 elements, including the lanthanides from lanthanum (La₅₇) through lutetium (Lu₇₁) together with scandium (Sc₂₁) and yttrium (Y₃₉), are called rare earth elements (REEs) (**Figure 1**) [5]. Lanthanoids or lanthanides (Ln) have been called by International Union of Pure and Applied Chemistry (IUPAC) as a result of sharing similar properties to Lanthanum. They are further divided into the "light" for early lanthanides (lanthanum to samarium) and the "heavy" for the

Introduction

later lanthanides (europium to lutetium) [6]. Scandium and yttrium usually found on the same ore deposits where Ln occur and have similar chemical characteristics to them. Therefore, they have been grouped as rare earth elements [5], [6].

Sc ₂₁														
Y ₃₉														
La ₅₇	Ce ₅₈	Pr ₅₉	Nd ₆₀	Pm ₆₁	Sm ₆₂	Eu ₆₃	Gd ₆₄	Tb ₆₅	Dy ₆₆	Ho ₆₇	Er ₆₈	Tm ₆₉	Yb ₇₀	Lu ₇₁

Figure 1. Rare earth elements and their atomic numbers as shown in Mendeleev's Periodic table. REEs consist of scandium, yttrium and the 15 lanthanide elements (lanthanum, cerium, praseodymium, neodymium, promethium, samarium, europium, gadolinium, terbium, dysprosium, holmium, erbium, thulium, ytterbium, and lutetium).

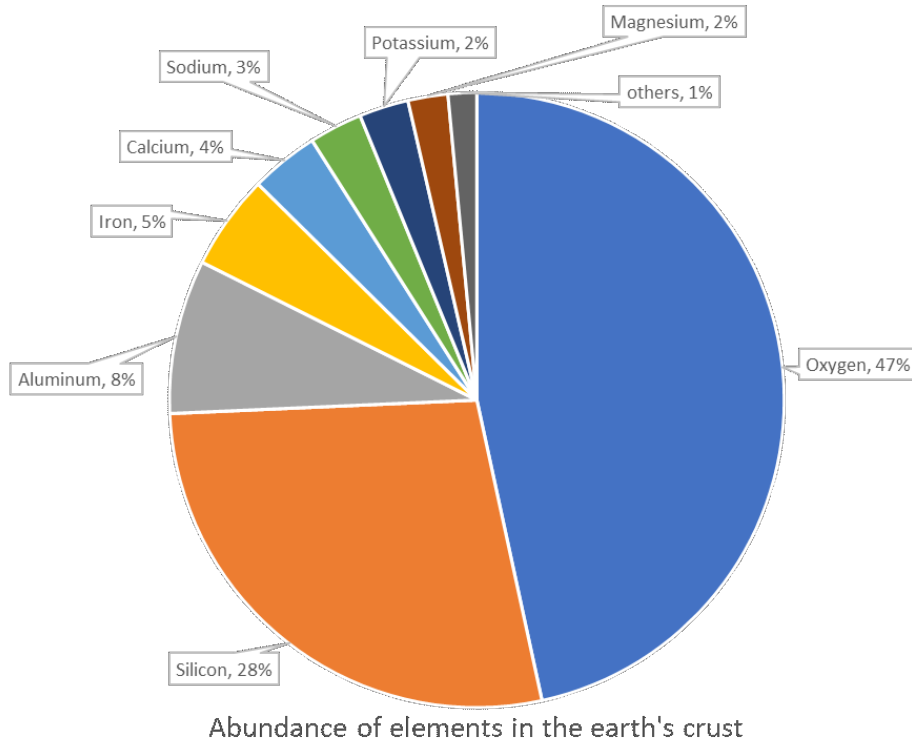
REEs inaccurately thought to be rare, although they occur abundantly than well-known distributed elements in the earth's crust. Their mostly widely distributed element, cerium (Ce), being the 26th most abundant among all known elements is almost equivalent to the abundance of the well-known distributed elements such as copper or zinc and even the least distributed one, terbium (Tm), is more abundant than iodide or silver.

As only eight elements represent approximately 99% of the earth's crust (**Figure 2A**) [7]. It is therefore that all other known elements could be considered as rare elements compared to these abundant elements. Correctly, the "rare" in the term "Rare earth elements" indicates that these elements rarely exist in pure form where many of them often co-exist together originating within other minerals. They are naturally found as a mixture of oxides extracted from ores as phosphate or carbonate minerals, for example monazite, bastnaesite, and xenotime. These minerals were considered as uncommon oxide-type "earth" minerals which was the reason to call it earth elements [5], [8].

Introduction

These earth elements are characterized by their very similar physical properties in addition to the very low solubility at common soil pH. This package of challenges results in a hard and expensive mining process for their extraction and separation [9], [10]. Therefore, they have been called “the rare earth elements”, however they are not rare in their abundance in the earth’s crust compared to other known elements. As a general fact, early REEs are more abundant than later ones with Oddo-Harkins rule apply where these with odd atomic numbers are less abundant than those of even atomic numbers (**Figure 2B**) [5], [6].

A



B

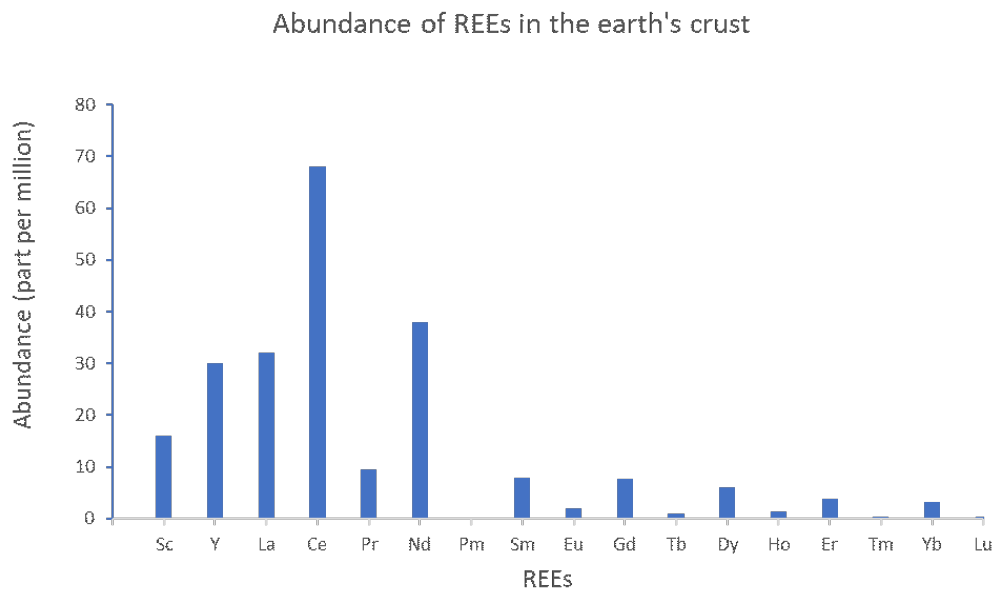


Figure 2. Abundance of elements in the earth's crust. A. Percentage of elements involved in the earth's crust. **B.** Abundance of REEs shown in part per million [5], [7].

1.1.2. Rare earth elements are not biologically inert.

During the last three decades, there has been a revolution in the applications of REEs. REEs are famous for their crucial role in a wide variety of several modern technologies, such as permanent magnets in wind energy converters, electric car batteries, lasers phosphors, smartphones, computers, and medical imaging agents due to their unique physical and chemical characteristics [11], [12]. However, it has been assumed that they are biologically inert for a long time as no evidence has been reported that any known organism could utilize these elements. Only a few biological studies that have used REEs due to their attractive chemical and physical properties have been reported. For example, Harry *et al.* have used terbium (Tb) as a luminescent probe for their unique photophysical properties to investigate a group of calcium-binding proteins [13].

1.1.2.1. Ionic radii of early rare earth elements mimic the ionic radius of calcium, the common biological cofactor.

Lanthanides provide interesting chemical properties due to their 4f-orbitals. Theoretically, the atomic electron configuration of the Ln is $[\text{Xe}]6s^24f^n$ except for La, Ce, Gd and Lu where 5d orbital is occupied with one electron. The main oxidation state of Ln in aqueous solutions is +3 where the 6s electrons and usually one 4f electron are lost (one 5d electron in case of La, Ce). However, +2 oxidation state has also been reported to be accessible to all Ln in soluble crystalline molecular species, but Eu^{+2} is the only member that has been reported to be stable in this oxidation state. In addition, Ce^{+3} can lose its single f electron to form Ce^{+4} with the stable electronic configuration of xenon. The high charge of Ln^{+3} , together with the high potential of 4f-orbitals to accept electrons, make them exhibiting good Lewis acidity properties [11], [12].

Introduction

Across the Lanthanides' series, each following element has one more positive nuclear charge accompanied by one consequent rise in the electrons occupying the 4f orbitals surrounding the nucleus. According to "Aufbau rule" or the atomic build-up principle of an atom in the ground state, electrons fill the orbital of lowest energy first and subsequent electrons are fed in the order of increasing energies [13]. Therefore, the lower energy 6s orbitals are filled before the higher energy 4f orbitals in accordance with the diagonal Madelung's rule [14]. Due to the fact that the radial density of 4f orbitals is closer to the nucleus than for that of 6s, 4f electrons poorly shield outer shells from the increased positive nuclear charge so that the nucleus could steadily attract the outer electrons through the lanthanide elements. As a result, Lanthanides' series exhibits greater ionic radius reduction across its elements than expected, ranging from 1.16 Å (La^{+3}) to 0.98 Å (Lu^{+3}) in a phenomena known as "lanthanide contraction" (**Figure 3**) [15], [16].

Interestingly, the ionic radius of early Ln^{+3} (1.16 Å- 1.12 Å) mimic that of calcium (Ca^{+2}) (1.14 Å), the commonly biological metal ion [15], [16]. The higher charge to ionic radius ratio of early light Ln compared to the commonly biological metal ions such as Ca^{+2} , Mg^{+2} , and Zn^{+2} giving them more advantages as stronger Lewis acids preferring different ligands with flexible geometries to acclimate high coordination numbers (CNs) from 8-12 that are seldom occurred with other common metal ions [11], [17].

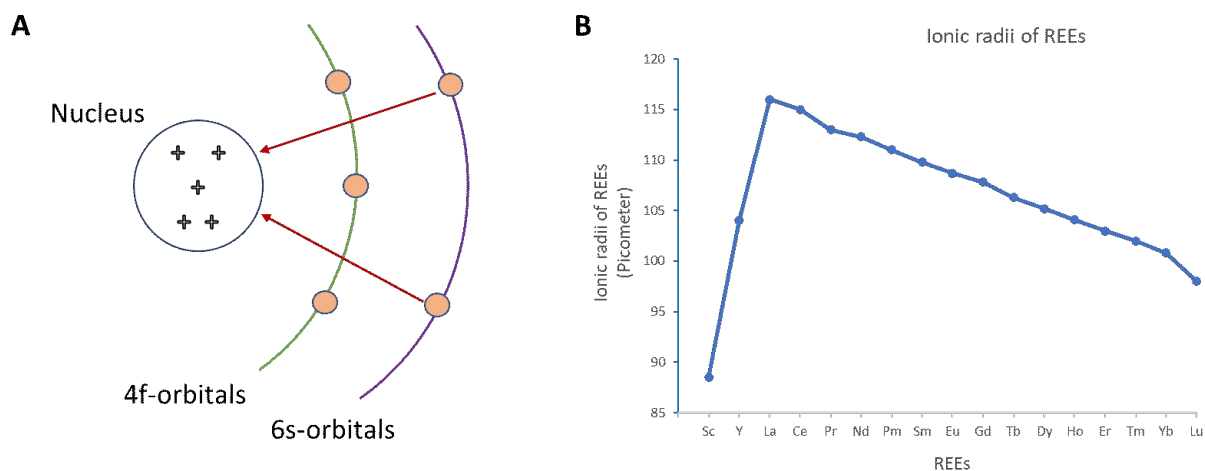


Figure 3. Lanthanide contraction and ionic radii of REEs. A. Description the reasons beyond lanthanide contraction behavior. The effective nuclear charge of the nucleus is increasing across the lanthanides' series with the increase of 4f-electrons. Due to the less shielding effect of 4f-orbitals as it is closer to the nucleus than 6s-orbitals, the nucleus efficiently attracts the 6s-electrons resulting in contraction of the ionic radii greater than expected or what is known as lanthanide contraction across the series of lanthanides. **B.** Ionic radii of REEs in picometer [15].

1.1.2.2. Biological role of rare earth elements has been established over the last decade.

The discovery of REEs role in biology has started when China used a mixture of these elements as trace supplements increasing the crop production [18] and animal growth promoters [19]. As a result, they have been transferred to the food chain. Together with the wide distribution of REEs use in technological product [20], this increases the attention to study the effect of REEs on the environment and human health.

Methylotrophs and methanotrophs represented the kick-off organisms where the biological role of REEs has been firstly discovered ten years ago. They are a group of bacteria utilize single carbon compounds, for example methanol and methane, as their sole carbon source. They, as environmental organisms in direct contact

Introduction

with soil, water, and plants, were of great interest to study the effect of REEs on the environment. In a cycle of studies performed by Japanese groups, have been published in 2011, to investigate the effect of REEs on methanol dehydrogenase (MDH) activity of *Methylobacterium radiotolerans*, *Bradyrhizobium* sp. MAFF211645, and the model plant phyllosphere colonizer *Methylobacterium extorquens* strain AM1, they elucidated that La^{+3} and Ce^{+3} increased the MDH activity through induction and regulation of a “latent” gene. Genetic and biochemical analysis suggested afterwards that it was *xoxF* and belongs to the quinoprotein alcohol dehydrogenases, a group of enzymes that depends on the redox cofactor pyrroloquinoline quinone (PQQ) and previously believed to be only calcium-dependent family [21]–[23].

These studies represented the first line that changed the belief that REEs are biologically inert. However, they showed that REEs promote the growth of bacterial cells, and they are not essential for them to grow as they encodes both calcium- and REEs- dependent homologs. The essence of REEs for life has been discovered through the volcanic mudpot water rich in REEs content when the growth of the *Methylacidiphilum fumariolicum* strain SolV was strictly dependent on the amount of its original habitat water added to the growth culture. Genomic analysis of the strain SolV revealed that it has only a REEs-dependent *xoxF* gene and it does not encode the Ca-dependent homolog. In turn, bacterial cells showed direct proportional growth with the amount of cerium added to the culture in case that its original habitat water was not added [24].

Besides the accumulation of different REEs elements by different types of bacteria, they have been determined in human body within different organs. They have also been detected in different kinds of aqueous environments such as ground, river and sea water with significantly higher concentrations in volcanic mudpots [25], [26]. An interesting observation highlights the ecological and biological role of

REEs was the depletion of the light REEs together with methanotrophic bacteria flourish in a submerged plume of water with high methane content during the Deepwater Horizon oil spill in 2010 [27].

Bioinformatic studies provide evidence that REEs-dependent enzymes are broadly dispersed among Eukaryotes as well as in Prokaryotes [28]. In ten years since REEs were unexpectedly found to play a role in methylotrophs, and they appear to be more widely spread throughout biological functions. *Pseudomonas putida* widens the REEs-utilizing bacteria beyond methanotrophic bacteria by the recent discovery that it expresses a REEs-dependent alcohol dehydrogenase (PedH) [29].

1.2. *Pseudomonas putida* is a REEs-utilizing bacterium.

1.2.1. *Pseudomonas putida* is a ubiquitous rhizosphere soil colonizer.

Pseudomonas putida, as a ubiquitous rhizosphere soil colonizer [30], is exposed to a wide variety of plant growth promoters, pesticides, and pollutants with antiherbivore, antibacterial, and antifungal characteristics. In addition, it encounters variable chemicals originated from different sources such as metabolic products of various bacterial, yeast, fungal, and plant species [31]. Of these chemicals, volatile alcohols represent a major category to which these root colonizers are regularly exposed [32]. Therefore, the inhabitant environment of *P. putida* represents a very challenging niche for survival and growth [33]–[36].

In order to establish in such a niche, *P. putida* exhibits a versatile intrinsic metabolism with diverse enzymatic capacities for efficient utilization of these chemicals [35], [37], [38]. To use volatile alcohols efficiently, it expresses 2 different types of alcohol dehydrogenases (ADHs), the cytoplasmic NAD(P)-

dependent ADHs [39] and the periplasmic quinoproteins, are also known as pyrroloquinoline quinone (PQQ)-dependent ADHs [29]. These dehydrogenases usually play a key role in energy production, catalyzing the oxidation of alcohols as a source of carbon to the corresponding aldehyde, which is then either further oxidized to carbon dioxide or incorporated into cell material.

1.2.2. Pyrroloquinoline quinone (PQQ)-dependent alcohol dehydrogenases (ADHs) in *P. putida*.

1.2.2.1. PQQ is a redox cofactor.

PQQ, also called methoxatin, is a tricyclic o-quinone (4,5-Dioxo-4,5-dihydro-1H-pyrrolo[2,3-f]quinoline-2,7,9-tricarboxylate (**Figure 4**). It serves as a cofactor in several enzyme-catalyzed redox reactions in different bacteria. It is synthesized separately in the cytosol from glutamate and tyrosine amino acids through a group of proteins encoded by *PqqABCDEFGHIG* gene cluster and then transferred to the periplasm with unknown mechanism where it binds non-covalently into the active site of the PQQ-containing enzymes, frequently called quinoproteins [40]–[42]. It was firstly introduced as a redox cofactor with glucose dehydrogenases [43] before it was discovered with methanol dehydrogenases where it was firstly structurally determined [44].

Different subclasses of PQQ-ADHs have been characterized. Type I are soluble, periplasmic enzymes containing a single PQQ prosthetic group but no other redox cofactors. Type II dehydrogenases are soluble, periplasmic, quinohemoproteins, having a C-terminal cytochrome domain containing covalently bound heme [45]–[47]. The periplasmic location of PQQ-ADHs is advantageous as it represents the first defense line against toxic volatile alcohols. This secures fast oxidation of these volatiles avoiding the problem of energy consuming due to volatiles transporting

into cells or of having high concentrations of them within the cells that could be lethal [46], [48].

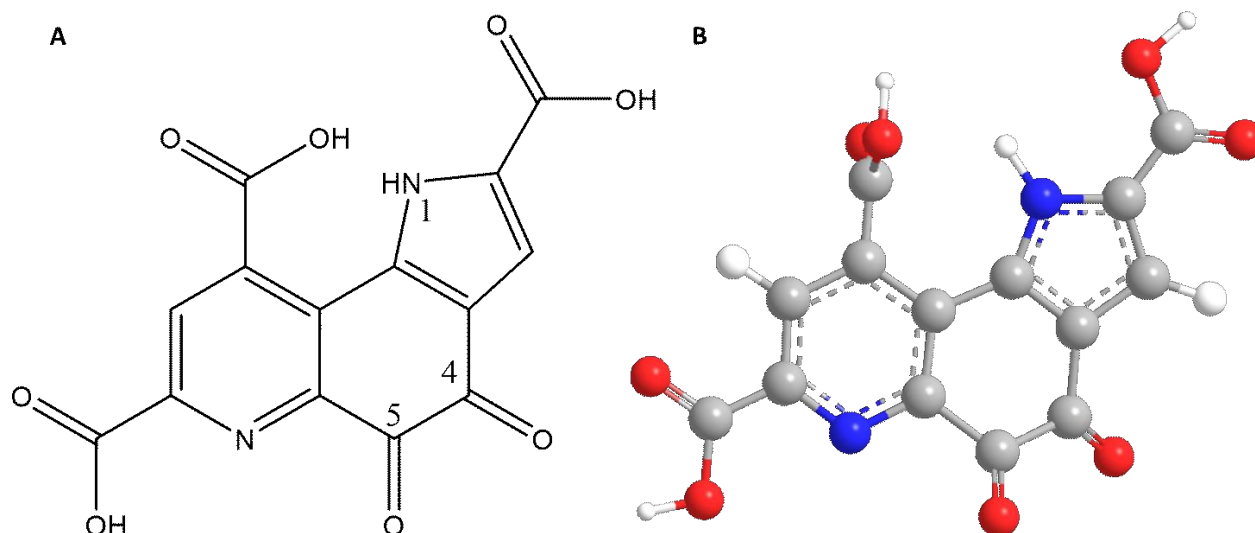


Figure 4. Structure of pyrroloquinoline quinone (PQQ). **A.** 2D structure of PQQ. It is a tricyclic o-quinone (4,5-Dioxo-4,5-dihydro-1H-pyrrolo[2,3-f]quinoline-2,7,9-tricarboxylate). **B.** 3D structure of PQQ in the same ring orientation as shown in **A**.

1.2.2.2. Proposed mechanisms of PQQ-ADHs

PQQ-ADHs catalyzes a redox reaction involved in energy production process, where oxidation of the alcohol to the corresponding aldehyde and reduction of the PQQ cofactor take place simultaneously (**Figure 5**). This is accompanied with two successive single-electron transfers to a heme group of c-type cytochrome, during which an oxidation of the reduced PQQ (PQQH₂) to the quinone through the free radical semiquinone occurs (**Figure 6A**) [42], [49]. It is, therefore, that the periplasmic PQQ-ADHs have to be coupled to an electron transport system where the released electrons from the PQQH₂ are transported stepwise through this system towards a molecular oxygen (O₂) that represents the terminal electron acceptor. On the meantime, this is coupled with liberation of 2 protons into the periplasm contributing to the protonmotive force across the inner cytoplasmic membrane. The movement of these protons, driven by this force, is coupled to the

synthesis of ATP from ADP and inorganic phosphate moiety P_i by the membrane ATP synthase. In total, the periplasmic oxidation of one alcohol molecule by PQQ-ADHs results in generating one ATP molecule by ATP synthase and a molecule of water through reduction of a molecular oxygen ($2H^+ + 2e^- + \frac{1}{2}O_2 \rightarrow H_2O$) by a terminal oxidase [49]–[51].

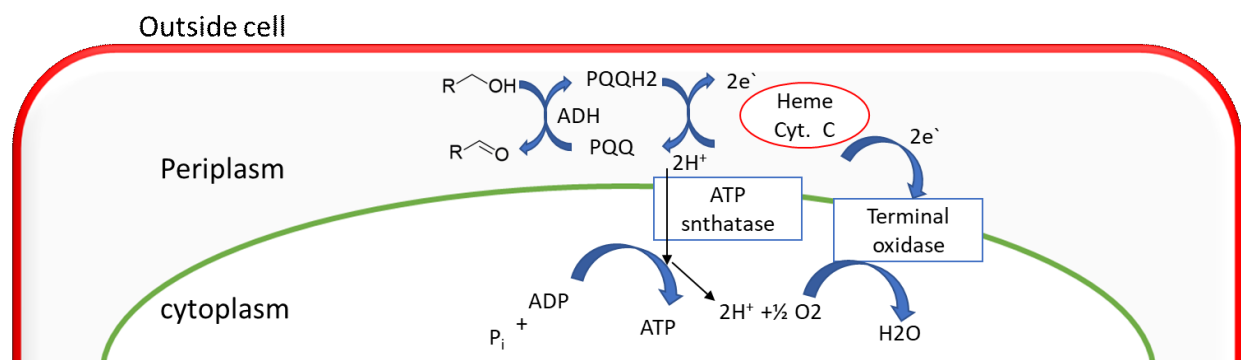


Figure 5. Periplasmic oxidation of alcohols by PQQ-ADHs for energy production process. Alcohol is oxidized to the corresponding aldehyde by the PQQ-ADHs leading to the reduction of PQQ into its reduced form (PQQH₂). The oxidation of PQQH₂ is associated with transfer of 2 successive electrons through an electron transfer chain and liberation of 2 protons contributing to the protonmotive force resulting in synthesis of ATP and H₂O by ATP synthase and terminal oxidase, respectively.

There are 2 hypotheses explaining the periplasmic oxidation by PQQ-ADHs, the direct hydride transfer mechanism or addition-elimination mechanism (**Figure 6**) [49], [52]. Both scenarios involve proton abstraction from the alcohol group by an active site base as the first step. The addition/elimination mechanism favors the hemiketal complex intermediate formation where the C-5 carbonyl of PQQ is exposed to the nucleophilic attack by the oxygen atom of the alcohol group forming a covalent PQQ substrate complex. Subsequently, the pyrrole N-atom of PQQ facilitates the ionization of the hemiketal complex results in reduction of PQQ and aldehyde release (**Figure 6B**). On the other hand, the hydride transfer mechanism involves a direct hydride transfer from the alcohol alkyl group to the C-5 of PQQ after the proton abstraction (**Figure 6C**). The direct hydride transfer hypothesis is

predominated by structural and quantum mechanical studies to be the mechanism of the periplasmic PQQ-dependent oxidation [49], [53], [54].

Whatever the mechanism involved in the oxidation process; the metal ion has an essential role as a cofactor. On one side, It has a structural function to conserve the redox cofactor PQQ in an active conformation. On the other side, it facilitates the redox reaction through the direct hydride transfer or the addition/elimination mechanism as it acts as a Lewis acid coordinating the C-5 carbonyl oxygen of PQQ, thus stabilizing the electrophilic C-5 for the nucleophilic attack [49], [52], [53].

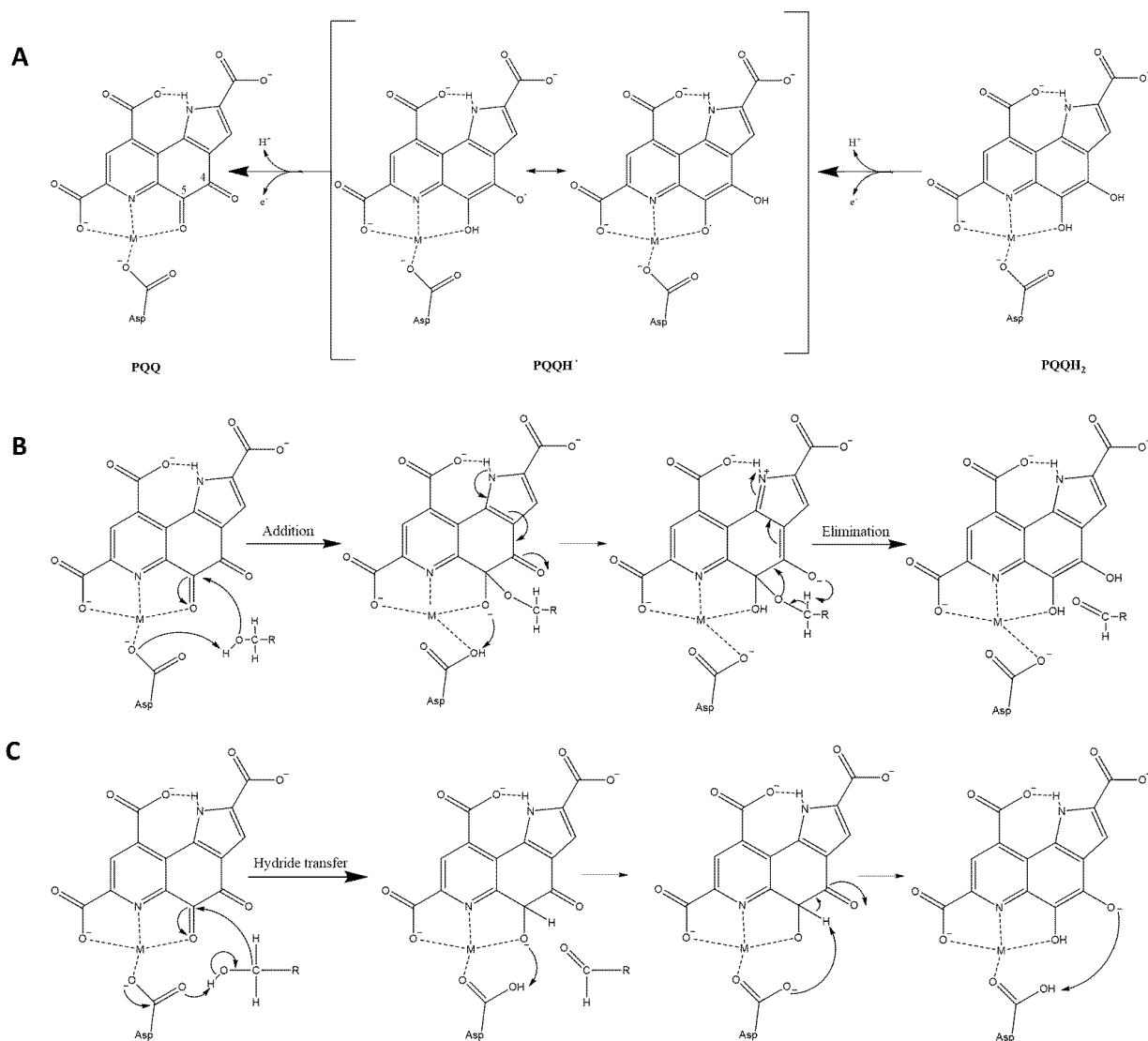


Figure 6. Proposed mechanisms of quinoproteins for alcohol oxidation. A. pyrroloquinoline quinone in oxidized (PQQ), semiquinone free radical (PQQH \cdot), and reduced (PQQH $_2$) forms in complex with metal (M) and the active site aspartate residue involved in the first proton abstraction from the alcoholic group. **B.** Addition/elimination mechanism hypothesis where a covalent alcohol PQQ complex formed. **C.** Hydride transfer mechanism hypothesis where a direct hydride transferred to electrophilic C5 of PQQ [49], [52].

1.2.2.3. *P. putida* expresses 2 different enzymes of the subclass Type I PQQ-ADHs on the same operon with a different metal cofactor.

Interestingly, *P. putida* expresses 2 different enzymes of the subclass Type I PQQ-ADHs, encoded by *PedE* (PP_2674) and *PedH* (PP_2679) on the same operon, with the same scope of substrate [29]. They are a part of the catabolic pathway *ped* gene cluster that involves besides these 2 dehydrogenases the participation of two different two-component signal-transducing systems (*PedS1R1* and *PedS2R2*), a periplasmic binding protein (*PedG*), a putative cytochrome *c* (*PedF*), an aldehyde dehydrogenase (*PedI*), a pentapeptide repeat protein (*PedD*) and a membrane-bound ATP-binding cassette transporter system (*PedABC*) (**Figure 7**). Additionally, two accessory sets of elements (encoded by *PqqABCDEF* and *CcmABCDEFGHI*) are necessary for the operation of the main pathways (*Ped*). *PqqABCDEF* is required for the biosynthesis of PQQ, that transfers electrons to an independent cytochrome *c*; whereas *CcmABCDEFGHI* is required for cytochrome *c* maturation [55].

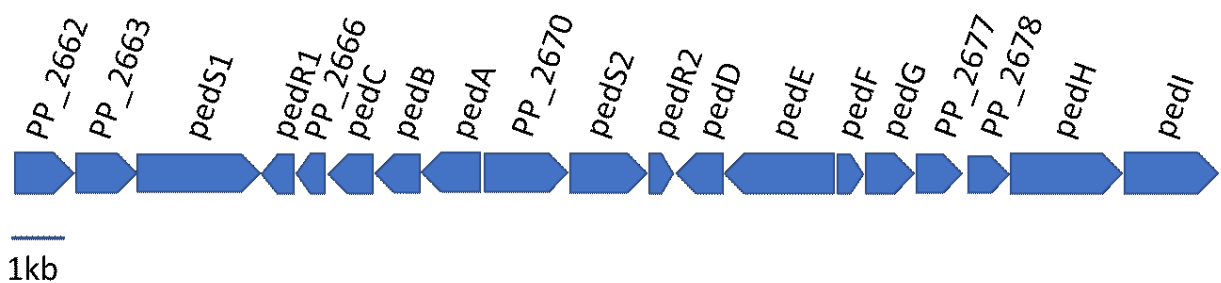


Figure 7. *Ped* gene cluster involved in volatiles oxidation of *P. putida* [55].

It was not clear why *P. putida* could express 2 members of the same type, *PedE* and *PedH*, encoded on the same operon and perform the same function on the same scope of substrates. This was attributed to the vital need to ensure the fast elimination of these alcohols, thereby preventing their toxicity to various metabolic

Introduction

processes [55]. A new piece of knowledge has been discovered over the last decade. It was believed that calcium represents the metal cofactor for PedE and PedH as well as other PQQ-ADHs [49], [52]. However, this has been dramatically changed over the last decade with the surprising role of REEs with PQQ-MDH in methanotrophic bacteria [24], [56]. In a recent study, it is reported that PedH could utilize REEs as a metal cofactor widening the REEs-utilizing bacteria beyond the methanotrophic and methylotrophic bacteria [29].

2. Aim of the work.

Pseudomonas putida KT2440 is the best-characterized saprophytic member of *P. putida* species that natively live and thrive in soil environments [33], [38]. This soil-dwelling bacterium employs the REEs-dependent alcohol dehydrogenase (ADH), PedH (PP_2679), in order to degrade plant-, fungal-, and bacteria-derived volatiles. Mechanistically, PedH resides in the periplasm of *P. putida* KT2440 and exhibits activity on a similar set of substrates as its strictly calcium-dependent counterpart PedE (PP_2674) [29]. Nonetheless, it is not defined till now why PedH could be able to utilize REEs in its alcohol dehydrogenase activity while PedE utilizes calcium to perform the same function. In particular, Ca^{+2} or the early Ln^{+3} share almost the same ionic radius and play the same role in the periplasmic PQQ-dependent oxidation process.

It is therefore that this work aims at the structural, biochemical, and functional understanding of enzymes involved in the periplasmic oxidation process of volatiles in *P. putida* KT2440. A particular focus should be on the recently discovered REEs- and calcium- dependent PQQ-ADHs, PedH and PedE, respectively. A combined approach of X-ray crystallography and biochemistry should uncover differences and similarities between both subclasses of the PQQ-dependent ADHs family. These results shall facilitate a thorough explanation of REEs- and calcium- mediated biochemistry of quinoproteins in *P. putida* KT2440. In addition, this understanding would help in establishing these enzymes as novel tools for biosynthetic routes to medically and/or industrially relevant products using readily available bulk chemicals or renewable resources.

3. Results.

3.1. Structural analysis of PedE and PedH.

3.1.1. Purification of PedE and PedH.

To investigate the reasons beyond the metal cofactor dependency of PedE and PedH [29], it was aimed to analyze their structure defining their differences and similarities. To do so, the genes encoding the PQQ-ADHs without the nucleotides corresponding for the signal peptide PedE34-634 (PP_2674) carrying a N-terminal hexa-histidine tag and PedH28-595 (PP_2679) carrying a C-terminal hexa-histidine tag were cloned to pET24d producing pET24d-PedE and pET24d-PedH, respectively as detailed in chapter **5.2.2**.

The plasmid of interest was then transformed in *E. coli* BL21 (DE3) in order to heterologously produce the protein using auto-induction medium. Subsequently, the protein was purified by employing immobilized metal affinity chromatography (IMAC) on a nickel-nitrilotriacetic acid (Ni-NTA) column (**Figures 8A, 8E**) then the elution has treated with ethylenediaminetetraacetic acid (EDTA, 100mM) to completely remove any binding metal from the polypeptide and finally size-exclusion chromatography (SEC) was applied as detailed in chapter **5.2.2**. using a HiLoad 26/600 Superdex 200 column (**Figures 8B, 8F**). The collected fractions were pooled, and the protein was concentrated to a final concentration of 50 mg/ml to further use it to set up future experiments.

To investigate the oligomerization state of the purified proteins, aliquots of purified proteins were used for analytical SEC. Samples of 100-200 μ M of each fraction peak were loaded onto a Superdex 200 10/300 column. The different peaks of

Results

PedE had eluted at approximately 66 and 135 kDa (**Figure 8D**). Given the molecular mass of ~ 66 kDa of a PedE monomer, this suggests a monomeric and homodimeric assembly of PedE on SEC. On the other hand, PedH had eluted in an apparent molecular mass of approximately 125 Kda (**Figure 8H**). Given the molecular mass of ~ 62.5 Kda of a PedH monomer, this suggests a homodimeric assembly of PedH.

Results

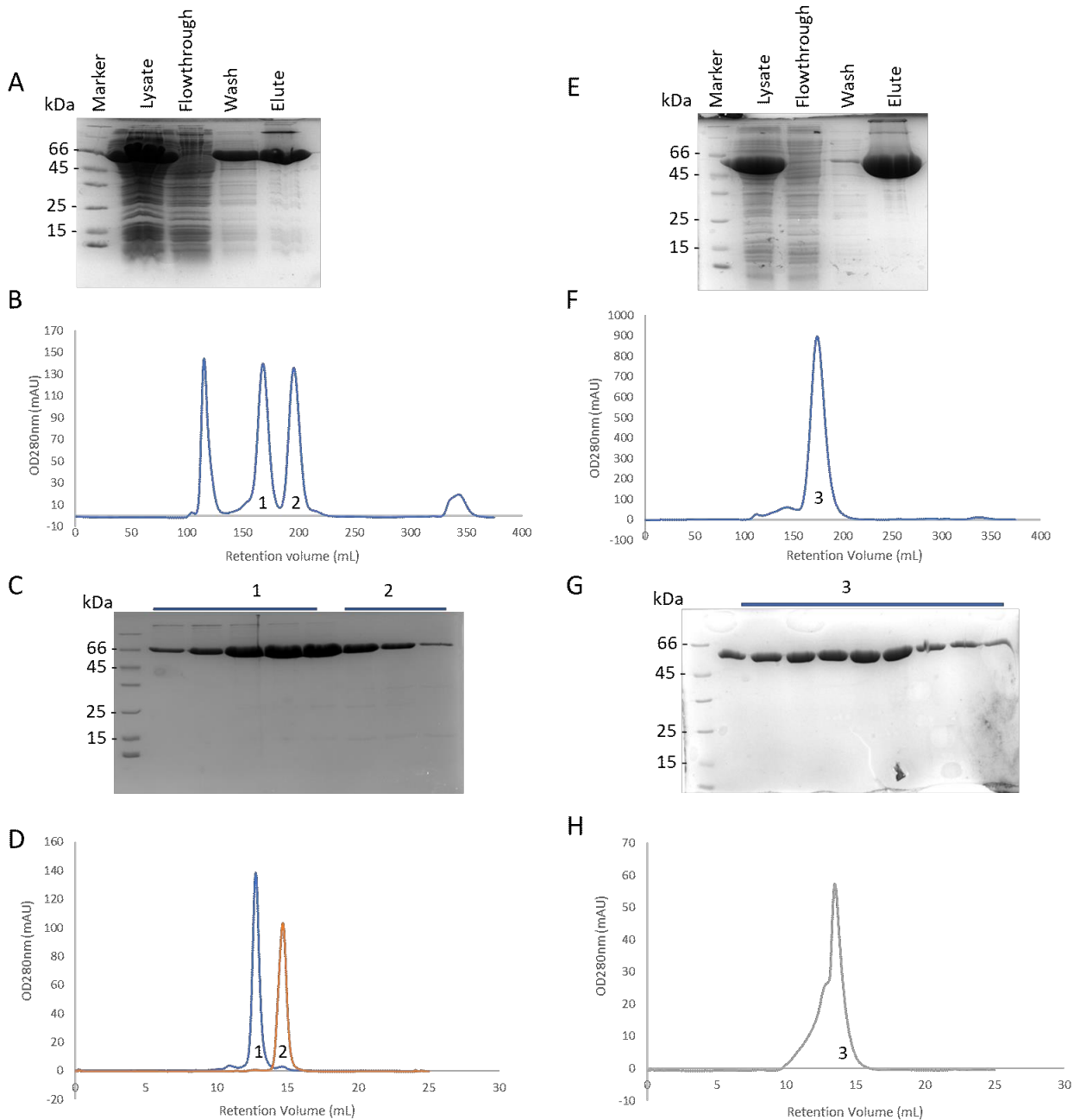


Figure 8. Immobilized metal affinity chromatography (IMAC) and size-exclusion chromatography (SEC) of PedE (A-D) and PedH (E-H). A and E represent the Coomassie-stained SDS-PAGE of IMAC on a nickel-nitrilotriacetic acid (Ni-NTA) column. B and F represent chromatograms from SEC. C and G are the respective SEC Coomassie-stained SDS-PAGE. D and H are the chromatograms from analytical SEC.

3.1.2. Microscale thermophoresis (MST) of PedE and PedH to different metals.

In close collaboration with Dr. Sven Freibert at the Philipps-University Marburg, microscale thermophoresis (MST) was employed as detailed in chapter 5.2.9. to detect the affinity of PedE and PedH towards Ca^{+2} and different Ln^{+3} , respectively. The purified protein in a concentration of 200 nM with equimolar concentration of PQQ had been titrated with different concentrations of the metal ion of interest ranging from (0-5 mM in case of CaCl_2 and 0-50 μM in case of LnCl_3). PedE showed a dissociation constant (K_d) value of $24 \pm 6.8 \mu\text{M}$ towards Ca^{+2} (**Figure 9**). On the other hand, PedH showed a nanomolar K_d values towards the early Ln^{+3} that have an ionic radius of (112-115 pm) which is close to that of Ca^{+2} (114 pm) [15]. The calculated K_d values were $35 \pm 2.6 \text{ nM}$, $178 \pm 19 \text{ nM}$, $706 \pm 68 \text{ nM}$ and $866 \pm 156 \text{ nM}$ in case of Nd^{+3} , Pr^{+3} , Ce^{+3} and La^{+3} , respectively. However, it showed higher K_d values with the heavier lanthanides ranging from 2 μM to 11.6 μM (**Figure 10**).

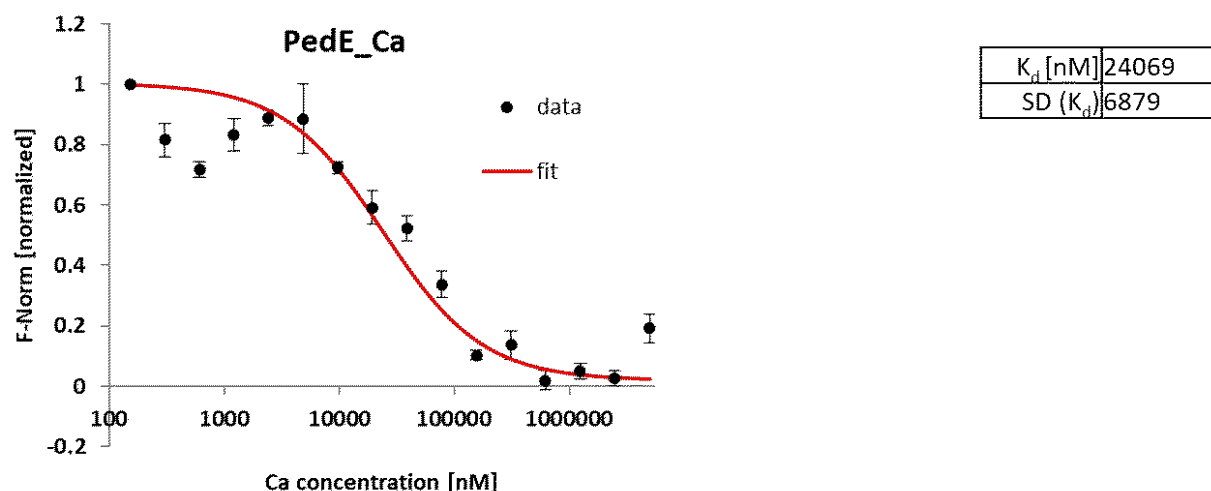


Figure 9. Binding affinity of PedE towards calcium using microscale thermophoresis (MST). The affinity in terms of dissociation constant (K_d) is calculated from the MST fitted curve that plots normalized fluorescence against concentration of calcium.

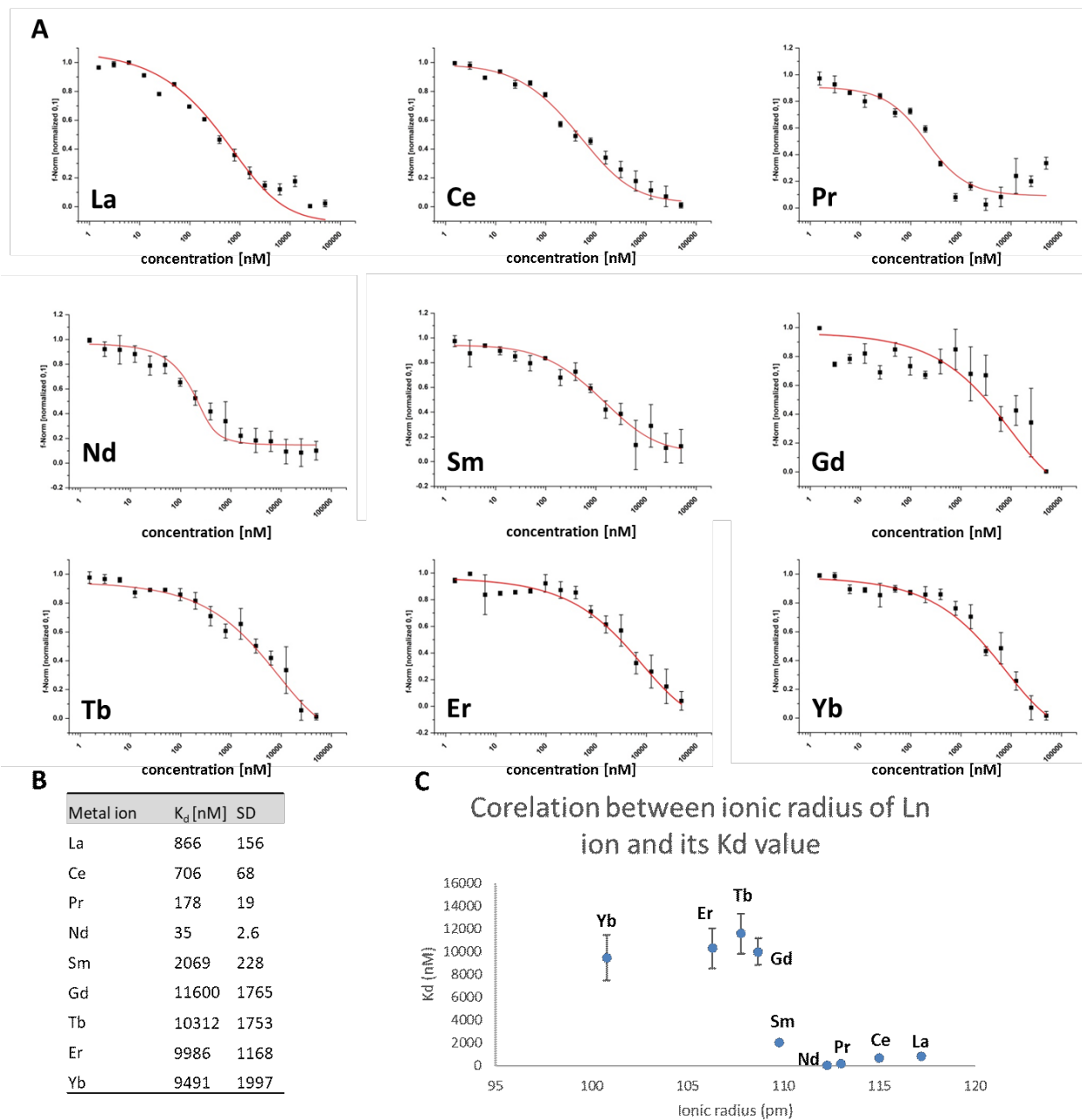


Figure 10. Binding affinity of PedH towards different lanthanides. A. MST binding curves of PedH towards different Ln. **B.** Table of the affinity in terms of dissociation constant (K_d) values of different lanthanides towards PedH. **C.** correlation between the ionic radius of Ln^{+3} and its K_d value towards PedH.

3.1.3. Crystallization of PedH and PedE.

For the crystallization of PedE and PedH, 20 mg/ml of protein was mixed with ten times molar concentrations of the PQQ cofactor and the metal of interest (CaCl₂ in case of PedE and LaCl₃, CeCl₃, PrCl₃, and NdCl₃ in case of PedH) used in a sitting drop experiment. 500 nl of protein was mixed with the same amount of precipitant solution. Crystals suitable for X-ray diffraction experiments were observed within 2-3 days of incubation at room temperature in several crystallization conditions as mentioned in (**Table 1, Figure 11**). Several crystals were picked with nylon loops and shortly incubated in precipitant buffer with 30 % glycerol prior to flash freezing in liquid nitrogen.

Table 1. Different crystallization conditions of PedE and PedH

Protein	Crystallization Condition
PedH	0.2 M ammonium sulfate, 20 % (w/v) PEG 3350.
	0.1 M sodium acetate pH 4.6, 20 % (w/v) PEG 3000.
	0.2 M ammonium sulfate, 0.1 M sodium acetate pH 4.6, 30 % (w/v) PEG 2000 MME.
	0.2 M ammonium sulfate, 0.1 M sodium acetate pH 4.6, 25 % (w/v) PEG 4000.
	0.2 M ammonium dihydrogen phosphate, 25 % (w/v) PEG 3350.
PedE	0.2 M sodium acetate, 0.1 M sodium cacodylate pH 6.5, 30 % (w/v) PEG 8000.
	0.04 M potassium dihydrogen phosphate, 16 % (w/v) PEG 8000, 20 (v/v) glycerol.
	0.16 M ammonium sulfate, 0.08 M sodium acetate pH 4.6, 20 % (w/v) PEG 4000, 20 (v/v) glycerol.

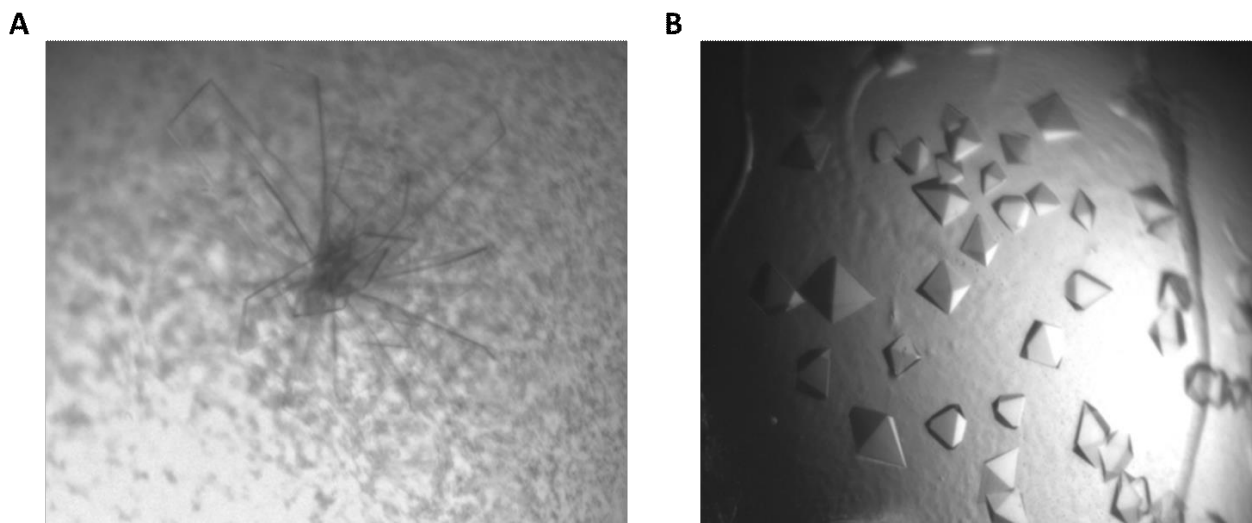


Figure 11. Crystals of PedE and PedH. **A.** Crystals of PedE observed within a condition of 0.16 M ammonium sulfate, 0.08 M sodium acetate pH 4.6, 20 % (w/v) PEG 4000, 20 (v/v) glycerol. **B.** Crystals of PedH observed within a condition of 0.2 M ammonium sulfate, 0.1 M sodium acetate pH 4.6, 30 % (w/v) PEG 2000 MME.

3.1.4. Crystal structures of PedE and PedH.

The X-ray diffraction data were collected, integrated, and processed as detailed in chapter 5.2.6. The structure of the ADH-PQQ-Metal ion complex was determined by molecular replacement using the crystal structures of ExaA of *Pseudomonas aeruginosa* (PDB-ID: 1FLG) as search models [57]. The crystal structure of PedE was determined at resolution of 2.4 Å, determined as space group $P2_12_12_1$ and was refined to $R_{\text{work}}/R_{\text{free}}$ of 15.1/19.5. On the other hand, PedH resulted in different crystal lattice, namely spacegroup $P4_32_12$, and PedH structures were determined at resolutions ranging from 1.5 – 2 Å. The same space group was detected in all different co-crystallized metals. The structures were refined to an $R_{\text{work}}/R_{\text{free}}$ of 15.1/16.1, 14.5/16.6, 16.7/18.4 and 15.6/17.8 in case of La^{+3} , Ce^{+3} , Pr^{+3} , and Nd^{+3} , respectively (Tables 2 & 3).

Table 2. Data collection and refinement statistics of PedH in presence of La, Ce, and Pr.

	PedH, La	PedH, Ce	PedH, Pr
Data collection			
Space group	P4 ₃ 2 ₁ 2	P4 ₃ 2 ₁ 2	P4 ₃ 2 ₁ 2
Cell dimensions			
a, b, c (Å)	105.04 105.04 186.59	105.18 105.18 186.55	105.716 105.716 186.942
α, β, γ (°)	90 90 90	90 90 90	90 90 90
Wavelength (Å)	0.976253	0.976253	0.976253
Resolution (Å)	46.65 - 1.51 (1.57 - 1.52)	47.71 - 2.0 (2.071 - 2.0)	47.28 - 2.0 (2.071 - 2.0)
R_{merge}	0.0931 (1.039)	0.01208 (0.03253)	0.0599 (2.424)
I / σI	23.22 (2.72)	16.40 (6.56)	8.27 (1.57)
Completeness (%)	99.78 (99.87)	99.93 (99.67)	99.86 (99.99)
Redundancy	26.5 (26.4)	13.2 (13.3)	26.5 (27.2)
CC1/2	0.999 (0.884)	0.997 (0.978)	0.989 (0.615)
Refinement			
Resolution (Å)	46.65 - 1.51	47.71 - 2.0	47.28 - 2.0
No. reflections	159961 (15756)	71282 (6997)	72098 (7107)
R_{work} / R_{free}	0.15/0.16	0.14/0.16	0.16/0.18
No. atoms	5054	5056	5089
Protein	4385	4385	4371
Ligand/ion	25	29	29
Water	644	642	689
B-factors	23.43	20.00	22.25
Protein	21.71	18.30	20.52
Ligand/ion	15.61	14.07	16.97
Water	35.40	31.85	33.46
R.m.s. deviations			
Bond lengths (Å)	0.012	0.017	0.012
Bond angles (°)	1.48	1.99	1.46
Ramachandran			
Favored (%)	96.09	95.91	96.27
Allowed (%)	3.37	3.91	3.55
Outliers (%)	0.53	0.18	0.18

*Values in parentheses are for highest-resolution shell.

*Data were collected on ID30A-1 (MASSIF-1, ESRF), ID23-2 (ESRF) and MX14.2 (BESSY).

Table 3. Data collection and refinement statistics of PedH in presence of Nd and PedE in presence of Ca.

	PedH, Nd	PedE, Ca
Data collection		
Space group	P4 ₃ 2 ₁ 2	P2 ₁ 2 ₁ 2 ₁
Cell dimensions		
a, b, c (Å)	105.125 105.125 186.743	72.37 128.61 331.81
α, β, γ (°)	90 90 90	90 90 90
Wavelength (Å)	0.976253	0.976253
Resolution (Å)	47.01 - 1.9 (1.968 - 1.9)	48.92 - 2.472 (2.561 - 2.472)
R _{merge}	0.1642 (1.497)	0.2465 (1.014)
I / σI	14.50 (1.66)	16.33 (4.03)
Completeness (%)	99.97 (99.99)	98.55 (87.42)
Redundancy	14.7 (14.7)	12.9 (12.1)
CC1/2	0.999 (0.697)	0.997 (0.892)
Refinement		
Resolution (Å)	47.01 - 1.9	48.92 - 2.472
No. reflections	82951 (8158)	110266 (9643)
R _{work} / R _{free}	0.15/0.17	0.15/0.19
No. atoms	5050	19131
Protein	4361	18152
Ligand/ion	30	104
Water	659	875
B-factors	28.74	29.99
Protein	27.29	29.84
Ligand/ion	23.98	26.60
Water	38.58	33.46
R.m.s. deviations		
Bond lengths (Å)	0.015	0.014
Bond angles (°)	2.05	1.57
Ramachandran		
Favored (%)	95.54	94.46
Allowed (%)	4.10	4.89
Outliers (%)	0.36	0.65

*Values in parentheses are for highest-resolution shell.

*Data were collected on ID30A-1 (MASSIF-1, ESRF), ID23-2 (ESRF) and MX14.2 (BESSY).

3.1.4.1. PedE and PedH arranged in a propeller-like style.

Sequence alignment of the Ca-dependent PedE and the Ln-dependent PedH shows ~ 79 % sequence similarity with up to 51% of sequence identity (**Figure 12A**). Structurally, they share the overall architecture showing eight W-shaped β -sheet motifs arranged circularly in a propeller-like style establishing a disk-shaped super barrel. This typical architecture is fully conserved in all known resolved quinoprotein alcohol dehydrogenases where each β -propeller blade W1 to W8 is formed by at least four antiparallel β -strands A, B, C and D. The innermost ones represent the A strands. Blade W3 and W5 is formed by six antiparallel β -strands. Blade W8 composed of β -strands A, B and C of the C terminus and strand D of the N terminus of the protein (**Figures 12B & 12C**).

Characteristically, a network of hydrophobic and hydrogen bond interactions leads to the close-fitting of the polypeptide backbone supporting the stability of the β -propeller fold pattern. Eight conserved regular repetitive tryptophan docking motifs (AWG) are formed by van der Waals contacts of alanine and tryptophan residues of β -strands C and D of one blade together with a glycine backbone located in strand D of the adjacent blade (**Figure 13**). Some variations from the regular AWG docking motif have observed. Phenyl alanine replaces tryptophan in position 378PedE/368PedH, and leucine replaces glycine in position 60PedE/70PedH. In addition, alanine is replaced by glycine in position 311PedE, valine in position 366PedE/356PedH, 591PedE and threonine in position 580PedH. However, this does not affect the interactions network among these motifs. The indole NH of the conserved tryptophan residues within these repetitive tryptophan docking motifs form hydrogen bonds with the backbone carbonyl group of residues 4 or 5 in the next amino acid docking sequence in the next blade, and a β -sheet hydrogen bond between its carbonyl oxygen atom and the main-chain amide nitrogen atom of residue 1 within the same amino acid docking sequence.

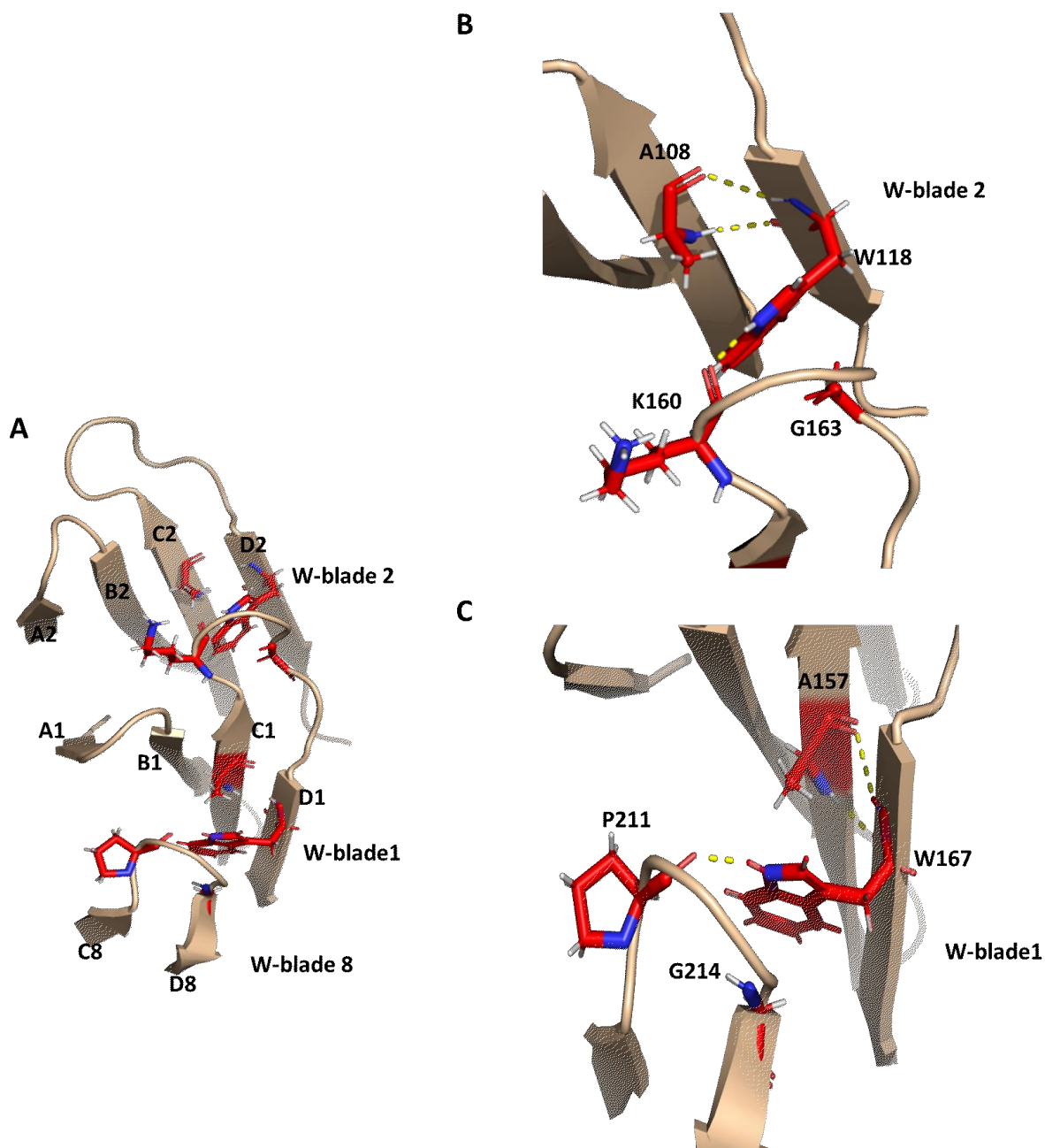


Figure 13. Interactions stabilizing the B-propeller structure of PedH. **A.** Arrangement of the β -sheets of W-blades 1 and 2 showing the four different antiparallel β -strands A, B, C and D in each W-blade. **B and C** represent 2 tryptophan docking motifs (AWG) out of 8 involved in the stabilization of the B-propeller structure showing residues involved in the hydrophobic and polar interactions (yellow dotted lines). The same pattern has been observed for PedE (not shown).

3.1.4.2. PQQ locates in the center of the active site.

In the active-site region, an almost planar tricyclic ring of PQQ is sandwiched between a tryptophan W264PedE/W263PedH (π - π stacking hydrophobic interaction) and unusual disulfide bridge with 2 adjacent cysteines C121PedE/C131PedH and C122PedE/C132PedH (Van der Waals interaction) (**Figures 14A-C**). It forms a network of hydrogen bond with surrounding sidechain residues of the polypeptide including E77PedE/Q87PedH, R127PedE/R137PedH, T171PedE/S181PedH, S192PedE/A196PedH, G193PedE/G197PedH, D194PedE/G198PedH, S334PedE/D325PedH, R360PedE/R350PedH, N429PedE/N417PedH, W505PedE/W493PedH, and A569PedE/A557PedH (**Figure 14D**).

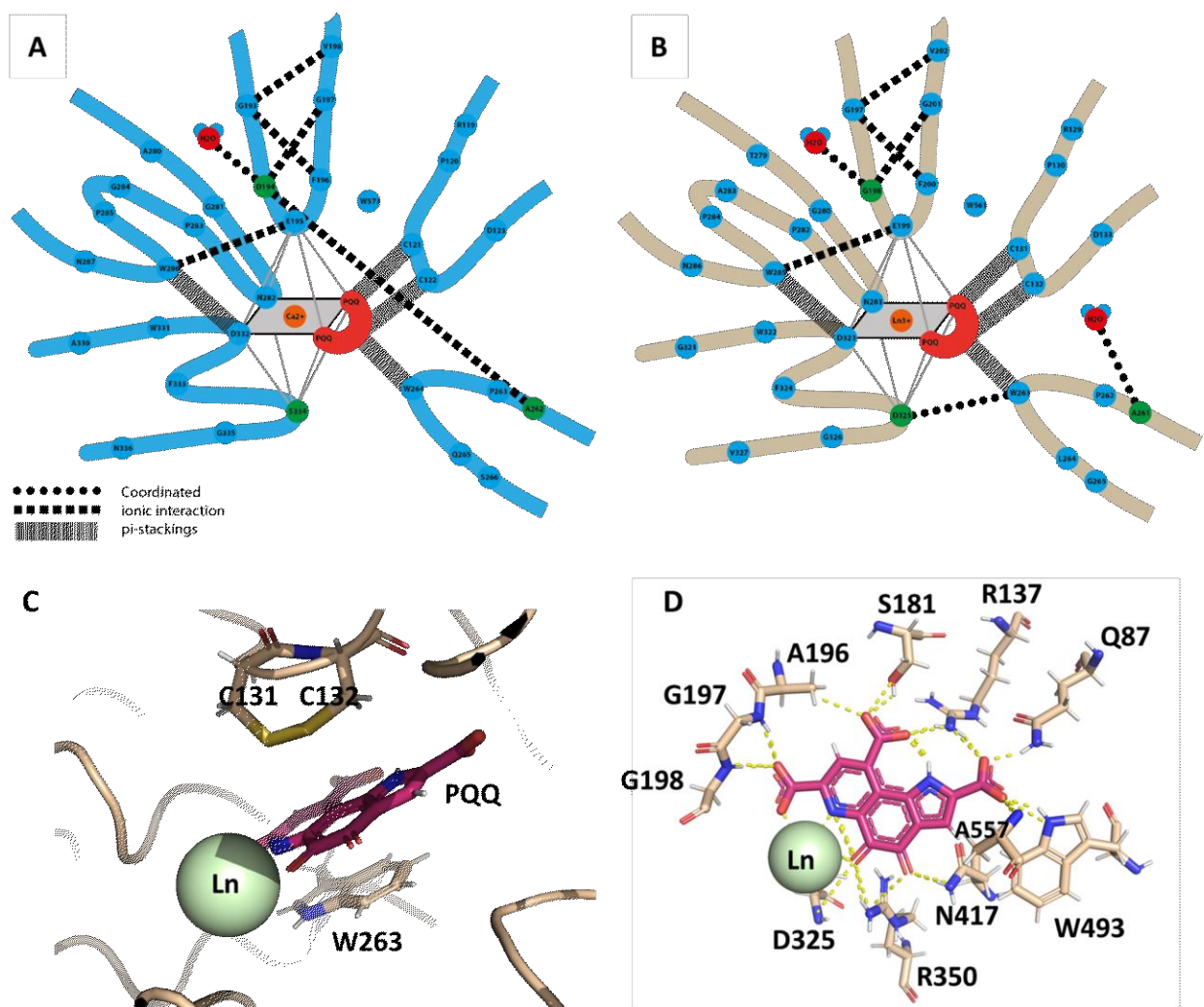


Figure 14. Coordination of PQQ in active site of PedE and PedH. A & B. Graphic representation of active site of PedE (colored cyan) and PedH (colored brown), respectively. **C.** π - π stacking and Van der Waals interaction of PQQ with W263 and C131C132 disulfide bridge of PedH, respectively. **D.** Polar Hydrogen bond interactions of PQQ with the surroundings amino acid residues of PedH shown in yellow dashed lines. The same pattern of C and D has been observed in case of PedE (not shown).

3.1.4.3. Substrate cavity of the active site

An electron density solved as acetate has been observed in the active site in the protein pocket of PedH. The substrate cavity is formed by a group of hydrophobic residues where W286PedE/W281PedH, F424PedE/F412PedH, L425PedE/L413PedH, A569PedE/A557PedH form its wall. A funnel-shaped channel, formed by the sidechains of C121PedE/C131PedH, E195PedE/E199PedH, W286PedE/W281PedH, F424PedE/F412PedH, L425PedE/L413PedH, A465PedE/A453PedH, L467PedE/L455PedH, A569PedE/A557PedH and F471PedE/F459PedH, represents the access to the substrate cavity (**Figure 15A**). A cover to the active site cavity has been provided by the bulky hydrophobic sidechain of W573PedE/W561PedH (**Figure 15B**).

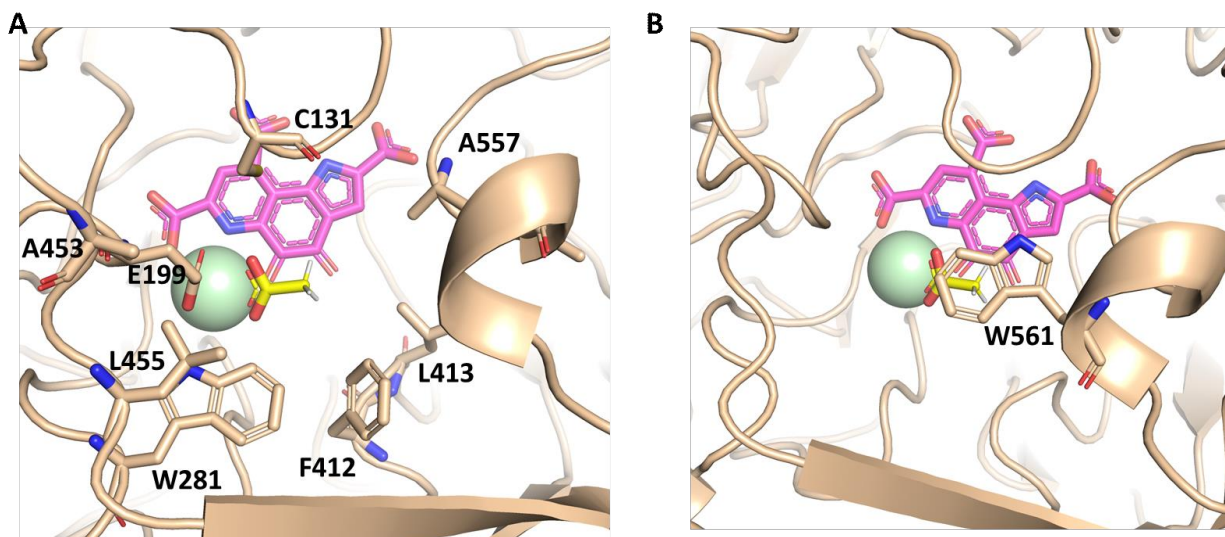


Figure 15. Substrate cavity of PedH. A. Amino acid residues form the funnel shaped channel for the substrate towards the active site. **B.** The bulky tryptophan covers the active site cavity. Acetate found in the active site colored in yellow. The same pattern has been observed in case of PedE.

3.1.4.4. Metal ion coordination of PedE and PedH

Closer inspection of the active sites revealed the respective metal ion tightly bound to the PQQ cofactor. Calcium showed a coordination number (CN) of 7 to E195PedE, N282PedE, D332PedE of the polypeptide and the O5, N6 and O7A atoms of the PQQ cofactor (**Figure 16A**). On the other hand, each of the lanthanide ions was coordinated in the same way, with a CN of 9 to amino acid side chains of E199PedH, N281PedH, D323PedH, and D325PedH of the polypeptide and the same atoms of the PQQ (**Figure 16B**). Although the overall architecture of the active site seemed to be almost identical, the conserved amino acid D325PedH/S334PedE appeared to be the defining amino acid by which PQQ-dependent ADHs can be distinguished into lanthanide or calcium dependent increasing the CN by 2 in case of the lanthanide ions.

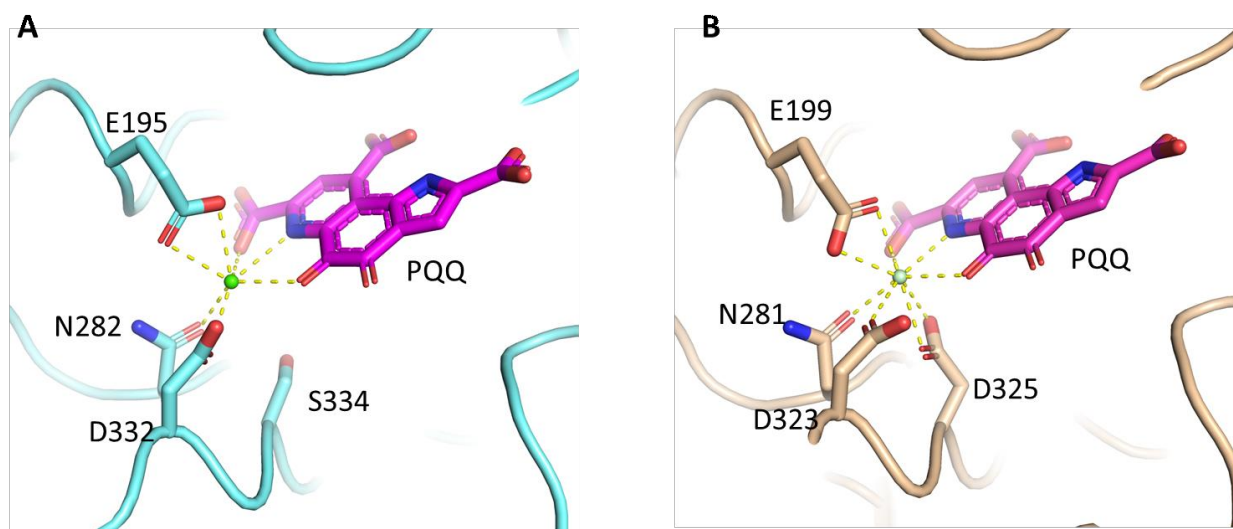


Figure 16. Comparison of the metal ion coordination in PedE (colored cyan) and PedH (colored brown). A. calcium colored green is coordinated as shown in yellow dashed lines through PQQ (shown in pink), E195, N282 and D332 of PedE. **B.** Ln colored pale green is coordinated through PQQ, E199, N281, D323 and D325 of PedH.

3.2. Functional analysis of PQQ/ADHs

It is elusive why *P. putida* KT2440 produce two redundant enzymes performing the same function. It should be that some clear benefit must exist to depend on an enzyme which is active with metals that are found at lower abundance while the same function could be fulfilled with an enzyme depending on the omnipresent calcium. To answer this question, mechanistic investigation of the periplasmic oxidation process by both Ca- and REEs- dependent PQQ-ADHs in *P. putida* KT2440 was aimed to be detected.

3.2.1. PedF is the cognate cytochrome for PedE and PedH.

3.2.1.1. *Ped* operon has a putative cytochrome-encoding gene (*PedF*).

The periplasmic oxidation process by the PQQ-dependent ADHs include electrons transfer from the substrate towards the PQQ cofactor, then to the respiratory complex chain through a c-type cytochrome. A detailed study to which electrons contribute to the activity of both ADHs extend was aimed to be performed. However, it is still not defined which enzyme represents the natural C-type cytochrome for PedE and PedH in *P. putida* KT2440.

Therefore, it was challenged to identify the cytochrome eventually serving as electron acceptor for both PQQ-ADHs, PedH and PedE. Analysis of the *ped* operon structure of the *P. putida* KT2440, which is involved in volatiles dehydrogenation and where PedE (PP_2674) and PedH (PP_2679) localize, shows also the presence of a putative cytochrome-encoding gene, named PedF (PP_2675) (**Figure 7**). The amino acid sequence derived from *pedF* identifies a protein of the periplasmic c-type cytochrome. It starts with a typical bacterial signal

peptide of 24 amino acids with the signal peptidase recognition site LLA. A typical heme-binding motif CXXCH is found at position 81 and methionine M127 or M130 could serve as the sixth ligand of the heme iron. The mature c-type cytochrome has 128 amino acids with calculated molecular mass of 13789 Da that is in close agreement with the previously reported *Ps. aeruginosa* c-type cytochrome [59].

3.2.1.2. Purification of the c-type cytochrome PedF.

To express functional PedF as a c-type cytochrome, it has to be in its mature form achieved by the covalent attachment of heme to the protein. The *ccmABCDEFGH* genes are responsible for maturation of cytochromes c. Even though these genes are present endogenously on the chromosome of *E. coli*, they are not expressed under aerobic conditions (shake flask). The plasmid pEC86 (CCOS Accession: CCOS 891) is a pACYC184 derivative containing the *E. coli* genes *ccmABCDEFGH* of the aeg operon expressed from the tet promoter of the plasmid. A mature c-type cytochrome can only be expressed in the holo-form (including heme) in an *E. coli* strain containing (i) pEC86 and (ii) the gene of target c-type cytochrome expressed from a compatible plasmid [60].

To do so, the gene encoding PedF (PP_2675) carrying an N-terminal hexahistidine tag without the nucleotides corresponding for the signal peptide PedF1-26 was cloned into pET-22b(+) vector that carries an N-terminal pelB signal sequence for potential periplasmic localization producing pET-22b-PedF to allow periplasmic proper folding of the cytochrome. Chemically competent *E. coli* BL21(DE3) cells were then co-transformed with pET-22b-PedF and pEC86.

The periplasmic extract only was used to purify the mature protein and then the protein was enriched via Ni-NTA-chromatography (**Figure 17A**) and purified further by SEC using a HiLoad 26/600 Superdex 200 column (**Figure 17B**) as

Results

detailed in chapter **5.2.3**. The collected reddish fractions were then tested for the heme binding to assure its maturation. Firstly, the heme staining of SDS-PAGE gel to check heme peroxidase activity using 3,3'-diaminobenzidine tetra-hydrochloride (DAB) where DAB is oxidized by hydrogen peroxide in the presence of heme-containing fractions, to generate a dark brown precipitate. This precipitate is exploited as a stain on the gel indicates the maturation of the PedF fractions (**Figures 17C & 17D**). Secondly, spectroscopic characterization (UV/visible absorption spectra of PedF) was performed as a typical mature c-type cytochrome peaks at 410 nm, 520 nm and 550 nm (**Figures 17E & 17F**). Only fractions of mature protein were then concentrated and flash freezed at -80 to further use it to set up experiments.

Results

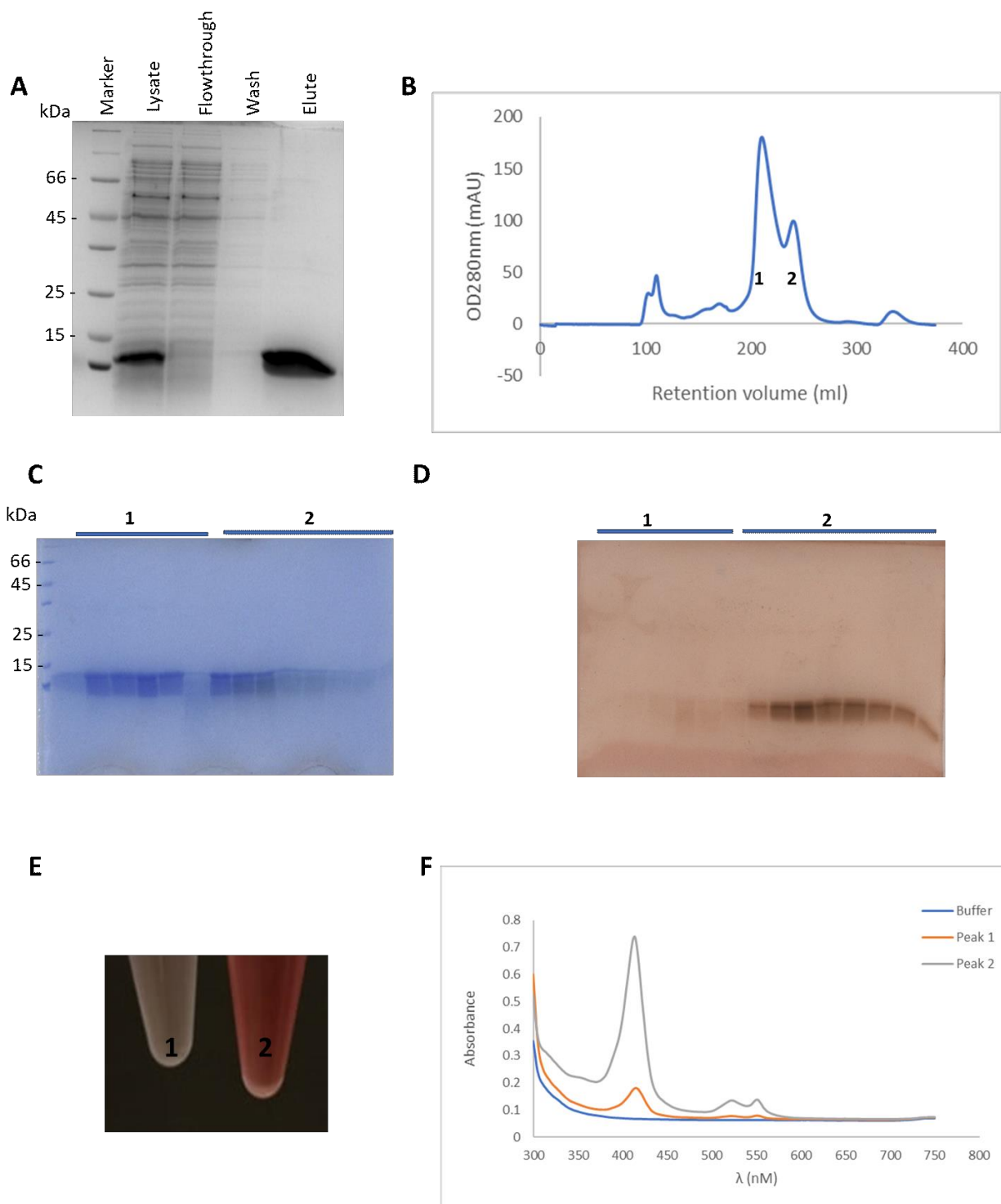


Figure 17. Purification of PedF. **A** represents the Coomassie-stained SDS-PAGE of IMAC on Ni-NTA column. **B** is the chromatogram from SEC. **C** and **D** are the respective SEC Coomassie-stained and heme peroxidase activity staining SDS-PAGE gels, respectively. **E** shows the color of the collected fractions. **F** represents spectroscopic characterization (UV/visible absorption spectra) of different PedF fractions.

3.2.1.3. Microscale thermophoresis of PedF towards PedE and PedH.

To challenge whether the PedF protein could indeed be the cognate electron acceptor of PedE and PedH, I aimed to investigate the possible binding between the cytochrome c (PedF) and each of the ADHs. The binding affinity was detected using MST as detailed in 5.2.9. PedF was titrated in concentrations ranging from (0-25 μM) on 200 nM of the ADH. PedH and PedE showed strong binding affinity to PedF with dissociation constant (K_d) of 70 ± 51.3 nM and 29.87 ± 23.5 nM respectively (Figure 18).

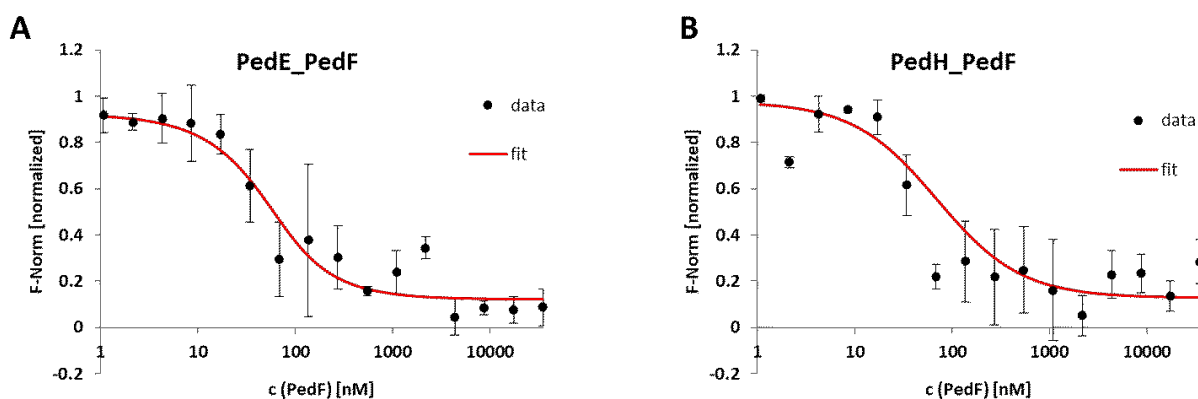


Figure 18. Binding affinity of PedF towards PedE (A) and PedH (B) using MST. The affinity in terms of dissociation constant (K_d) is calculated from the MST fitted curve that plots normalized fluorescence against concentration of PedF.

3.2.1.4. Activity measurement of PedE and PedH using PedF as their natural c-type cytochrome.

To further confirm that PedF could be the cognate c-type cytochrome for both ADHs (PedE and PedH), the activity of both ADHs was aimed to be detected using PedF as their natural c-type cytochrome. To do so, ferricyanide reductase assay protocol was adapted from Reichmann and Gorisch [61] with some modifications

Results

as detailed in chapter 5.2.7. In this assay, the proton is abstracted from the alcohol group by the ADH via the PQQ cofactor, and the electrons of the substrate are then transferred to the heme group of the PedF cytochrome then to ferricyanide as terminal electron acceptor. The reduction of Fe^{+3} leads to the formation of ferrocyanide with its Prussian blue which can be detected by its blue absorption. At low concentrations the low abundance of formed pigment hampers accurate determination of activity rates (**Figure 19**).

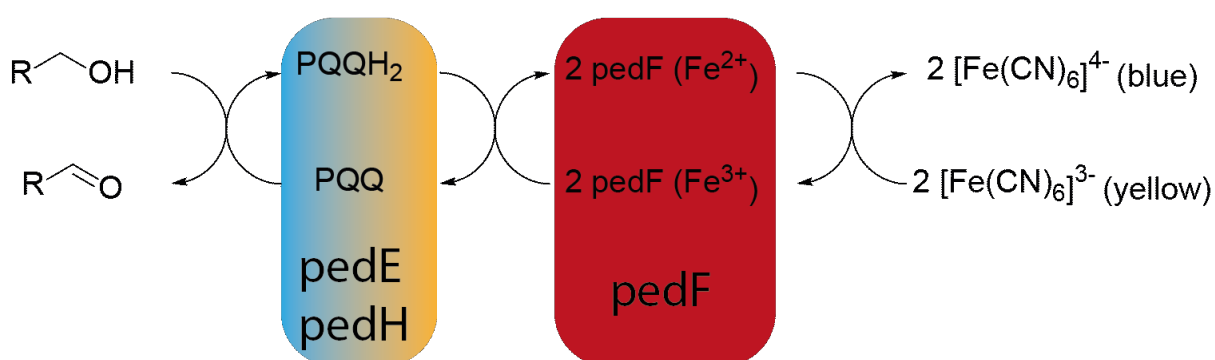


Figure 19. Graphic explanation of the kinetic characterization of PQQ-ADHs using their natural cytochrome PedF as electron acceptor. Alcohol is oxidized by the PQQ-ADHs (PedE or PedH colored cyan and brown). The resulted electrons from the substrate flow towards the PQQ of the ADH, then to Heme of the c-type cytochrome PedF colored red, and lastly to potassium ferricyanide as terminal electron acceptor. The reduction of Fe^{+3} leads to the formation of ferrocyanide with its Prussian blue which can be detected by its blue absorption.

Due to high affinity of ADHs towards its substrate, a concentration of 10 mM of ethanol as the substrate concentration is used to assure saturating conditions for both ADHs. From the affinities of the ADHs towards the metal cofactors, concentrations of 50 μM NdCl_3 and 50 mM CaCl_2 were extrapolated for as suiting concentrations for initial activity measurements. The activity assay clearly verified the suggestion that PedF represents the cognate cytochrome C550 for both PQQ-ADHs (**Figure 20**).

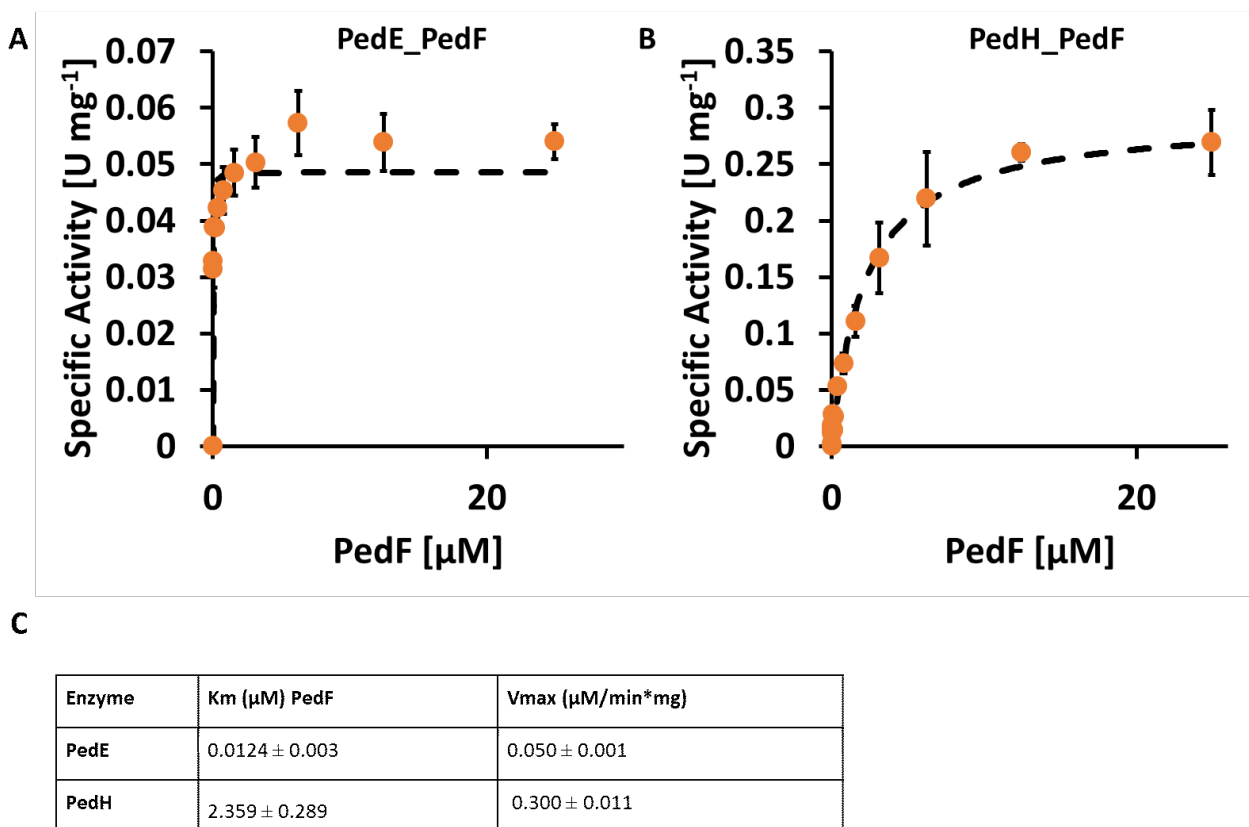


Figure 20. Activity measurements of PedE and PedH using PedF as their natural c-type cytochrome.

3.2.2. Kinetics of PedH and PedE towards ethanol as a substrate

Due to the fact that 2 cytochrome molecules are needed to accept both electrons released by one substrate molecule, a high turnover of PedF is needed in order to guarantee non-limiting reaction conditions. The initial activity measurements of both ADHs using PedF suggested that a concentration of 20 μM PedF is saturating the ADHs for further comparative kinetics measurements between the 2 enzymes. With the saturating reaction conditions, the kinetic parameters for both ADHs towards ethanol using 20 μM of PedF as their natural electron acceptor have been detected as detailed in chapter 5.2.7.

Results

Interestingly, the lanthanide-dependent PedH shows almost 6 times specific activity compared to its calcium-dependent counterpart PedE. The Michaelis constant (K_m) of ethanol towards PedH was approximately one third of that observed with PedE. In total, PedH showed almost 15 times catalytic efficiency as observed with PedE (**Figure 21**).

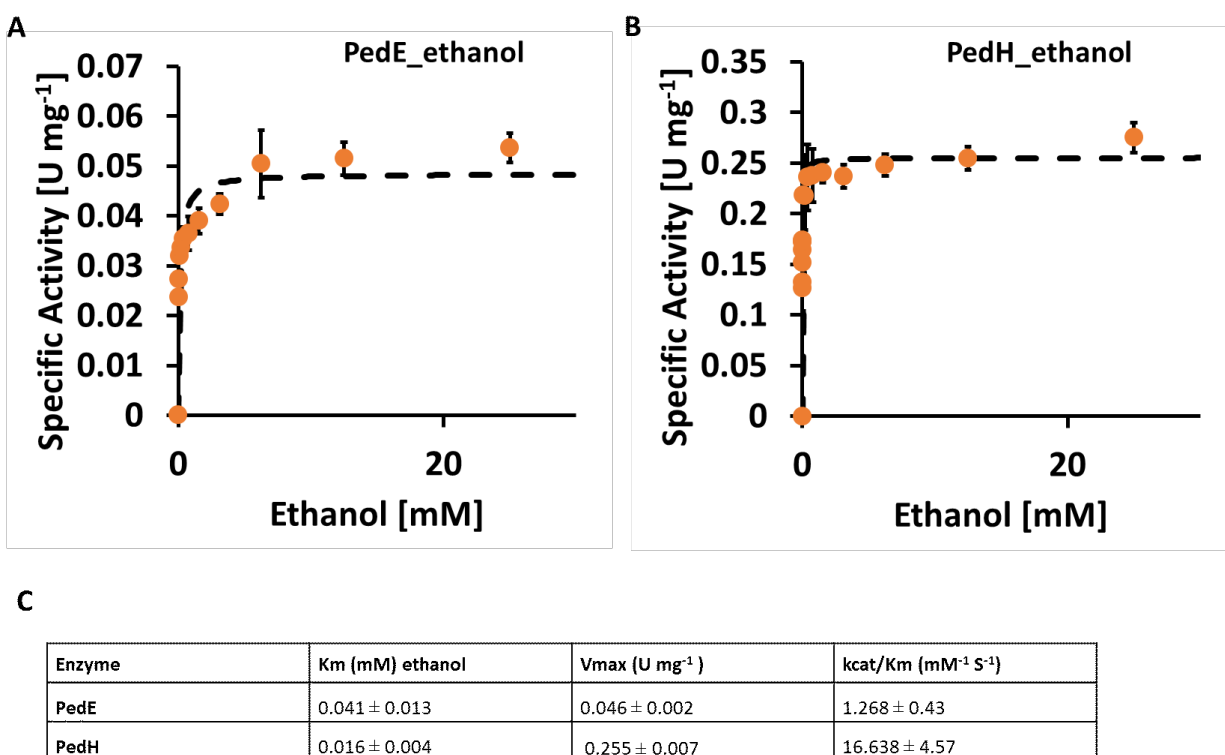


Figure 21. kinetic parameters and catalytic efficiency of PedE and PedH towards ethanol.

3.2.3. The REEs-dependent PedH can use calcium as a metal cofactor

Theoretically, calcium and early lanthanides share the same ionic radius and play the same role. A question is then raised how the REEs-dependent PedH could behave if REEs are not available in the surrounding environment. To get better

Results

insights, I wanted to compare the affinities and specific activities of both dehydrogenases while varying the metal cofactors.

It was interesting to find that K_d values of PedE and PedH towards calcium are on the same range that were $24 \pm 6.8 \mu\text{M}$ and $67 \pm 33.9 \mu\text{M}$, respectively. However, they showed 100 times different K_d values towards neodymium, as a representative for early lanthanides, that were $5 \pm 2.6 \mu\text{M}$ and $0.035 \pm 0.002 \mu\text{M}$ in case of PedE and PedH, respectively (**Figure 22**). On the other hand, specific activities of both ADHs varying the metal cofactor were detected with the same set up of the kinetic measurement in presence of 10 mM ethanol as the substrate concentration using 20 μM PedF. Surprisingly, both ADHs were active to the same degree in presence of CaCl_2 , but strikingly the PedH showed an almost 10 times higher activity than PedE in presence of NdCl_3 (**Figure 22**).

It can be therefore concluded that both ADH are active in presence of calcium, but the PedH is optimized towards performing the dehydrogenation in presence of neodymium with a much more efficient way compared to the PedE. Presented with these findings I tried to identify the reasons for such observed activity in molecular and structural level.

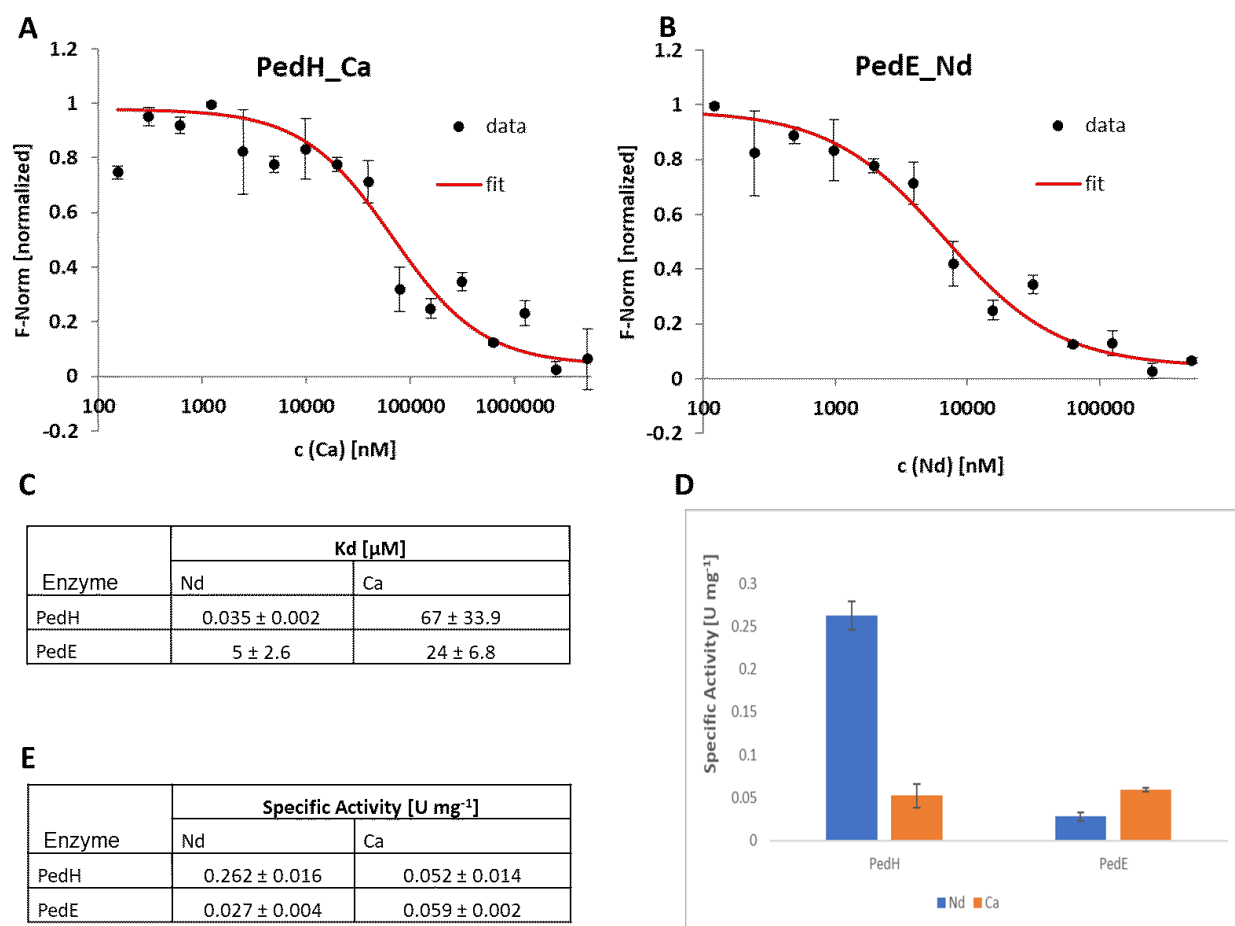


Figure 22. MST and specific activity of PedH and PedE in different metal conditions. **A** and **B** represent binding affinities of PedH (**A**) and PedE (**B**) towards calcium (Ca) and Neodymium (Nd), respectively. **C** shows the affinity in terms of dissociation constant (K_d) is calculated from the MST fitted curve that plots normalized fluorescence against concentration of the metal of interest. **D** and **E** show the specific activity performed for both ADHs in different metal conditions.

3.2.3.1. Crystallization of PedH in presence of calcium shows an active site glutamate switch.

The EDTA-treated metal-free PedH was cocrystallized in presence of PQQ and calcium on the same way previously described in chapter 3.1.3. The same lattice, previously observed in all different co-crystallized lanthanides, has been observed

Results

within 24 hours in 0.2 M ammonium sulfate, 0.1 M sodium acetate pH 4.6, 25 % (w/v) PEG 4000 condition. The produced crystal lattice was determined at resolution of 1.65 Å and determined as space group $P4_32_12$. The structures were refined to an $R_{\text{work}}/R_{\text{free}}$ of 14.64/16.39 (**Table 4**).

A detailed analysis of the metal coordination spheres for PedH surprisingly showed significant differences between calcium and lanthanide ions. The conserved glutamate E199PedH that completes the coordination sphere of lanthanide ion (CN=9) switches away from the coordination sphere of the calcium ion returning it to a CN of 7 that is similar to that in case of PedE but through different residues. In other words, PedH could coordinate Ca^{+2} with a CN of 7 to amino acid side chains of N281PedH, D323PedH, and D325PedH of the polypeptide and the O5, N6 and O7A atoms of the PQQ cofactor (**Figures 23A-C**).

Interestingly, PedH has a glycine residue (G198PedH) directly before the switched glutamate residue (E199PedH) that is not the case in case of PedE that has the bulky aspartate residue (D194PedE). The alignment of several known lanthanide-dependent PQQ-ADHs and several known calcium-dependent PQQ-ADHs showed that the former group has such conserved glycine residue directly before the proposed switched glutamate compared to a bulkier aspartate or alanine in case of the second group (**Figure 23D**). Therefore, It could be suggested that G198PedH could play a role in its adaption towards the calcium dependence by providing a flexible space to the metal coordinating glutamate E199PedH to freely switch according to the metal inside the active site pocket compared to the bulkier D194PedE containing loop.

A detailed analysis of the metal coordination spheres for PedH surprisingly showed significant differences between calcium and lanthanide ions. The conserved

Results

glutamate E199PedH that completes the coordination sphere of lanthanide ion (CN=9) switches away from the coordination sphere of the calcium ion returning it to a CN of 7 that is similar to that in case of PedE but through different residues. In other words, PedH could coordinate Ca^{+2} with a CN of 7 to amino acid side chains of N281PedH, D323PedH, and D325PedH of the polypeptide and the O5, N6 and O7A atoms of the PQQ cofactor (**Figures 23A-C**).

Interestingly, PedH has a glycine residue (G198PedH) directly before the switched glutamate residue (E199PedH) that is not the case in case of PedE that has the bulky aspartate residue (D194PedE). The alignment of several known lanthanide-dependent PQQ-ADHs and several known calcium-dependent PQQ-ADHs showed that the former group has such conserved glycine residue directly before the proposed switched glutamate compared to a bulkier aspartate or alanine in case of the second group (**Figure 23D**). Therefore, It could be suggested that G198PedH could play a role in its adaption towards the calcium dependence by providing a flexible space to the metal coordinating glutamate E199PedH to freely switch according to the metal inside the active site pocket compared to the bulkier D194PedE containing loop.

Table 4. Data collection and refinement statistics of PedH in presence of Ca.

	PedH, Ca
Data collection	
Space group	P4 ₃ 2 ₁ 2
Cell dimensions	
<i>a, b, c</i> (Å)	105.51 105.51 187.18
α, β, γ (°)	90 90 90
Wavelength (Å)	0.976253
Resolution (Å)	47.19 - 1.65 (1.71 - 1.65)
<i>R</i> _{merge}	0.1113 (1.371)
<i>I</i> / σ <i>I</i>	23.78 (1.97)
Completeness (%)	99.73 (97.66)
Redundancy	25.9 (22.7)
<i>CC</i> _{1/2}	1 (0.738)
Refinement	
Resolution (Å)	47.19 - 1.65
No. reflections	126340 (12209)
<i>R</i> _{work} / <i>R</i> _{free}	0.146/0.163
No. atoms	
Protein	4361
Ligand/ion	29
Water	510
B-factors	
Protein	25.96
Ligand/ion	24.54
Water	22.77
R.m.s. deviations	
Bond lengths (Å)	38.27
Bond angles (°)	0.020
Ramachandran	
Favored (%)	2.16
Allowed (%)	95.90
Outliers (%)	3.57
	0.53

*Values in parentheses are for highest-resolution shell.

Data were collected on MX14.2 (BESSY).

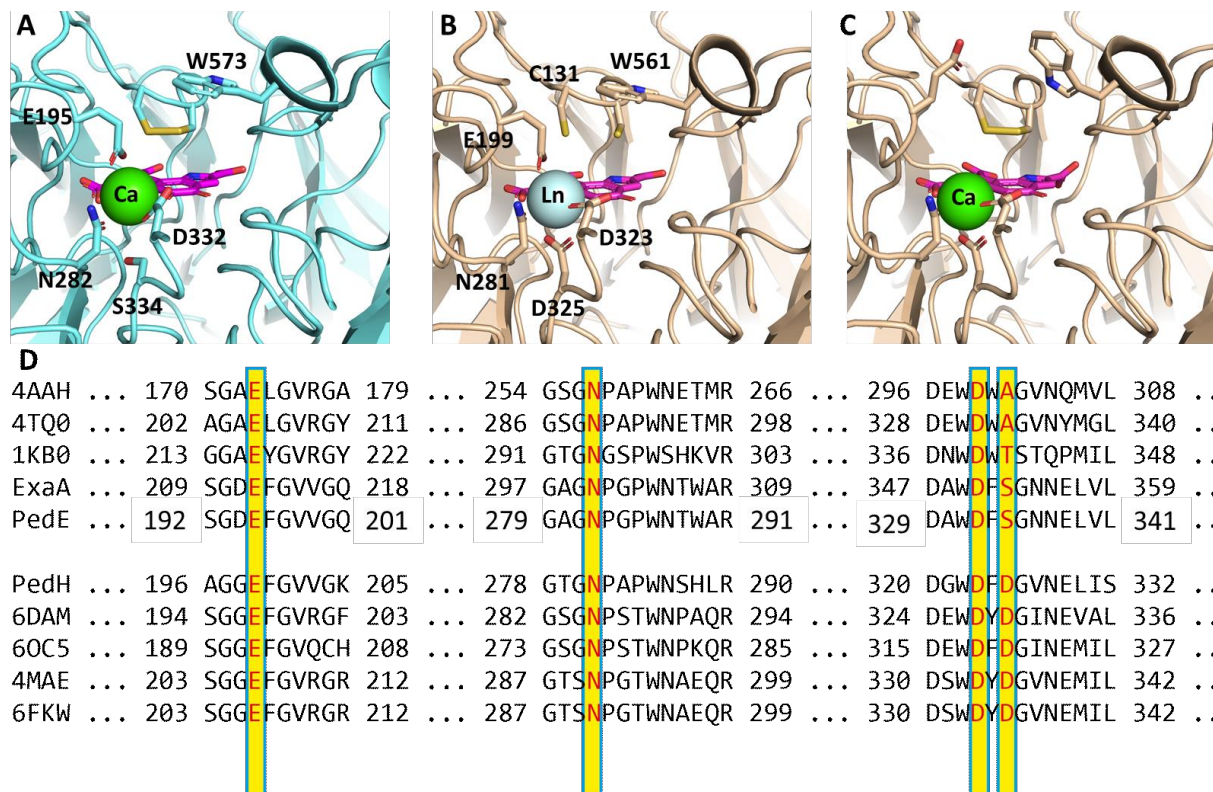


Figure 23. Comparison of different metal ion coordination in the active site of PedE and PedH. **A.** Calcium ion (colored green) coordination in case of PedE (colored cyan). **B and C** are the coordination of Ln (colored sky blue) and calcium (colored green), respectively in case of PedH (colored brown) where the disulfide bridge, E199, and W561 showed conformational switch from its position outwards in the upper direction. **D.** Alignment of different lanthanide-dependent PQQ-ADHs [24], [62]–[64] including PedH and calcium-dependent PQQ-ADHs [57], [65]–[67] including PedE with residues involved in the metal ion coordination shown in red and highlighted in yellow.

3.2.3.2. Quantum chemical calculations explain the orientation preference of PedH depending on the metal cofactor.

In close collaboration with Dr. Florian Weigend and Kevin Reiter at the Philipps-University Marburg, the preferences for the two different orientations of the glutamate (E199PedH/E195PedE) unit for metal (M)=Ca/Nd were elucidated by quantum chemical calculations. Models were considered for the active centers of PedH and PedE with the carboxyl group of the glutamate unit oriented towards the

Results

metal ion in the center in the “closed” (**Figures 24A & 24C**) and away from it in the “open” conformation (**Figures 24B & 24D**). The structure parameters were optimized, but the atoms binding to the backbone labelled in (**Figure 24**) were kept fixed at the positions obtained from the X-ray structure of the Ca compound. The H^+ ions binding to the carboxyl groups were omitted; instead, the negative charge was simulated by the conductor-like screening model (COSMO) [68]. This most closely resembles the experimental situation. In this way, for metal ions of formal oxidation states of I to IV total charges amount to -5 to -2 .

The energy differences ΔE for PedH and PedE between the “closed” and “open” conformations were calculated for $M=Ca, Nd$ and for no metal ion in the center (for the structure parameters optimized for Ca). For PedH, moreover the energy differences ΔE were calculated for $M=$ sodium (Na), cadmium (Cd), Mercury (Hg), Bismuth (Bi) and Thorium (Th), additionally. They are listed in **Table 5**; negative values indicate preferences for the closed orientation, structures A or C, respectively. Obviously, in the case of PedH, the preference for the specific orientation is well correlated to the oxidation state of the metal ion. For MIII ions, to approximately -67 kJ/mol and for MII ions it is close to zero. In contrast, for the MI ion orientation B is preferred by 45 kJ/mol, and without any metal ion in the center even by 170 kJ/mol.

This overall indicates that the respective preferences are due to electrostatic reasons. This is confirmed by the estimation of ΔE from the difference of the electrostatic potential for the two orientations at the center of the model without a metal ion. It amounts to -100 kJ/mol per elementary charge. This leads to values for ΔE of $+70/-30/-130$ kJ/mol for ions of formal oxidation states I/II/III, respectively. This is in reasonable agreement with the explicitly calculated data above. Of course, the partial charges (**Table 5**) are smaller than the formal

Results

oxidation states by roughly a factor of two. Thus, the preference of A is smaller than predicted by the simple calculation basing on formal oxidation states.

In the case of PedE without any metal ion in the center, the opened structure D is preferred, but only by 130 kJ/mol, indicating less repulsion between the coordinating oxygen atoms in PedE compared to PedH. The estimated energy gain resulting from the difference of the electrostatic potential for the two orientations C and D at the center of the model without a metal ion amounts to -126 kJ/mol per elementary charge. Here, already the first formal oxidation state almost entirely compensates the repulsion due to the negatively charged oxygen atoms. The closed structure of PedE, C, is preferred by roughly 30 kJ/mol for Ca^{2+} and by approximately 110 kJ/mol for Nd^{3+} .

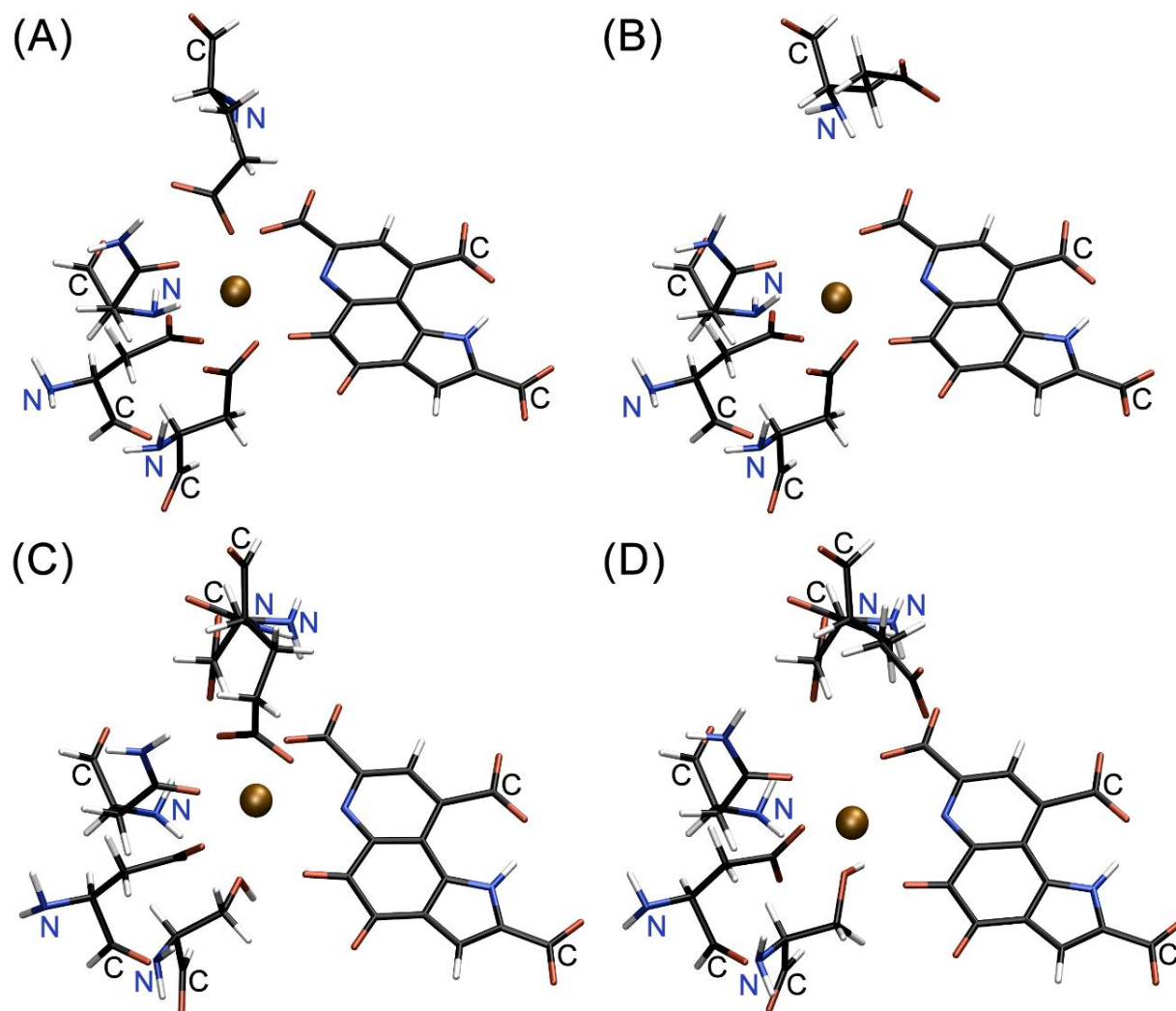


Figure 24. Models for the active centers of PedH (top row) and PedE (bottom row). The carboxyl group of the glutamate unit oriented towards the metal ion in the center (A and C) and away from it (B and D). The explicitly labeled atoms are fixed during the structure optimizations.

Results

Table 5. Energy differences ΔE between the two orientations of the glutamate (E199PedH/E195PedE) unit for selected metal ions as well as for no metal ion in the center (for the structure parameters optimized for Ca). In the third column the partial charge, Q, from a Mulliken analysis for orientation A (PedH) and C (PedE) is given. Additionally, the Pauling electronegativity, EN.

PedH			
M	ΔE / kJ/mol	Q	EN [69], [70]
Th ^{IV}	-121.3	2.11	1.3
Nd ^{III}	-67.7	1.92	1.14
Bi ^{III}	-47.1	1.44	2.02
Ca ^{II}	-5.2	1.22	1.00
Cd ^{II}	-2.5	1.14	1.69
Hg ^{II}	1.5	0.95	2.00
Na ^I	44.7	0.58	0.93
-	171.6	-	-
PedE			
M	ΔE / kJ/mol	Q	EN
Nd ^{III}	-110.7	1.93	1.14
Ca ^{II}	-31.6	1.23	1.00
-	132.2	-	-

3.2.3.3. PedH molecular switch changes its electrostatic surface charge at the binding interface with PedF

3.2.3.3.1. Change of PedH electrostatic surface charge at the disulfide bridge side.

Besides the E199PedH switch in the active site region, W561PedH also showed a switch from its position on the same direction where the E199PedH switched (**Figure 23**). Interestingly the switch of these amino acids was on the side of the conserved disulfide bridge, and which thought to play an important role for the electron transfer from the PQQH₂ towards the cytochrome. Moreover, it was interesting to observe a red electron density on the bridge of the disulfide and green electron densities both on its sides and on the upper side of the carbonyl of the peptide group connected to the next amino acid D133 in all Ln solved structures of PedH that was not the case in case of calcium state of PedH (**Figures 25A & 25B**). This revealing that the thiol groups of C131 and C132 should not be linked, and the carbonyl of the peptide group connected to the next amino acid D133 should be oriented to the surface in the upper direction and not to the inner direction towards the PQQ.

Careful inspection of the electrostatic surface charge map of both states generated by Pymol at this disulfide bridge side showed a clear difference between the 2 states where PedH surface is partially charged in its open form in presence of calcium rather than its closed form in presence of lanthanides as a result of the PedH residues switch not only in the active site region but also in the surface of PedH polypeptide (**Figures 25C & 25D**).

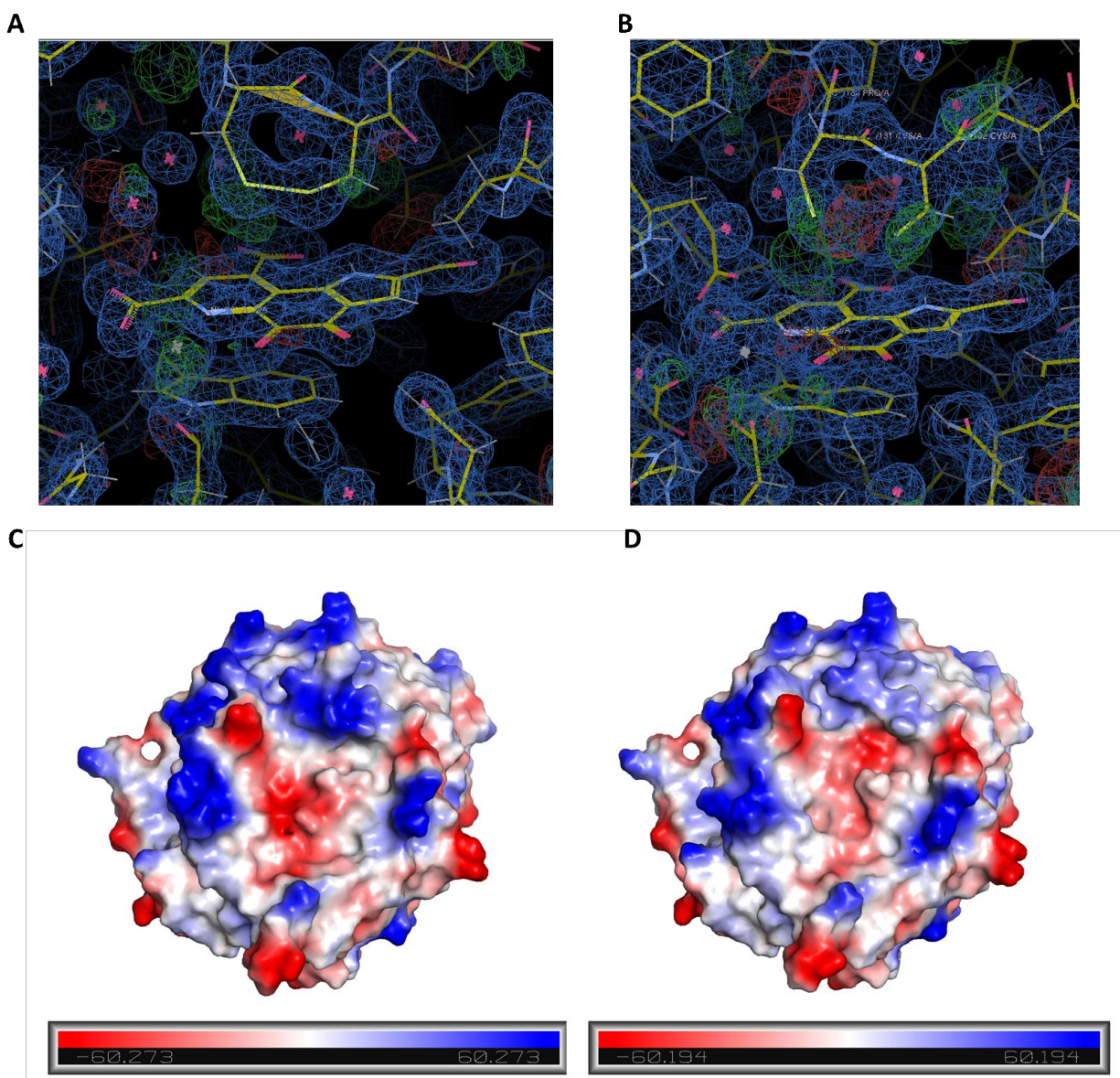


Figure 25. PedH molecular switch changes its electrostatic surface charge at the binding interface with PedF. A & B. Comparison of the disulfide bridge in both states of PedH according to the metal ion on the active. **A.** Calcium state of PedH, the disulfide bridge formed, and the carbonyl of the peptide group connected to D133 oriented inside towards the PQQ. **B.** Lanthanide state of PedH, red electron density on the bridge of the disulfide and green electron density both on its sides and on the upper side of the carbonyl of the peptide group connected to the next amino acid D133 revealing that the thiol groups of C131 and C132 were not linked, and the carbonyl of the peptide group connected to the next amino acid D133 in the upper direction to the surface not to the inner direction towards the PQQ. **C & D.** Comparison of the electrostatic surface charge of PedH at the disulfide bridge side in presence of calcium (**C**) and lanthanides (**D**).

3.2.3.3.2. The disulfide bridge side of PedH represents the PedH/PedF binding interface.

It is therefore hypothesized that this change of the surface charge of the open form of PedH could affect the binding between PedH and PedF and/or disrupt the pathway by which electrons transfer from the reduced PQQ towards the Heme in PedF. To validate the binding interface between the PedF cytochrome and the PedH alcohol dehydrogenase, Hydrogen-deuterium exchange (HDX) coupled to mass spectrometry (MS) was conducted in close collaboration with Dr. Wieland Steinchen at the Philipps-University Marburg. Hereby, PedF and PedH were mixed in equimolar ratio and subjected to HDX through incubation in deuterated buffer for different time points, digested with pepsin and the amount of deuterium incorporated was analyzed by electrospray ionization-mass-spectrometry as further detailed in chapter 5.2.10. Individual states of PedF and PedH treated similarly served as control and the changes in deuterium incorporation upon binding of PedH to PedF was investigated. Data analysis was carried out using PLGS and DynamX 3.0 softwares (both from Waters).

A total of 47 peptides have been detected in case of PedF that covered 85.3% coverage with 5.85-fold redundancy per amino acid (**Figure 26**). Comparison of the HDX of individual and PedH-bound PedF revealed multiple peptides with decreased HDX in the former, that mainly encompassing helices 1 and 2, the loop interconnecting helices 3 and 4 and a portion of helix 4. Given that the N-terminal part of PedF was entirely unaltered in complex with PedH and the location where the HDX reduction observed, we could expect that these regions involved in the binding of PedF to PedH should be close to the Heme binding site (**Figure 27**).

Results

On the other hand, 116 peptides of PedH have been recovered with 92.5% of the amino acid sequence and 3.59-fold redundancy per amino acid (**Figure 28**). Interestingly, scattered regions with different increased HDX profiles of PedH when in complex with PedF have been observed compared to its alone state. This could suggest a conformational change of PedH in case of complex compared to the PedH-alone state. Taking into consideration that the increased HDX regions detected in the terminals together with the peptides surrounding PQQ, this could be explained that the PedH/PedF complex could result in change of the dimerization state of PedH and its binding to PQQ making it more exposed for HDX (**Figure 29**).

In addition, it was interesting to find that the areas of reduced HDX profiles on PedF alone state compared to PedH/PedF complex are in good agreement with the interaction interface between the two domains of the previously published structure of QbdA enzyme, a type II quinohemoprotein alcohol dehydrogenase in *Pseudomonas putida* HK5 (PDB code: **1KV9**) [66]. This enzyme has a PQQ-binding domain together with an internal cytochrome domain. Superimposition of PedF structural model and PedH and onto the cytochrome binding domain and the PQQ binding domain of 1KV9 “chimeric PedH/PedF complex”, respectively, confirms that the disulfide bridge side represents the interface through which the PedH/PedF complex is formed for the electron transfer (**Figures 27,29 & 30**).

Taken together, two different kind of interactions via salt bridges and hydrophobic clusters could be established facilitating the interaction between the 2 protein. D132PedF&R129PedH, K129PedF&D127PedH and R99PedF&D571PedH represent potential amino acid side chains that could be critical in establishing the PedF/PedH interactions via salt bridges. Y126PedF&V134PedH, I94PedF&Y103PedH and Y133PedF&F454PedH form a bunch of hydrophobic clusters (**Figure 30**).

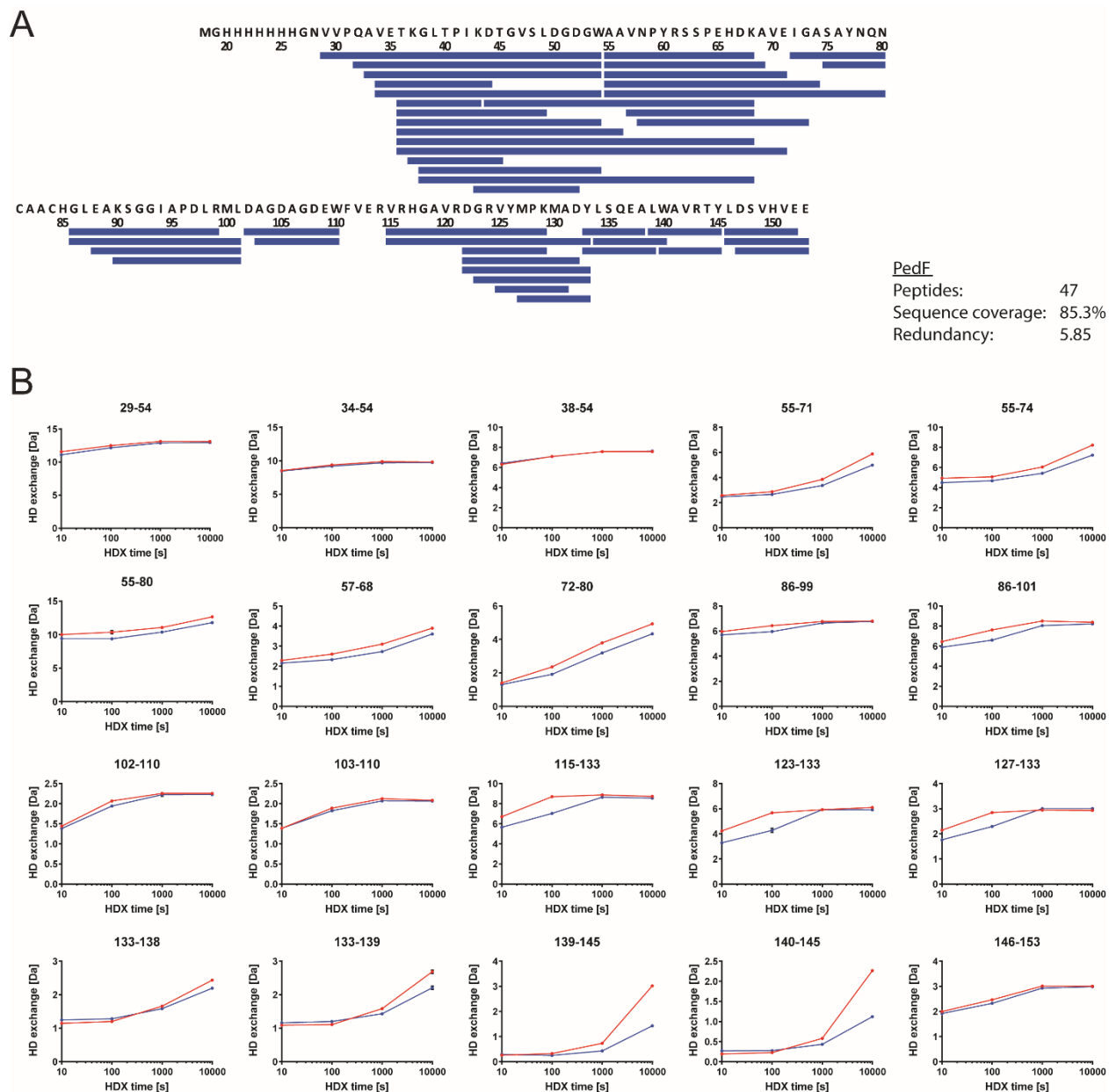


Figure 26. HDX-MS of PedF. A. Peptides of PedF analyzed for their HDX are indicated as blue bars and plotted on the amino acid sequence of PedF. **B.** Deuterium incorporation of representative PedF peptides for individual PedF (red) or the PedF/PedH complex (blue). Data represent mean \pm SD of three technical replicates (individual HDX reactions) for each time-point.

Results

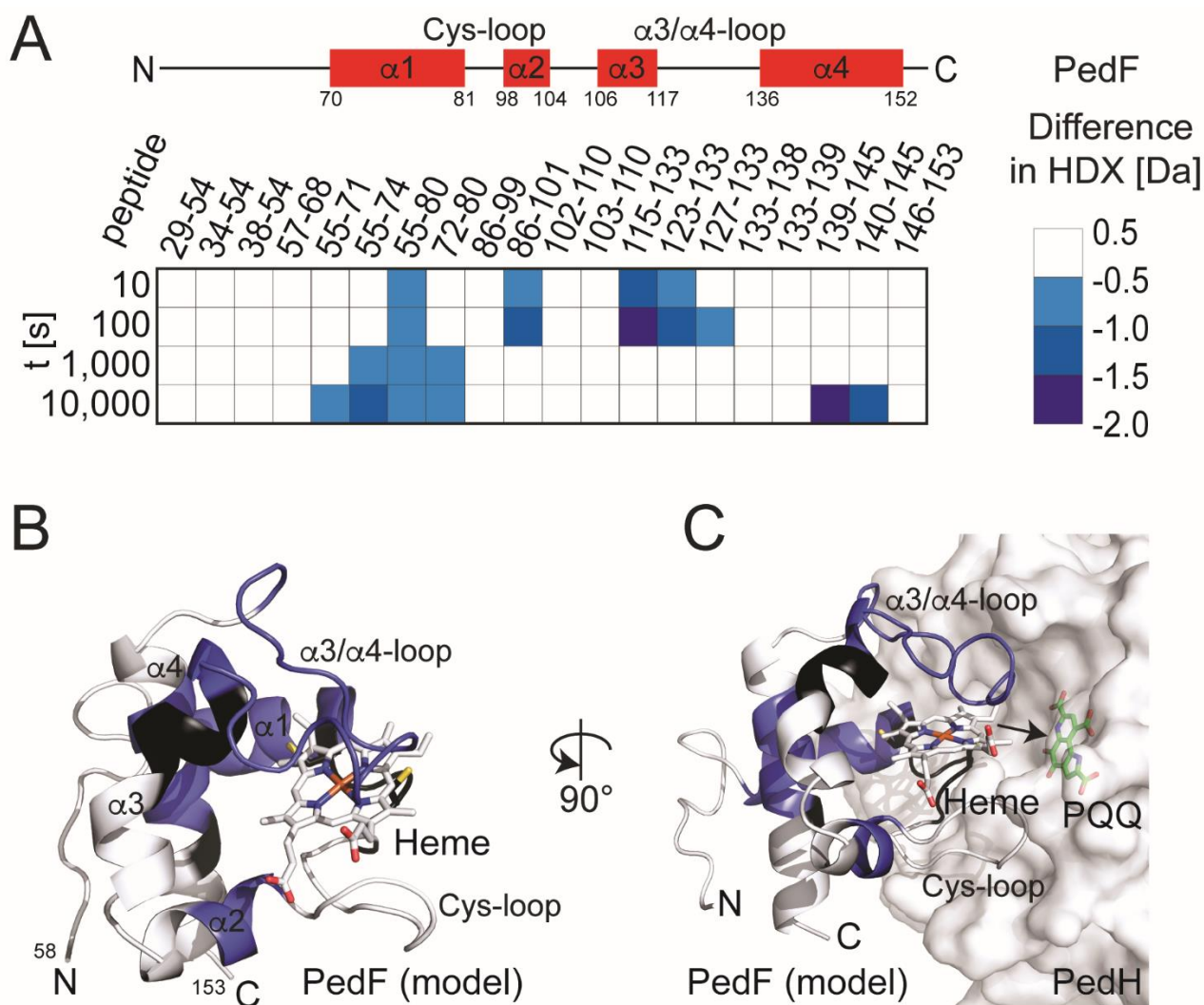


Figure 27. The binding interface of PedF in the PedF/PedH complex. A. Representative peptides of PedF are colored according to their difference in HDX between the PedF/PedH complex and individual PedF. The secondary structure of PedF indicated above is based on a structural model of PedF generated with SwissModel with the structure of cytochrome c_L from *Hyphomicrobium denitrificans* (PDB-ID: 2D0W) as template [71]. Numbers denote amino acid residues. **B.** Areas of PedF that exhibited reduced HDX at at least one time-point are colored in blue in the structural model of PedF (see above). Areas not covered by peptides in HDX are colored in black. **C.** Expected topology of the PedF/PedH complex. The PedF structural model was superimposed with the cytochrome c -like domain of the quinohemoprotein alcohol dehydrogenase QbdA from *Pseudomonas putida* (PDB-ID: 1KV9) and is colored as in panel B. The crystal structure of PedH was superimposed with the alcohol dehydrogenase domain of QbdA and is shown as grey surface. The ligand pyrroloquinoline quinone (PQQ) residing in the active site of PedH is shown as sticks.

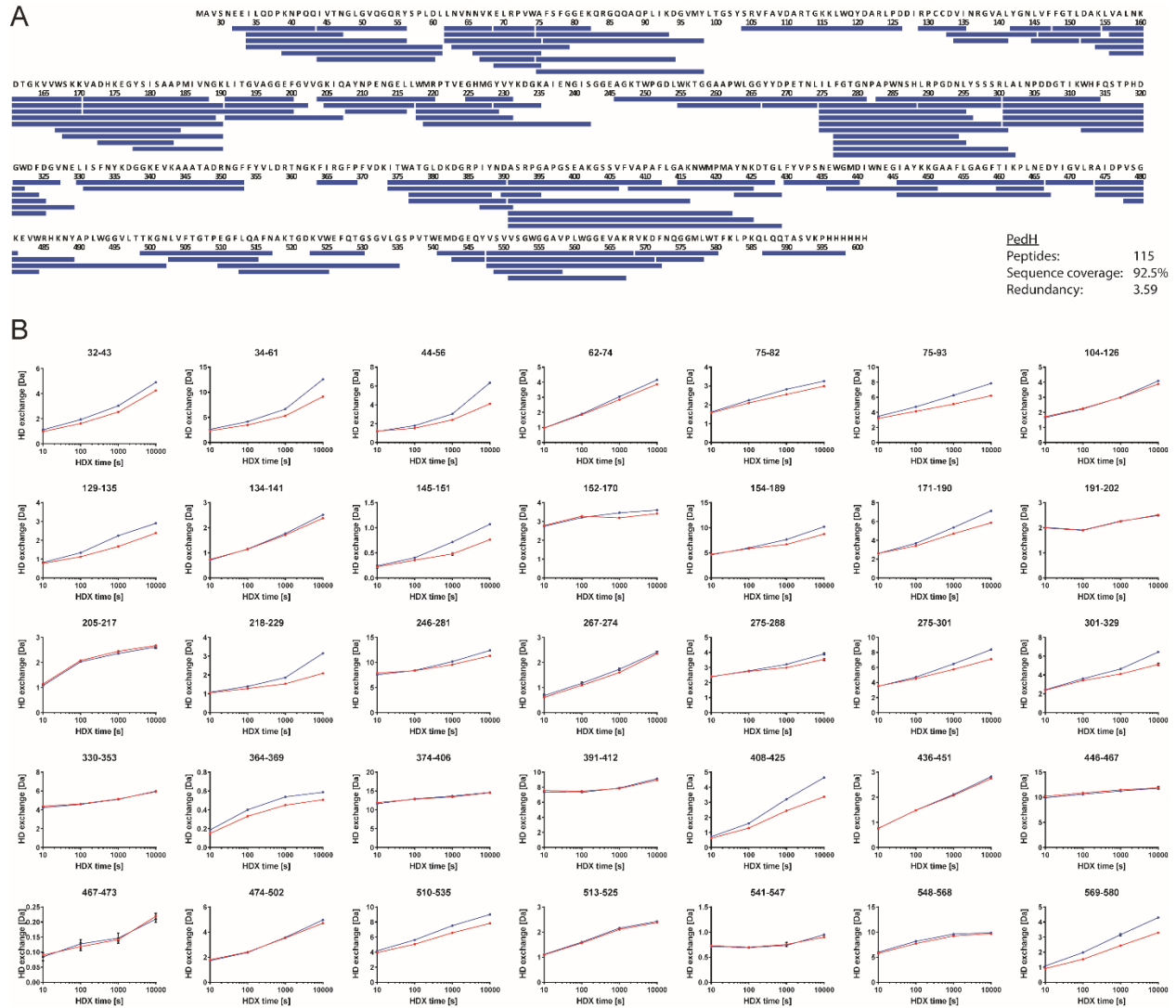


Figure 28. HDX-MS of PedH. A. Peptides of PedH analyzed for their HDX are indicated as blue bars and plotted on the amino acid sequence of PedH. **B.** Deuterium incorporation of representative PedH peptides for individual PedH (red) or the PedF/PedH complex (blue). Data represent mean \pm SD of three technical replicates (individual HDX reactions) for each time-point.

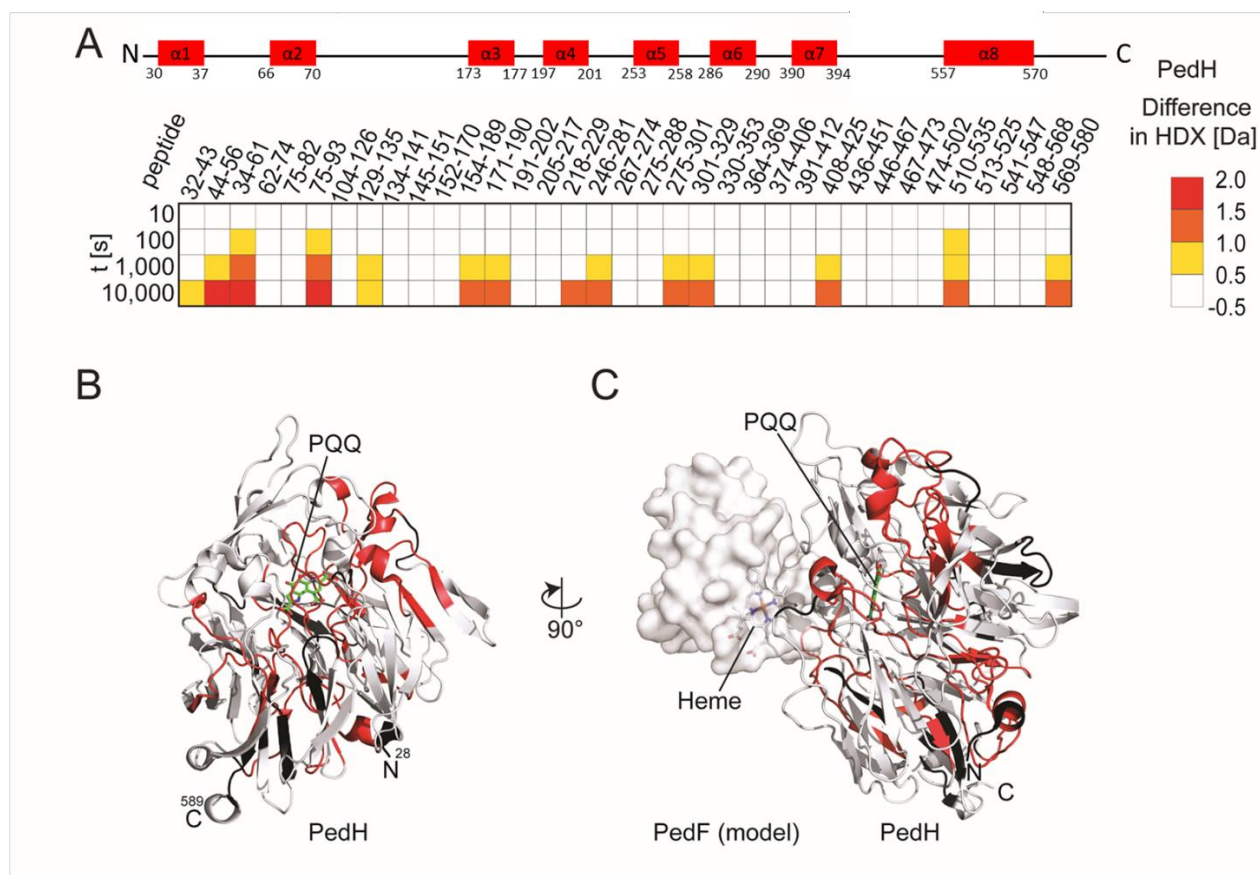


Figure 29. Conformational changes of PedH in the PedF/PedH complex. A. Representative peptides of PedH are colored according to their difference in HDX between the PedF/PedH complex and individual PedH. The topology of PedH is indicated above. **B.** Areas of PedH that exhibited increased HDX at at least one time-point are colored in red in the crystal structure of PedH. Areas not covered by peptides in HDX are colored in black. **C.** Expected topology of the PedF/PedH complex. The PedF structural model was superimposed with the cytochrome c-like domain of the quinoxinoprotein alcohol dehydrogenase QbdA from *Pseudomonas putida* (PDB-ID: 1KV9) and is colored as in panel B. The crystal structure of PedH was superimposed with the alcohol dehydrogenase domain of QbdA and is shown as grey surface. The ligand pyrroloquinoline quinone (PQQ) residing in the active site of PedH is shown as sticks.

Results

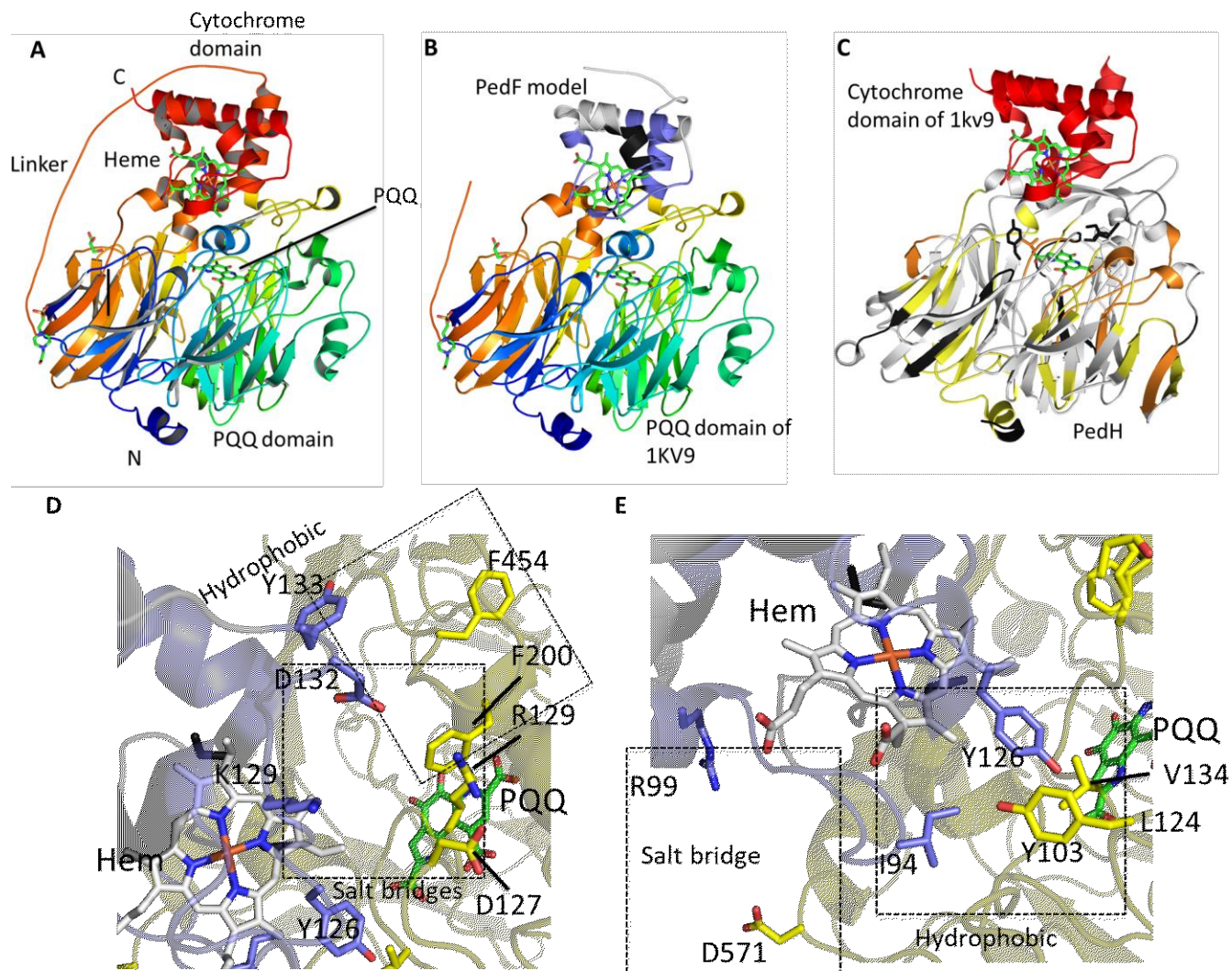


Figure 30. Expected topology of the PedF/PedH complex. **A.** Cartoon structure of quinohemoprotein alcohol dehydrogenase QbdA from *Pseudomonas putida* (PDB-ID: 1KV9) coloured in rainbow with the N-terminus in blue and C-terminus in red. **B.** The PedF structural model was superimposed with the cytochrome c-like domain of the QbdA with areas of PedF that exhibited reduced HDX are colored in blue. **C.** The crystal structure of PedH was superimposed with the alcohol dehydrogenase domain of QbdA and is shown as grey surface with areas showed increased HDX in yellow and brown. Areas not covered by peptides in HDX are colored in black. **C-D.** Potential amino acid side chains that could be critical in establishing the PedH/PedF interactions via salt bridges and hydrophobic clusters (boxed).

3.2.3.3.3. Different patterns of PedH/PedF binding depending on the metal cofactor.

To further investigate if the change of the electrostatic surface charge of PedH caused by presence of calcium is affecting the binding towards the PedF, the MST of PedH towards PedF had been measured in presence of different metal states. Different concentrations of PedF (0- 25 μM) were titrated on 200 nM of PedH in different metal conditions (no metal, 100 μM Ca or 10 μM Nd). Interestingly, the K_d values were almost the same in nanomolar range (50-70 nM) in the three conditions, however different patterns of binding between PedF and PedH have been detected (**Figure 31**). In presence of Nd, PedH-PedF complex showed slower movement than the PedH alone and this is reversed in case of non-metal and calcium where the complex had faster movement compared to the PedH alone. This could suggest that PedH can still bind PedF in both states, however, the way by which both proteins bind differs according to the metal ion inside the active site that results into the different states of PedH.

Therefore, I have challenged that a variant of PedH disrupting the disulfide bridge could have the same behavior of PedH in presence of Nd towards PedF. PedH_C132S variant has cloned, purified and its binding towards PedF using MST has measured in absence of metals as previously described. Interestingly, PedH_C132S variant as assumed showed the same pattern of PedH towards PedF only observed in presence of Nd with a reported K_d value of 45.82 ± 16.15 nM (**Figure 31**). Therefore, the pathway by which electrons transferred from reduced PQQ towards the Heme in PedF could be different in the 2 states.

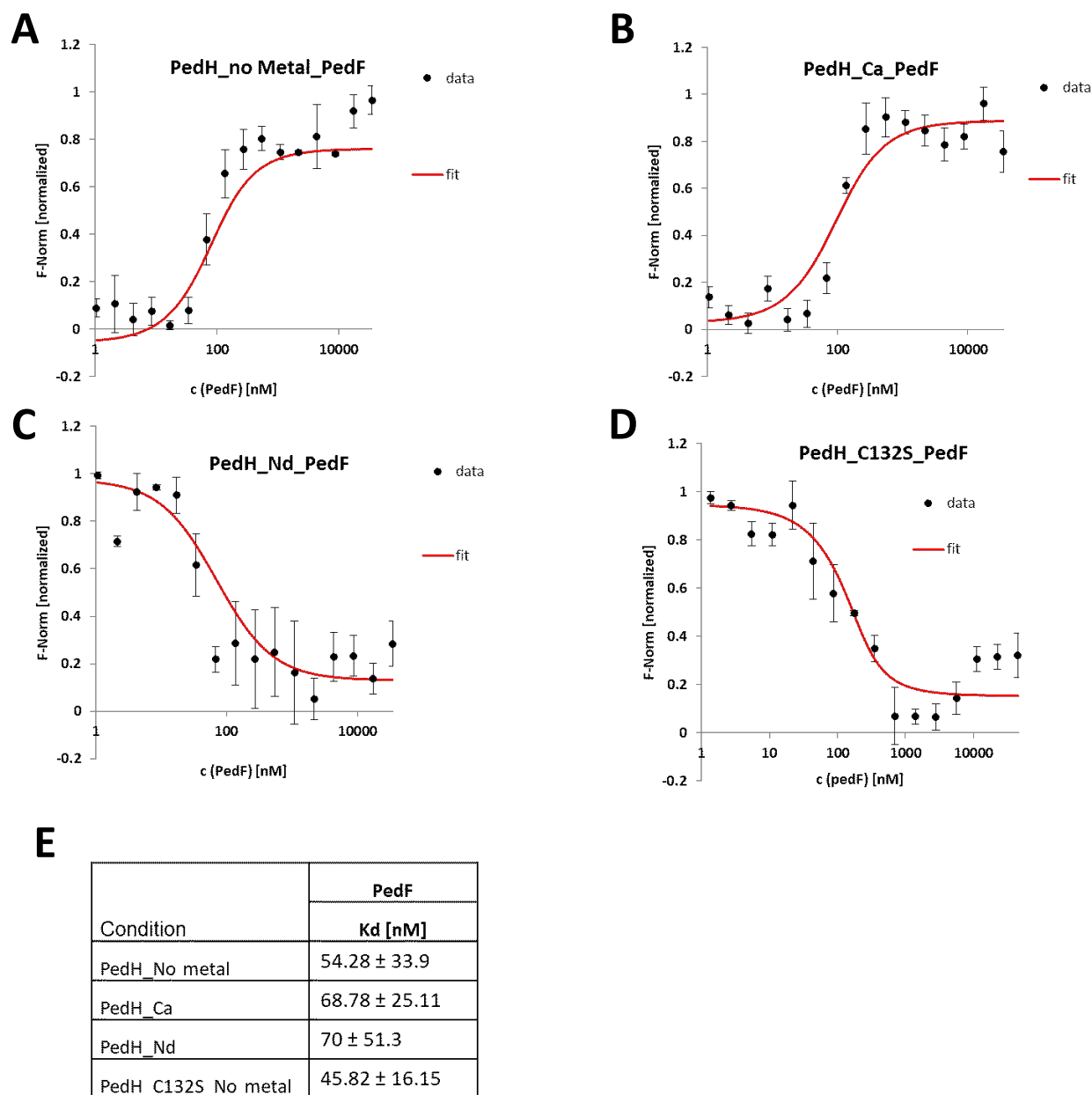


Figure 31. Binding affinity of PedH and PedH_C132S variant towards PedF in different metal conditions using MST. A, B, C represent Binding affinity of PedH towards PedF in presence of no metal, Ca, and Nd, respectively. D represents the binding affinity of PedH_C132S variant towards PedF in presence of no metal condition. E. The affinity in terms of dissociation constant (K_d) is calculated from the MST fitted curve that plots normalized fluorescence against concentration of PedF.

3.2.4. Metal dependency and activity of PedE and PedH can be switched.

To validate that mainly electrostatic reasons are causing the metal affinity and in turn the activity of the ADHs, it is hypothesized that switching the ligancy of the metal ion sphere would also change the affinity towards the metals that as a result would cause change in the activity level.

Based on the conserved residues defining Ca- and REEs- dependent ADHs, I have designed designated PedH variants with the intention to switch both their metal affinity and activity. The double variant PedH_G198D/D325S formed a PedH_{E-like} variant that showed a dramatic increase of neodymium (Nd) dissociation constant (K_d) by a factor of 100 confirming the assumption that these are the defining residues responsible for the Ln affinity of PedH. To determine if this switch can also be introduced into PedE, the corresponding variant PedE_{H-like} D198G/S334D was designed. For PedE_{H-like}, the switch in affinity was also confirmed by MST where K_d towards Nd has profoundly improved from 5 μ M to 76 nM. PedF dependent activity measurements confirmed that both ADHs variants were functional. PedE_{H-like} outperformed wildtype PedE by a factor of 2 in presence of neodymium compared to calcium reaching to almost half activity of WT-PedH. The comparison of individual specific activities revealed that PedE_{E-like} kept its Ca-dependent activity and almost lost its activity in presence of neodymium, confirming MST driven enzyme engineering (**Figure 32**).

Two single PedH variants have been designed in order to check the role played by each residue in PedH function. Due to the fact that D325PedH is in direct contact with the lanthanide ion sphere according to the solved structure, it was assumed that it would have more effect rather than G198PedH on both affinity and activity

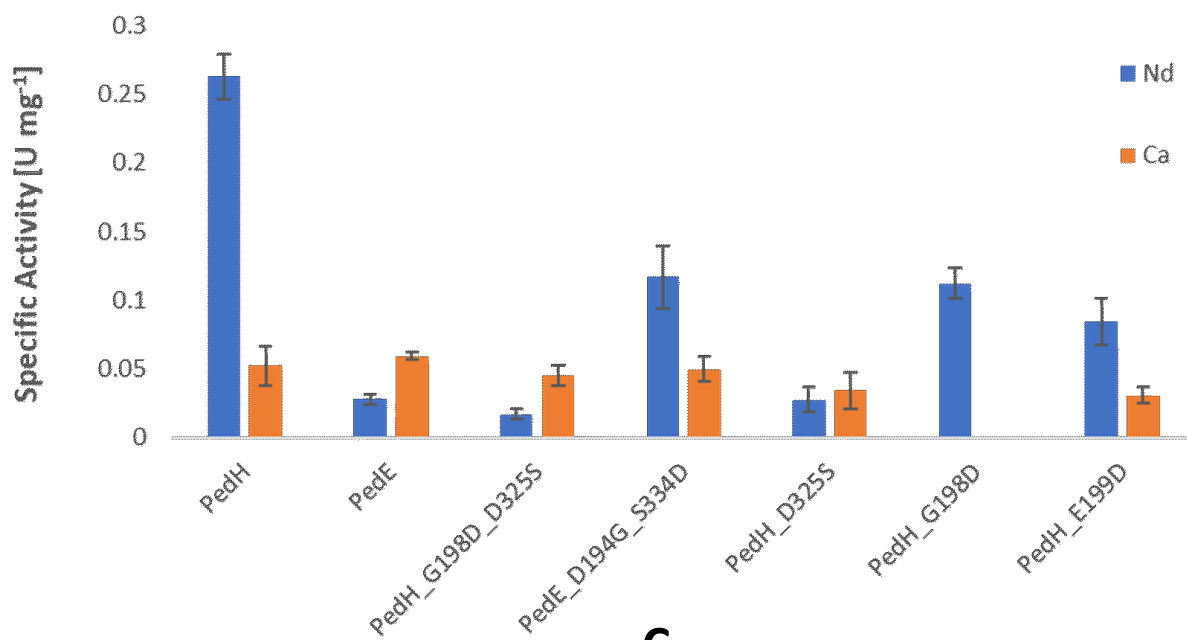
Results

in case of the lanthanide metal ion. The individual change of PedH_D325S clearly showed an increase of its K_d to 2.2 μM that was almost like the effect of the double mutant. This, in turn, significantly diminished its specific activity in presence of neodymium by almost 10 times to be in the same level as detected in case of WT PedH in presence of calcium.

On the other hand, PedH activity in case of calcium could be affected by conserved G198 as it could provide a flexibility for the “switch”-glutamate. Interestingly, PedH_G198D had lost both activity and affinity towards calcium. This reveals the significance of both residues for PedH functionality towards the available metal cofactor. However, it showed 6 times increase of Nd K_d to 200 nM and the activity was almost half of that observed with WT PedH.

To shed the light on the significance of coordinating the metal sphere in all directions, I further chose to exchange the “switch”-glutamate for an aspartate as it seemed that this one already exhibited some flexibility. This exchange reducing the distance towards the coordination sphere by one carbon atom left some partial negative charge allowing a partial coordination of the lanthanides. As the MST verified, the affinity of Ln was lowered by almost a factor of 10, resulting in a reduction of its specific activity to one-third of WT.

A



B

Enzyme	Specific Activity [U mg ⁻¹]	
	Nd	Ca
PedH	0.262 ± 0.016	0.052 ± 0.014
PedE	0.027 ± 0.004	0.059 ± 0.002
PedH_G198D_D325S	0.016 ± 0.003	0.045 ± 0.007
PedE_D194G_S334D	0.116 ± 0.022	0.049 ± 0.008
PedH_D325S	0.027 ± 0.009	0.034 ± 0.013
PedH_G198D	0.112 ± 0.011	ND
PedH_E199D	0.084 ± 0.016	0.030 ± 0.005

C

Enzyme	K _d [μM]	
	Nd	Ca
PedH	0.035 ± 0.002	67 ± 33.9
PedE	5 ± 2.6	24 ± 6.8
PedH_G198D_D325S	3.3 ± 0.6	31.1 ± 6.1
PedE_D194G_S335D	0.075 ± 0.002	39.6 ± 18.2
PedH_D325S	2.2 ± 0.3	43.7 ± 8.5
PedH_G198D	0.2 ± 0.01	ND
PedH_E199D	0.2 ± 0.04	44 ± 10.2

Figure 32. Metal Dependency and Activity of ADHs can be switched. A, B. Specific activity of PedH, PedE and their variants in presence of calcium (Ca) and neodymium (Nd). **C.** The affinity in terms of dissociation constant (K_d) is calculated from the MST fitted curves (Figure S4) that plot normalized fluorescence against concentration of metal of interest.

4. Discussion and Conclusion

4.1. REEs-dependent PedH has an extra coordinating residue “D325” completes the geometry required for Ln⁺³ coordination.

REEs-dependent enzymes represent an expanding family in biology [72]. It has been recently discovered that *P. putida* KT2440 widens the REEs-utilizing bacteria beyond the methylotrophs through expression of PedH (PP_2679), the lanthanide-dependent PQQ-ADH. Remarkably, in the same *ped* operon of *P. putida* KT2440 locates PedE (PP_2674), the calcium-dependent PQQ-ADH homolog [29]. Being able to produce 2 homologs makes this organism an interesting model for REEs biology investigation. Both PQQ-ADHs functionally perform the same scope of reaction [29] and their sequence alignment reveals 79.3 % sequence similarity with up to 51% sequence identity (**Figure 12A**). However, there is no clear evidence till now why PedH could be Ln-dependent in its alcohol dehydrogenase activity while its counterpart PedE uses calcium to perform the same function.

To gain a deeper insight into PQQ-ADHs in *P. putida* KT2440, their atomic structures were determined by X-ray crystallography in presence of the reported corresponding dependent metal. I was able to solve the structure of PedE in presence of calcium at 2.4 Å. In addition, PedH as the first discovered member of non-methylotrophic Ln-dependent ethanol dehydrogenases has been successfully determined in 4 different lanthanides states, in presence of La⁺³, Ce⁺³, Pr⁺³, and Nd⁺³.

Structurally, both PQQ-ADHs share a similar overall architecture, showing 8 W-shaped β -sheet motifs arranged circularly in a propeller-like style establishing a disk-shaped super barrel (**Figures 12B & 12C**), that described with previously

Discussion and conclusion

determined PQQ-ADHs structures [24], [45], [73], [74]. A similar active site region whatever the Ln^{+3} used in the co-crystallization process has been observed with PedH where the Ln^{+3} is coordinated through 9 atoms, 8 oxygen atoms of PQQ (2), E199 (2), N281 (1), D323 (1), D325 (2) and one nitrogen atom of PQQ (**Figure 16B**). In contrast, Ca^{+2} in case of PedE is coordinated through 7 atoms only where S334PedE replaces D325PedH, and it has not anymore role in Ca^{+2} coordination (**Figure 16A**). This observation, together with the fact that Ln^{+3} , particularly the light ones, have a higher charge to ionic radius ratio so that they prefer higher geometrical coordination numbers (8-12) compared to Ca^{+2} that prefer CNs of 6-8 and seldom reported with higher CNs [75], [76], highlighted the significance of this extra coordinating residue “D325” for Ln coordination as it completes the geometry required for the preferred coordination of Ln^{+3} .

Moreover, alignment of different Ln-dependent PQQ-ADHs [24], [62]–[64] reflects the conservation of this extra-aspartate residue while it is obviously replaced with alanine, serine, or threonine in case of Ca-dependent PQQ-ADHs [57], [65], [66] (**Figure 23D**). This has also been confirmed through the PedH_D325S variant that not only showed increase of its K_d value towards Nd^{+3} by approximately 100 times from 35 ± 2 nM of WT-PedH to 2.2 ± 0.3 μM that was close to that of WT-PedE, but it also showed 10 times less specific activity to be almost equal to that observed in case of WT PedE (**Figure 32**). Therefore, it could be concluded that PQQ-dependent ADHs can be distinguished into lanthanide- or calcium- dependent based on such defining amino acid that in position of D325_{PedH}/S334_{PedE} which could either actively participate in metal ion coordination increasing the CN by 2 in case of the Ln^{+3} or be apart from the metal ion coordination in case of Ca^{+2} . This explains the reason why PedH is optimized as a lanthanide-dependent PQQ-ADHs while this is not the case in case of PedE.

4.2. The REEs-dependent PedH has better catalytic efficiency than its Ca-dependent PedE

It is obvious that calcium, the fifth abundant element in the earth crust (**Figure 2**), is much more abundant almost by 1000 times than cerium, the most abundant REE [77]. It remained indefinable why to depend on an enzyme which is only active with metals that are found at lower abundance while the same function could be fulfilled with another enzyme that is active with the omnipresent calcium. In this regard, it was aimed to investigate the periplasmic oxidation process by both calcium- and lanthanide-dependent PQQ-ADHs in *P. putida* KT2440 in terms of affinity of enzymes towards the metals and the catalytic efficiency of each enzyme in presence of the corresponding metal.

MST data showed that PedH has a nanomolar dissociation constant (K_d) towards Ln^{+3} , approximately 1000 times less than that of PedE towards Ca^{+2} (**Figure 32**). This observation was in line with the findings of previous studies reported bacterial cells growth response towards nanomolar concentrations of lanthanides like *M. fumariolicum* SolV strain [24], *M. extorquens* AM1 [78] and *M. buryatense* 5GB1C [56]. As a result, it could be assumed that the abundance is not problematic as the concentration required for the lanthanides-dependent activity is relevant to the ecological abundance of these elements.

In the kinetics assay, ferricyanide was used as the final electron acceptor to detect the dehydrogenase activity of PQQ-ADHs (**Figure 19**). It is previously reported that type I PQQ-ADHs, of which PedE and PedH classified, are not able to directly reduce ferricyanide, however, in the presence of its natural c-type cytochrome, they exhibit at pH 7 an ethanol dependent ferricyanide reductase activity [59].

Discussion and conclusion

Due to its location on *ped* operon which is involved in alcohols dehydrogenation and the same operon where *pedE* (PP_2674) and *pedH* (PP_2679) localize, the only putative c-type cytochrome-encoding gene *pedF* (PP_2675) was challenged to be gene expressing the cognate electron acceptor for PedH and PedE (**Figure 7**). Firstly, MST data showed strong binding affinity of PedF towards PedH and PedE with K_d values of 70 ± 33.9 nM and 29.87 ± 23.5 nM, respectively (**Figure 18**). Further, initial activity measurements using 10 mM of ethanol as a substrate concentration and changing the PedF concentrations (0–50 μ M) was examined i) to prove the hypothesis that both PQQ-ADHs are able to use PedF to transfer the electrons towards ferricyanide so that they are sharing the same cytochrome ii) to guarantee saturating concentrations of PedF to be used in the next step for full kinetics assay of PQQ-ADHs towards ethanol as a substrate if the hypothesis is right. As a result, these measurements validated the proposed hypothesis and 20 μ M PedF were extrapolated to be used for the next comparative measurements (**Figure 20**).

Intriguingly, the efficiency in case of the Ln-dependent PedH was much more than that observed in case of its calcium-dependent counterpart PedE. The calculated catalytic efficiency of PedH (16.638 ± 4.57 $\text{mM}^{-1} \text{s}^{-1}$) was approximately 15 times more than that of PedE (1.268 ± 0.43 $\text{mM}^{-1} \text{s}^{-1}$) (**Figure 21**). This observation could be attributed to the stronger Lewis acidity properties of Ln^{+3} as a result of their higher capability to accept electrons in their 4f orbitals and the higher charge to ionic radius ratio compared to Ca^{+2} . Consequently, this is facilitating the hydride transfer from the substrate towards the cofactor PQQ through better coordinating the C-5 carbonyl oxygen of PQQ, thus stabilizing the electrophilic C-5 for the nucleophilic attack by the alcohol substrate. These findings are in accordance with a previous study reported that the Ln-dependent ExaF in *M. extorquens* AM1 had the highest catalytic efficiency with ethanol of any reported PQQ-dependent

Discussion and conclusion

ethanol dehydrogenas [78]. In addition, this efficiency can also be guessed from discovering high Lanthanides' concentrations in a steaming volcanic mudpot in Italy that enables *M. fumariolicum* to survive and grow in an environment full of volatiles [24] and the depletion of lighter lanthanides observed together with methanotrophic bacteria flourish in a submerged plume of water with high methane content during the Deepwater Horizon oil spill in 2010 [27].

Therefore, the affinity and kinetics studies could suggest that the ecological distribution of lanthanides, even with its known lower abundance compared to calcium, provide bacteria with very efficient system to get rid of the toxicity of volatile organic compounds and efficiently use them for energy production in case of their availability in the surrounding environment even with such low concentrations. It is also concurred that such functional redundancy of having 2 similar systems with different dependent metals improves the heftiness of complex systems to adapt with different environments.

4.3. Molecular switch defines the adaptability of PedH towards the calcium dependent activity.

Next, I wanted to investigate if these REEs-dependent enzymes are able to utilize calcium in case of lack of REEs in the surrounding environment. Intriguingly, PedH as well as PedE showed a close affinity towards Ca^{+2} in terms of micromolar dissociation constant (K_d), although it was not the case in case of Nd^{+3} (**Figures 22A-22C**). Curiously, I wanted to check what could happen for the specific activity of both enzymes when varying the metal ion cofactor. Surprisingly, the specific activity of PedH is significantly inhibited in case of changing the metal cofactor to calcium to be almost equal to that observed with PedE using the same metal cofactor. On the other hand, PedE in presence of neodymium shows half of its Ca-

Discussion and conclusion

dependent specific activity and 10 times less than that observed with Ln-dependent PedH activity (**Figures 22D & 22E**). This suggests that Ln⁺³ showing its stronger Lewis acid properties facilitating the dehydrogenase activity only when it is well coordinated through the polypeptide backbone.

As a result, it can be deduced that PedH is optimized towards performing the dehydrogenation in presence of the Ln⁺³ with a much more efficient way compared to the PedE for the reasons previously explained through PedH and PedE structures. In addition, both PQQ-ADHs are active in presence of Ca⁺² to the same extent that suggests that PedH could be also adapted for calcium-dependent activity. These observations are in complete accordance with previous studies that reported low ADH activity for culturally purified Ln-dependent ADH (XoxF1), that has proven to be completely loaded with Ca⁺² (> 97%), suggesting its function with Ca⁺² in absence of the Ln⁺³ [62]. In addition, previous proteomics studies showed high PedH (PP_2679) expression levels in *P. putida* KT2440 even in absence of lanthanides [39].

In order to investigate the reason(s) beyond the observed activity of PedH in presence of Ca⁺², the metal-free PedH was co-crystallized in presence of CaCl₂. Surprisingly, the active site of PedH showed a conformational change where the Ca⁺² coordination pattern has significantly changed from that observed in case of Ln⁺³. Only 7 atoms have been observed to participate in Ca⁺² coordination instead of the 9 atoms in case of Ln⁺³. Superimposition of the 2 states of PedH showed a switch of the upper coordinating glutamate (E199PedH) in the outside direction from the metal ion sphere. As a result, PedH showed a Ca⁺² coordination towards N281PedH, D323PedH, and D325PedH of the polypeptide and the O5, N6 and O7A atoms of the PQQ cofactor. Interestingly, this switch gives Ca⁺² its preferred

Discussion and conclusion

coordination number of 7 which is equal to that observed in case of Ca^{+2} in PedE (**Figure 23**).

To explain this finding theoretically, computational quantum chemical calculations have been performed. The energy differences (ΔE) for PedH between the “closed” and “open” conformations for $M = \text{Nd}^{+3}$, Ca^{+2} , Na^{+} and no metal ion in the center (for the structure parameters optimized for Ca^{+2}) amounted for -67.7, -5.2, 44.7, and 171.6 kJ/mol, respectively. As shown, the closed conformation is preferred with increasing the negative values of ΔE (**Table 5, Figure 24**). As a result, it could be implied that electrostatic reasons are responsible for the preference for the two different orientations of PedH depending on the oxidation state of the metal ion in the pocket. Therefore, it could be suggested that the lower charge to ionic radius ratio of Ca^{+2} compared to that of Ln^{+3} hinders calcium from acclimating high coordination numbers that frequently observed and preferred with lanthanides.

Previous studies using density functional theory (DFT) calculations and classical molecular dynamics simulations were employed to rationalize the enzymatic activities of Ln-dependent MDH [79], [80]. In accordance with the determined Ca-PedH structure in this study, the theoretical calculations of these studies reported that all Ln-coordinating residues are identical except the upper coordinating glutamate (E172 of Ln-dependent MDH) that switches from bidentate to unidentate in going from lighter (La, Eu) to heavier (Yb) lanthanide as a result of lanthanide contraction giving a theoretical evidence of the observed switchable glutamate flexibility according to the metal in the active site of PedH. In addition, the flexibility of the active site amino acids has been previously shown by a recent study comparing the 2 subunits of Ln-dependent ADH, one contains PQQ and the other does not [62].

Discussion and conclusion

Remarkably, alignment of several Known Ln-dependent ADHs including PedH revealed presence of a glycine residue directly before the switchable glutamate in contrast to PedE and other Ca-dependent ADHs that have bulkier group like aspartate (**Figure 23**). Interestingly, the affinity of PedH_G198D variant towards calcium was not detected under the measured range. In addition, its specific activity in presence of calcium was under the detectable level (**Figure 32**). It can be therefore speculated that the conserved G198PedH could also have a significant role providing flexibility for E199PedH for easily adapting the metal ion in the active site pocket.

It has been also observed that the E199PedH switch in the active site region is accompanied with switching of W561PedH on the direction of the conserved disulfide bridge (**Figure 23**). This was accompanied with the interesting observation that the thiol groups of C131 and C132 is linked when Ca^{+2} is coordinated in the active site and should not be linked in the closed state of PedH in case of one of the Ln^{+3} is coordinated. As a result, a clear difference has been observed in the electrostatic surface charge on the disulfide bridge surface side between the closed and open states in case of lanthanide and calcium state, respectively (**Figure 25**). HDX data revealed potential interaction between PedF and PedH on the disulfide bridge interface through a bunch of hydrophobic clusters and salt bridges (**Figure 30**). This is in accordance with several previous studies suggested an important role of the conserved disulfide bridge for the electron transfer from the PQQH_2 towards the heme of the PedF cytochrome [47], [81].

A hypothesis has been therefore raised that this molecular switch could in turn affect the interaction between PedH and PedF or the pathway of electron transfer from the reduced PQQ towards the Heme group of the PedF cytochrome. It was interesting to observe different biophysical pattern of interaction between PedF

Discussion and conclusion

and PedH by MST according to the metal used in the interaction, however the K_d values was almost non-changeable (50-70 nM) (**Figure 31**). This provides an assumption that the interaction still could happen but may be in a different way so that the pathway by which the electrons transfer from the PQQH₂ towards the Heme could be affected as a result of such change in PedH surface charge. Further support of this finding comes from the fact that a variant of the PedH dehydrogenase C132S which was proposed to mimic the state of the closed PedH in presence of Ln⁺³ where the disulfide bond has been reduced showed the same pattern of PedH binding towards PedF in absence of the metal cofactor in the interaction.

Summing up, structure analysis of PedE and PedH in *P. putida* KT2440 clearly showed that D325PedH plays a significant role in optimization of PedH towards the Ln-dependance. The functional analysis of both ADHs revealed that both enzymes use the cognate c-type cytochrome PedF in their periplasmic oxidation process where the Ln-dependent PedH has more catalytical efficiency compared to the Ca-dependent PedE. Furthermore, a molecular switch is in charge of an adaptive mechanism of PedH towards Ca-dependence.

5. Materials and Methods

5.1. Materials

5.1.1. Chemicals and consumables

Chemicals were purchased from Sigma Aldrich, Carl Roth, AppliChem or Acros in biochemical grades unless otherwise stated. Consumable plastic ware (reaction tubes, falcon tubes, pipette tips, syringes) was from Sarstedt and Braun.

5.1.2. Enzymes and cloning equipment

Q5 High-Fidelity DNA Polymerase, restriction enzymes and T4 DNA Ligase with their corresponding buffers were purchased from New England Biolabs (NEB). Deoxynucleoside triphosphates (dNTPs, 100 mM of each dNTP) were from Fermentas. Purification of DNA and preparation of plasmids from *E. coli* cells were carried out using the GeneJET Gel Extraction Kit and GeneJET Plasmid Miniprep Kit, respectively (both (Thermo Scientific) according to the manufacturer's manuals. Agarose gels for analysis of DNA were prepared in TBE-buffer according to the experimental requirements. GeneRuler 1kb (Thermo Scientific) served as size standard for agarose gel electrophoresis.

5.1.3. Bacterial strains and plasmids

5.1.3.1. Oligonucleotides

Oligonucleotides were purchased from Sigma Aldrich in the purity 'salt free'. All oligonucleotides used in this study are listed in Table S1.

5.1.3.2. Plasmids

For overproduction of hexa-histidine tagged PedE and PedH in *E. coli*, the vector pET24d(+), (Novagen) was employed. The plasmids, pET22b(+), (Novagen) and pEC86 (CCOS Accession: CCOS 891), were employed for overproduction of the periplasmic mature PedF. All plasmids used in this study are listed in Table S2. Plasmids were obtained using techniques described in chapter 5.2.1.

5.1.3.3. Strains

For plasmid amplification, chemically competent *E. coli* DH5 α cells (Thermo Scientific) were employed. Proteins were produced in chemically competent *E. coli* BL21 (DE3) cells (Thermo Scientific). *Pseudomonas putida* KT 2440 was kindly provided by Kai Thormann Lab., Department for Microbiology and Molecular Biology, Justus-Liebig-Universität Gießen.

5.1.4. Growth media and buffers

5.1.4.1. Growth media

Lysogeny broth (LB) medium was purchased as a premix from Roth and sterilized (121 °C, 20 min) before use. For preparation of LB medium for cultivation of *E. coli*, 25 g/l of LB premix were used.

5.1.4.2. Antibiotics

All antibiotics were purchased from Carl Roth and Sigma Aldrich. 1000x concentrated stock solutions were prepared by dissolving the antibiotic in the appropriate solvent and filtrated through a 0.2 μ M filter under aseptic conditions.

Materials and Methods

Antibiotic stock solutions were stored at -20 °C until use. Antibiotics were used in the following final concentrations:

Antibiotic	Final concentration (µg/ml)	Solvent
Ampicillin	100	ddH ₂ O
Kanamycin	50	ddH ₂ O
Chloramphenicol	35	Ethanol

5.1.4.3. Buffers for protein purification

Proteins were purified by a two-step protocol employing Ni-NTA affinity chromatography and size-exclusion chromatography (SEC).

Ni-NTA Lysis buffer	
HEPES	20 mM
KCl	20 mM
NaCl	500 mM
Imidazole	40 mM

pH 8.0 with NaOH

Ni-NTA Elution buffer	
HEPES	20 mM
KCl	20 mM
NaCl	500 mM
Imidazole	500 mM

pH 8.0 with NaOH

SEC buffer	
HEPES	20 mM
KCl	20 mM
NaCl	500 mM

pH 7.5 with NaOH

5.1.4.4. Buffers for HDX

D₂O-containing SEC buffer for deuteration of PedH and PedF during HDX experiments (see chapter 5.2.10) was prepared by dissolving the solid components in deuterium oxide 99.9% (Sigma Aldrich). The pD value of the solution was adjusted to 7.5 using 10 M NaOD obtained by dissolving NaOH in deuterium oxide 99.9%. During determination of the pD value of deuterated SEC buffer with a pH electrode calibrated for H₂O, the differing dissociation constants of H₂O and D₂O were taken into account. Peptides were separated during HDX employing HDX buffer A and B. The quench buffer for stopping the HDX reaction and the wash solution for cleaning the columns used in the HDX setup were prepared as follows:

HDX quench buffer	
KH ₂ PO ₄ /H ₃ PO ₄	400 mM

pH 2.2 with H₃PO₄

HDX column wash solution	
Acetonitrile	4% (v/v)
Guanidine-HCl	500 mM

HDX buffer A	
ddH ₂ O	
Formic acid	0.1% (v/v)

HDX buffer B	
Acetonitrile	
Formic acid	0.1% (v/v)

5.1.4.5. Buffers for agarose gel electrophoresis

Agarose gels were prepared by dissolving agarose in Tris/boric acid/EDTA (TBE) buffer. For visualization of nucleic acids, ethidium bromide was directly

Materials and Methods

added to the gels. The following buffers were used for agarose gel electrophoresis:

TBE buffer	
Tris	90 mM
Boric acid	90 mM
EDTA	2 mM

pH 8.3 with NaOH

5.1.4.6. Buffers for sodium dodecyl sulfate polyacrylamide gel electrophoresis (SDS-PAGE)

Gels for SDS-PAGE were prepared using a Mini-PROTEAN 3 Multi-Casting Chamber (Biorad) and stored at 4 °C until use. The stacking and separation gels had the following composition:

Component	Stacking gel	Separation gel
Acrylamide/Bisacrylamide (37.5/1)	4.5 % (w/v)	15 % (w/v)
Tris	125 mM	375 mM
SDS	0.1 % (w/v)	0.1 % (w/v)
APS	0.1 % (w/v)	0.1 % (w/v)
TEMED	0.1 % (w/v)	0.1 % (w/v)
Final pH adjusted with HCl	6.8	8.8

Materials and Methods

For loading and running of SDS-PAGE gels and visualization of proteins, the following buffers were employed:

SDS running buffer	
Tris	25 mM
Glycine	192 mM
SDS	0.1 % (w/v)

5x SDS loading dye	
Tris-HCl pH 6.8	300 mM
SDS	10 % (w/v)
β -mercaptoethanol	25 % (v/v)
Glycerin	25% (v/v)
Bromophenol blue	0.05% (w/v)

SDS staining solution	
Comassie R250	0.36% (w/v)
Ethanol 99%	45.5% (v/v)
Acetic acid 99%	9% (v/v)

SDS destaining solution	
Ethanol 99%	30% (v/v)
Acetic acid 99%	10% (v/v)

5.1.5. Protein biochemistry

Prepacked columns (HisTrap FF, 1 ml and 5 ml) for purification of hexa-histidine tagged proteins were purchased from GE Healthcare. Purified proteins were concentrated using Amicon Ultra-15 centrifugal filter units (Merck Millipore) with molecular weight cut-offs of 10 and 3 Kda. PageRuler unstained protein ladder (Thermo Scientific) and Pierce unstained protein MW marker (Thermo Scientific) served as standards for molecular weight estimation on SDS-PAGE gels.

Materials and Methods

5.1.6. Laboratory equipment

Equipment	Supplier
FPLC systems	
ÄKTApure	GE Healthcare
ÄKTApurifier	GE Healthcare
ÄKTAprime	GE Healthcare
Columns for protein purification	
HiLoad 26/600 Superdex S200 pg	GE Healthcare
HiLoad 26/600 Superdex S75 pg	GE Healthcare
HisTrap FF, 1 ml	GE Healthcare
HisTrap FF, 5 ml	GE Healthcare
Incubators	
Ecotron	Infors HT
Incucell	MMM Einrichtungen Medcenter
WiseCube	Wisd Laboratory Instruments
Microscopes	
SZM-2	Optika Microscopes
AX70 Research System Microscope	Olympus
UPlanSApo 100x/1.40 objective	Olympus
Photometrics CoolSnap ES2 CCD camera	Visitron Systems
Centrifuges	
Sorvall LYNX 6000	Thermo Scientific
A27-8 x 50 Fixed Angle Rotor	Thermo Scientific
Fiberlite F9-6 x 1000 LEX Fixed Angle Rotor	Thermo Scientific

Materials and Methods

Heraeus Megafure 40R	Thermo Scientific
Heraeus Fresco 21 Centrifuge	Thermo Scientific
Heraeus Pico 21 Centrifuge	Thermo Scientific
Weights	
Präzisionswaage PCB, d = 0.1g	Kern
Weight S-203, d = 0.001 g	Denver Instrument
Weight SI-203, d = 0.1 mg	Denver Instrument
HDX equipment	
ACQUITY UPLC M-Class system with HDX Technology	Waters
Two-arm robotic autosampler	LEAP Technologies
Enzymate BEH Pepsin column 2.1 x 30 mm	Waters
ACQUITY UPLC BEH C18 1.7 µm 1.0 x 100 mm column	Waters
AQUITY UPLC BEH C18 1.7 µm 2.1 x 5 mm vanguard	Waters
SYNAPT G2-Si	Waters
Miscellaneous	
SDS-PAGE equipment	Biorad
Agarose gel equipment	Cleaver Scientific
Ultrospec 10 Cell Density Meter	Amersham
T100™ Thermal cycler	Biorad
M-110L Microfluidizer	Microfluidics
Gel iX20 Imager	Intas
Crystal Gryphon LCP	ARI - Art Robbins Instruments
Peristaltic pump	Gilson
NanoDrop Lite	Thermo Scientific

Materials and Methods

HI-2211 Bench Top pH & mV meter	Hanna Instruments
Vortex	IKA England Ltd.
Autoclave	Ibs Tecnomara
Microwave D450W Inverter	Panasonic
Shaker Dos-10L	neoLab

5.2. Methods

5.2.1. Molecular cloning.

The gene encoding *PedE* (PP_2674), *PedF* (PP_2675), *PedH* (PP_2679) without the nucleotides corresponding for the signal peptide (*PedE*³⁴⁻⁶³⁴, *PedF*²⁶⁻¹⁵³ and *PedH*²⁸⁻⁵⁹⁵) were amplified from genomic DNA of *Pseudomonas putida* KT2440 by polymerase chain reaction (PCR) using Q5[®] and Phusion[®] High-Fidelity DNA Polymerase (NEB) according to the manufacturer's protocol. Briefly, 100 μ M dNTP's (NEB), 200 μ M of each oligonucleotide primer and 0.01 U/ μ l polymerase was used to set up a PCR reaction. An estimation of the optimal annealing temperature for each oligonucleotide was calculated by the webpage OligoCalc (<http://biotools.nubic.northwestern.edu/OligoCalc.html>). The program used was personally adjusted for each reaction according to the oligonucleotides and templates.

DNA was separated and visualized by agarose gel electrophoresis employing TBE as buffer. Depending on the DNA fragment size, gels were prepared with an agarose concentration ranging from 0.8 % to 2 % (w/v). The agarose was dissolved in running TBE buffer by microwave heating and poured into gel casts. 5 μ l of a 0.025 % ethidium bromide solution (Roth) was added to 100 ml of gel solution. Gel

Materials and Methods

loading dye (6X, NEB) was added in appropriate amounts to the samples prior to loading. A voltage of 120 V was applied for 20-30 minutes, and DNA visualized with a Gel iX20 Imager (intas). Purification of DNA was carried out using the GeneJET Gel Extraction Kit (Thermo scientific) according to the manufacturer's manuals.

Golden Gate Assembly [82], [83] has been applied for the initial cloning yielding N-terminus histidine-tagged pET24d-PedE and pET22b-PedF using a forward primer that contained a NcoI restriction site and the coding sequence for a hexa-histidine tag and a reverse primer which contained a XhoI restriction site (**Table S1**). Both primers have the BsaI restriction site coding sequence. The hexa-histidine tag introduced in the reverse primer in case of PedH yielding C-terminus histidine-tagged pET24d-PedH. The coding sequences for the hexa-histidine tag were in-frame with the sequence of the cloned genes. All Golden Gate reactions were performed in a total volume of 15 μ l. The final reaction volume contained 1-fold concentrated T4 ligase buffer (Promega, Madison, US). Prepared reaction mixtures (ligase buffer, acceptor plasmid, insert(s)) were adjusted to 13.5 μ l with ddH₂O. First, a volume of 0.5 μ l of BsaI-HF[®]v2 (10 units; New England Biolabs, Ipswich, US) and then 1 μ l (1-3 units) of T4 ligase (Promega, Madison, US) was added. Golden Gate reactions were carried out by default under following conditions: a) enzymatic restriction 37 °C (2 min); b) Ligation 16 °C (5 min) [10 passes each] and c) enzyme inactivation: 80 °C (20 min).

Variants have been cloned using Golden Gate Mutagenesis. The mutated fragments are amplified from the corresponding plasmid using a forward and reverse primers have the desired mutation and BsaI restriction site.

Transformation of chemically competent *E. coli DH5 α* strains was performed with 50 – 200 ng of plasmid and 100 μ l of cells. The cells were incubated with plasmid

Materials and Methods

DNA for 10 minutes on ice and then transferred to a neoBlock 1 (Neolab) for 45 seconds of incubation at 42 °C. Afterwards, 300 µl of SOC media was added, the cells transferred to 37 °C and incubated for one hour at 200 rpm. The whole aliquot was transferred to selective media and incubated at 37 °C overnight.

To extract plasmid DNA, 5 ml cultures of *E. coli* were inoculated from one colony and incubated overnight at 37 °C and 200 rpm. The cells were harvested by centrifugation at 4000 rpm for 5 minutes in a Heraeus Meagfuge 40R (Thermo Scientific) and further processed according to the manufacturer's manual supplied with the GeneJET Plasmid Miniprep Kit (Thermo Scientific). The plasmid DNA was finally eluted in 50 µl deionized water. All cloned plasmids have been verified by sequencing diagnosis through Microsynth seqlab (Germany) and stored at -20 C for further use.

5.2.2. Purification of PedE and PedH.

PedE, PedH and their variants thereof were purified by the same procedure with the buffers stated in chapter 5.1.4.3. *E. coli* BL21(DE3) cells carrying the expression plasmid were grown in LB medium supplemented with 50 µg/ml kanamycine and 12.5 g/l D(+)-lactose-monohydrate for 16 h at 30 °C and shaking at 150 rpm (WiseCube). Cells were harvested (3500 x g, 20 min, 4 °C), resuspended in lysis buffer and lysed using a pressure of 18,000 psi through the M-110L Microfluidizer (Microfluidics). After centrifugation (47850 x g, 20 min, 4 °C), the clarified supernatant was loaded on a 5-ml HisTrap column equilibrated with 10 column volumes (CV) of lysis buffer for NiNTA affinity chromatography. After washing with 15 CV lysis buffer, the protein was eluted with 3 CV elution buffer. The protein was concentrated to volume of 2.5 ml using an Amicon Ultracel-10K (Millipore) and applied to size-exclusion chromatography (SEC) (HiLoad 26/600

Materials and Methods

Superdex S200 pg) equilibrated in SEC buffer. Fractions containing the pure protein were pooled and concentrated according to the experimental requirements. Protein concentration was determined spectrophotometrically (NanoDrop Lite).

5.2.3. Protein production and purification of PedF.

PedF was expressed in the presence of pEC86, a plasmid encoding cytochrome c maturation factors [60]. Chemically competent *E. coli* BL21(DE3) cells were co-transformed with pET22b-PedF (AmpR) and pEC86 (CmR) and plated on lysogeny broth (LB)-agar plates containing ampicillin (Amp; 50 $\mu\text{g mL}^{-1}$) and chloramphenicol (Cm; 35 $\mu\text{g mL}^{-1}$; antibiotic concentrations in all media), and grown at 30°C. A single colony was used to inoculate LB-Amp/Cm (5 mL), which was grown overnight at 30°C with 200 rpm shaking. This culture was used to inoculate a 100 mL culture at 100 \times dilution, which was grown under the same conditions. This culture in turn was used to inoculate 8 \times 1 L LB-Amp/Cm at 100 \times dilution, which was grown under the same conditions to OD₆₀₀=0.5-0.8, at which point isopropyl β -d-1-thiogalactopyranoside (IPTG; 1 μM) was added, and protein expression was induced overnight (15 h). Cells were harvested by centrifugation for 15 min at 8000x g and 4°C to yield 6-8 g cell paste per L culture. The cell pellets were used immediately to harvest the periplasmic fraction containing PedF.

The cell paste was resuspended by pipetting and stirring at 40 mL g⁻¹ in previously described lysis buffer with 20% (w/v) sucrose and ethylenediaminetetraacetic acid (EDTA; 1 mM) at room temperature (20°C). The suspension was stirred at 150 rpm at room temperature for 10 min and then centrifuged for 20 min at 8000 x g and 4°C. The supernatant was decanted, and the pellet was resuspended in ice-cold MgSO₄ (5 mM), at 20 mL g⁻¹ (original wet weight). The suspension was stirred for 10 min at 4°C and then centrifuged for 10 min at 8000x g and 4°C. The

Materials and Methods

supernatant containing the periplasmic extract was decanted and applied onto 1 ml HisTrap FF columns (GE Healthcare) equilibrated by 15 CV of the same buffer for NiNTA affinity chromatography[84]. After a wash step with 15 CV of lysis buffer, proteins were eluted with three CV of elution buffer. Protein eluted fraction was pooled and concentrated in Amicon Ultra-10K centrifugal filters to a volume of 2.5 ml and further purified by size-exclusion chromatography (SEC). PedF was purified using a HiLoad 26/600 Superdex 200 column (GE Healthcare) equilibrated in SEC buffer. Fractions containing PedF were pooled and concentrated for further experiments.

5.2.4. SDS-PAGE

Prior to SDS-PAGE analysis, protein samples were mixed with 5x SDS loading dye in a volume ratio of 5:1. Electrophoresis was performed in a Mini-PROTEAN Tetra cell (Biorad) at 260 V for 35 min. The gels were stained for approximately 30 min using SDS staining solution. After removal of the staining solution, the gels were destained using SDS destaining solution until the protein bands were clearly distinguishable from the background.

5.2.5. Heme staining of PedF SDS-PAGE

The PedF samples are applied on a second SDS-PAGE gel that was directly soaked in water for 20 min after electrophoresis in a Mini-PROTEAN Tetra cell (Biorad) at 260 V for 35 min, and then incubated in a solution containing 0.2% (w/v) 3,3'-diaminobenzidine tetra-hydrochloride (DAB), 25% methanol, and 0.25 M sodium citrate (pH 4.7) for 1 h. 2% hydrogen peroxide was then added for color development [85].

5.2.6. Structural biology

5.2.6.1. Crystallization

Crystallization screens were carried out at room temperature by the sitting-drop method in SWISSCI MRC 2-well or SWISSCI MRC 3-well plates (Jena Bioscience) using the JCSG Core Suites (Qiagen). The reservoir volume was 50 μl and the drop volume typically 1 μl containing a 1:1 mixture of protein and crystallization solution. Crystals of PedH and PedE were obtained from a 250 μM concentration with ten times equimolar concentration of PQQ and metal of interest within 24-48h as detailed in table 1.

Prior data collection, crystals were flash-frozen in liquid nitrogen employing a cryo-solution that consisted of mother-liquor supplemented with 30 % (v/v) glycerol. Crystals were looped with Adjustable Mounted CryoLoops™ of different diameters sourced from Hampton Research (CrystalCap Spine HT, CrystalCap SPINE Vial and CrystalWand Magnetic). Data were collected under cryogenic conditions at the beamline ID30A-1 (MASSIF-1) operated by European Synchrotron Radiation Facility (ESRF, Grenoble, France) [86], at the beamlines (P13/P14) operated by EMBL Hamburg at the PETRA III storage ring (DESY, Hamburg, Germany) [87] or at the MX beamline BL14.1 operated by Helmholtz-Zentrum (BESSY, Berlin, Germany) [88] under laminar nitrogen flow at 100 K (Oxford Cryosystems 700 Series) with a DECTRIS PILATUS 6M detector.

5.2.6.2. Data processing and refinement

Diffraction Data were integrated and scaled with XDS and merged with XSCALE [89]. Structures were determined by molecular replacement with PHASER [90], manually built in COOT [91], and refined with PHENIX [92]. The structure of the

Materials and Methods

ADH-PQQ-Metal complex was determined by molecular replacement using the crystal structures of ExaA of *Pseudomonas aeruginosa* (PDB-ID: 1FLG) as search models [57]. Figures were prepared with PYMOL (www.pymol.org) [93].

5.2.7. The ferricyanide reductase Kinetics assay.

The ferricyanide reductase assay protocol was adapted from Reichmann and Gorisch [61] which was initially developed to assay quinoprotein ethanol dehydrogenase with cytochrome C₅₅₀ as electron acceptor. To detect the saturating concentration of PedF as a cytochrome, the final assay (200 μ L final volume) contained K₃[Fe(CN)₆] (1 mM), 50 μ M NdCl₃ or 50mM CaCl₂, 100 μ M PQQ, ethanol (10 mM), ADH (100 nM), and PedF at a range of concentrations (0–50 μ M) in 20 mM HEPES pH 7.5, 20 mM KCl and 500 mM NaCl. All assay components except for ethanol were added to the plate (Greiner Bio-One 96-well half area) and equilibrated in the plate reader at 30 °C for 20 min, during which time A₄₂₀ nm did not change significantly. The assay was then initiated by addition of ethanol (20 μ L) and the absorbance decrease at 420 nm was monitored every 30 s for 60 min.

For Kinetics assay of ADHs towards ethanol as a substrate, the same setup has performed except that 20 μ M of PedF as the cytochrome concentration and variable concentrations of ethanol (0-20 mM) have been used. The molar extinction coefficient of K₃[Fe(CN)₆] was experimentally determined to be 1.04 mM⁻¹cm⁻¹. The rate of reduction was calculated from the average slope over the first 15 min of the assay, from which the specific activity of ADHs was calculated. All assays were performed in three replicates, and data are presented as the mean value with error bars representing the corresponding standard deviation. All

analysis of kinetic data was carried out using GraphPad Prism version 6.04 for Windows (GraphPad Software, San Diego, California, USA).

5.2.8. Quantum chemical computational analysis.

Structures were optimized with TURBOMOLE [94] at level BP86 [95]/def-SV(P) [96], for the optimized structures single-point energies were obtained at level PBE0 [97] / dhf-TZVP [98], together with Dirac-Fock effective core potentials (ECPs) for the Cd [99], Hg [99], Bi [100]. For Nd and Th, a Wood-Boring ECP with 49 [101] (78 [102]) core electrons was used together with the corresponding triple zeta valence basis sets [101], [102]. For the compensation of negative charges the conductor-like screening model (COSMO) [68], [103] was used with default settings throughout.

5.2.9. Measurements of affinity in terms of dissociation constants (K_d) by microscale thermophoresis (MST).

MST experiments were performed in a buffer containing 20 mM HEPES pH 7.5, 20 mM KCl and 500 mM NaCl using a Monolith NT.115 with red LED power set to 50% and infrared laser power to 75 % [104], [105]. PedH, PedE and the variants (50 μ M) were each labeled using Monolith NT™ Protein Labeling Kit RED-NHS (Amine Reactive) according to the supplier's instructions (dye NT 647, Nano Temper technologies). The excess unreacted "free" dye was then eliminated through the supplied buffer exchange column and the concentration of labelled protein had been detected using Bradford protein quantification assay. Subsequently, 200 nM of each protein with equimolar of PQQ was titrated with increasing amounts of the metal of interest starting from 0-50 μ M, 0-5000 μ M for Ln and Ca, respectively or 0-50 μ M of PedF in case of detecting the K_d value of

Materials and Methods

PedH towards PedF. At least three independent MST experiments were recorded at 680 nm and processed by NanoTemper Analysis 1.2.009 and Origin8G. Negative controls, including titrating metals of interest to the buffer and buffer containing PQQ without the addition of an enzyme have been applied and did not show any binding behavior.

5.2.10. Hydrogen-Deuterium Exchange Mass Spectrometry (HDX-MS)

Samples for HDX-MS contained 50 μ M PedF or 50 μ M PedH and 100 μ M PQQ or a mixture of PedF, PedH (both 50 μ M) and 100 μ M PQQ in SEC buffer (20 mM HEPES-Na pH 7.5, 20 mM KCl, 500 mM NaCl). Preparation of HDX reactions was aided by a two-arm robotic autosampler (LEAP technologies). 7.5 μ l of sample were mixed with 67.5 μ l of D₂O-containing SEC buffer to start the exchange reaction and incubated for 10, 100, 1,000 or 10,000 seconds at 25 °C. Subsequently, 55 μ l of this reaction were withdrawn and mixed with an equal volume of quench buffer (400 mM KH₂PO₄/H₃PO₄, 2 M guanidine-HCl, pH 2.2) kept at 1 °C. 95 μ l of the resulting mixture were injected into an ACQUITY UPLC M-Class System with HDX Technology (Waters) [106]. Undeuterated samples were prepared similarly by 10-fold dilution into H₂O-containing SEC buffer.

The injected sample was flushed out of the loop (50 μ l) with H₂O + 0.1 % (v/v) formic acid (100 μ l/min) and guided to a column (2 mm x 2 cm) filled with a mixture of immobilized porcine pepsin, protease type XIII from *Aspergillus saitoi* and protease type XVIII from *Rhizopus* sp. in 1:1:1 ratio and kept at 12 °C. The resulting peptides were collected on a trap column (2 mm x 2 cm) filled with POROS 20 R2 material (Thermo Scientific) kept at 0.5 °C for a duration of 3 min. Afterwards, the trap column was placed in line with an ACQUITY UPLC BEH C18 1.7 μ m 1.0 x 100 mm column (Waters), and the peptides eluted at 0.5 °C using a gradient of H₂O + 0.1 % (v/v) formic acid (buffer A) and acetonitrile + 0.1

Materials and Methods

% (v/v) formic acid (buffer B) at a flow rate of 30 μ l/min as follows: 0-7 min/95-65 % A, 7-8 min/65-15 % A, 8-10 min/15 % A, 10-11 min/5 % A, 11-16 min/95 % A.

The elution was guided to a G2-Si HDMS mass spectrometer with ion mobility separation (Waters), peptides ionized with an electrospray ionization source (250 °C capillary temperature, spray voltage 3.0 kV) and mass spectra acquired in positive ion mode over a range of 50 to 2000 m/z in HDMS^E or HDMS mode for undeuterated and deuterated samples, respectively [107], [108]. Lock-mass correction was conducted with [Glu1]-Fibrinopeptide B standard (Waters). During chromatographic separation of the peptide mixtures, the protease column was washed three times with 80 μ l of 4 % (v/v) acetonitrile and 0.5 M guanidine hydrochloride and blank injections performed between each sample. All measurements were carried out in triplicate.

Peptide identification and analysis of deuterium incorporation were carried out with ProteinLynx Global SERVER (PLGS, Waters) and DynamX 3.0 softwares (Waters) as described previously [109].

6. References

- [1] J. N. Goswami, "Nucleosynthesis BT - Encyclopedia of Geochemistry: A Comprehensive Reference Source on the Chemistry of the Earth," W. M. White, Ed. Cham: Springer International Publishing, 2018, pp. 1014–1019.
- [2] A. Frebel and T. C. Beers, "The formation of the heaviest elements," vol. 30, no. 2018, 2019, doi: 10.1063/PT.3.3815.
- [3] H. Sigel, "Biological action of metal ions," *Met. Ions Biol. Syst.*, 1976.
- [4] C. Sissi and M. Palumbo, "Effects of magnesium and related divalent metal ions in topoisomerase structure and function," *Nucleic Acids Res.*, vol. 37, no. 3, pp. 702–711, Feb. 2009, doi: 10.1093/nar/gkp024.
- [5] F. Wall, "Rare Earth Elements," D. Alderton and S. A. B. T.-E. of G. (Second E. Elias, Eds. Oxford: Academic Press, 2021, pp. 680–693.
- [6] K. M. Goodenough, F. Wall, and D. Merriman, "The Rare Earth Elements: Demand, Global Resources, and Challenges for Resourcing Future Generations," *Nat. Resour. Res.*, vol. 27, no. 2, pp. 201–216, 2018, doi: 10.1007/s11053-017-9336-5.
- [7] R. L. Rudnick, S. Gao, H. D. Holland, and K. K. Turekian, "Composition of the continental crust," *The crust*, vol. 3, pp. 1–64, 2003.
- [8] D. Qi, "Chapter 1 - Extraction of Rare Earths From RE Concentrates," D. B. T.-H. of R. E. Qi, Ed. Elsevier, 2018, pp. 1–185.
- [9] X. J. Yang, A. Lin, X.-L. Li, Y. Wu, W. Zhou, and Z. Chen, "China's ion-adsorption rare earth resources, mining consequences and preservation," *Environ. Dev.*, vol. 8, pp. 131–136, 2013, doi: <https://doi.org/10.1016/j.envdev.2013.03.006>.
- [10] M. M. Bomgardner, "The struggle to mine rare earths," *Chem. Eng. NEWS*, vol. 93, no. 30, pp. 36–39, 2015.
- [11] C. H. Evans, *Biochemistry of the Lanthanides*, vol. 8. Springer Science & Business Media, 2013.
- [12] M. R. MacDonald, J. E. Bates, J. W. Ziller, F. Furche, and W. J. Evans, "Completing the Series of +2 Ions for the Lanthanide Elements: Synthesis of Molecular Complexes of Pr²⁺, Gd²⁺, Tb²⁺, and Lu²⁺," *J. Am. Chem. Soc.*, vol. 135, no. 26, pp. 9857–9868, Jul. 2013, doi: 10.1021/ja403753j.
- [13] "Aufbau Principle," *Encyclopedia of Inorganic and Bioinorganic Chemistry*. Dec. 15, 2011, doi: <https://doi.org/10.1002/9781119951438.eibd0064>.

References

- [14] D. P. Wong, "Theoretical justification of Madelung's rule," *J. Chem. Educ.*, vol. 56, no. 11, p. 714, Nov. 1979, doi: 10.1021/ed056p714.
- [15] R. D. Shannon, "Revised effective ionic radii and systematic studies of interatomic distances in halides and chalcogenides," *Acta Crystallogr. Sect. A Cryst. physics, diffraction, Theor. Gen. Crystallogr.*, vol. 32, no. 5, pp. 751–767, 1976.
- [16] M. Seitz, A. G. Oliver, and K. N. Raymond, "The lanthanide contraction revisited.," *J. Am. Chem. Soc.*, vol. 129, no. 36, pp. 11153–11160, Sep. 2007, doi: 10.1021/ja072750f.
- [17] D. D. Perrin, *Ionisation constants of inorganic acids and bases in aqueous solution*, no. 29. Elsevier, 2016.
- [18] G. Tyler, "Rare earth elements in soil and plant systems - A review," *Plant Soil*, vol. 267, no. 1, pp. 191–206, 2004, doi: 10.1007/s11104-005-4888-2.
- [19] Q. Shen, "Application of rare earth elements on animal production," *Feed Ind.*, vol. 12, pp. 21–22, 1991.
- [20] G. B. Haxel, J. B. Hedrick, G. J. Orris, P. H. Stauffer, and J. W. Hendley II, "Rare earth elements: critical resources for high technology," 2002. doi: 10.3133/fs08702.
- [21] Y. Hibi, K. Asai, H. Arafuka, M. Hamajima, T. Iwama, and K. Kawai, "Molecular structure of La³⁺-induced methanol dehydrogenase-like protein in *Methylobacterium radiotolerans*," *J. Biosci. Bioeng.*, vol. 111, no. 5, pp. 547–549, 2011, doi: <https://doi.org/10.1016/j.jbiosc.2010.12.017>.
- [22] N. A. Fitriyanto, M. Fushimi, M. Matsunaga, A. Pertiwinigrum, T. Iwama, and K. Kawai, "Molecular structure and gene analysis of Ce³⁺-induced methanol dehydrogenase of *Bradyrhizobium* sp. MAFF211645," *J. Biosci. Bioeng.*, vol. 111, no. 6, pp. 613–617, 2011, doi: <https://doi.org/10.1016/j.jbiosc.2011.01.015>.
- [23] T. Nakagawa *et al.*, "A Catalytic Role of XoxF1 as La³⁺-Dependent Methanol Dehydrogenase in *Methylobacterium extorquens* Strain AM1," *PLoS One*, vol. 7, no. 11, p. e50480, Nov. 2012, [Online]. Available: <https://doi.org/10.1371/journal.pone.0050480>.
- [24] A. Pol *et al.*, "Rare earth metals are essential for methanotrophic life in volcanic mudpots.," *Environ. Microbiol.*, vol. 16, no. 1, pp. 255–264, Jan. 2014, doi: 10.1111/1462-2920.12249.
- [25] A. M. Panichev, "Rare Earth Elements: Review of Medical and Biological Properties and Their Abundance in the Rock Materials and Mineralized Spring Waters in the Context of Animal and Human Geophagia Reasons

References

- Evaluation,” *Achiev. Life Sci.*, vol. 9, no. 2, pp. 95–103, 2015, doi: <https://doi.org/10.1016/j.als.2015.12.001>.
- [26] H. Herrmann, J. Nolde, S. Berger, and S. Heise, “Aquatic ecotoxicity of lanthanum – A review and an attempt to derive water and sediment quality criteria,” *Ecotoxicol. Environ. Saf.*, vol. 124, pp. 213–238, 2016, doi: <https://doi.org/10.1016/j.ecoenv.2015.09.033>.
- [27] A. M. Shiller, E. W. Chan, D. J. Joung, M. C. Redmond, and J. D. Kessler, “Light rare earth element depletion during Deepwater Horizon blowout methanotrophy,” *Sci. Rep.*, vol. 7, no. 1, p. 10389, Sep. 2017, doi: [10.1038/s41598-017-11060-z](https://doi.org/10.1038/s41598-017-11060-z).
- [28] G. De Simone, F. Polticelli, S. Aime, and P. Ascenzi, “Lanthanides-based catalysis in eukaryotes.,” *IUBMB Life*, vol. 70, no. 11, pp. 1067–1075, Nov. 2018, doi: [10.1002/iub.1933](https://doi.org/10.1002/iub.1933).
- [29] M. Wehrmann, P. Billard, A. Martin-Meriadec, A. Zegeye, and J. Klebensberger, “Functional Role of Lanthanides in Enzymatic Activity and Transcriptional Regulation of Pyrroloquinoline Quinone-Dependent Alcohol Dehydrogenases in *Pseudomonas putida* KT2440,” *MBio*, vol. 8, no. 3, pp. e00570-17, Jul. 2017, doi: [10.1128/mBio.00570-17](https://doi.org/10.1128/mBio.00570-17).
- [30] L. Molina *et al.*, “Survival of *Pseudomonas putida* KT2440 in soil and in the rhizosphere of plants under greenhouse and environmental conditions,” *Soil Biol. Biochem.*, vol. 32, no. 3, pp. 315–321, 2000, doi: [https://doi.org/10.1016/S0038-0717\(99\)00156-X](https://doi.org/10.1016/S0038-0717(99)00156-X).
- [31] A. Segura, P. de Wit, and G. M. Preston, “Life of microbes that interact with plants,” *Microb. Biotechnol.*, vol. 2, no. 4, pp. 412–415, Jul. 2009, doi: [10.1111/j.1751-7915.2009.00129.x](https://doi.org/10.1111/j.1751-7915.2009.00129.x).
- [32] Tyc Olaf, C. Song, J. S. Dickschat, M. Vos, and P. Garbeva, “The Ecological Role of Volatile and Soluble Secondary Metabolites Produced by Soil Bacteria,” *Trends Microbiol.*, vol. 25, no. 4, pp. 280–292, 2017, doi: <https://doi.org/10.1016/j.tim.2016.12.002>.
- [33] K. N. Timmis, “*Pseudomonas putida*: a cosmopolitan opportunist par excellence,” *Environ. Microbiol.*, vol. 4, no. 12, pp. 779–781, Dec. 2002, doi: <https://doi.org/10.1046/j.1462-2920.2002.00365.x>.
- [34] M. Espinosa-Urgel, R. Kolter, and J.-L. Ramos, “Root colonization by *Pseudomonas putida*: love,” *Microbiology*, vol. 148, no. 2, pp. 341–344, 2002, [Online]. Available: <http://mic.sgmjournals.org/content/148/2/341.short>.
- [35] X. Wu, S. Monchy, S. Taghavi, W. Zhu, J. Ramos, and D. van der Lelie,

References

- “Comparative genomics and functional analysis of niche-specific adaptation in *Pseudomonas putida*,” *FEMS Microbiol. Rev.*, vol. 35, no. 2, pp. 299–323, Mar. 2011, doi: 10.1111/j.1574-6976.2010.00249.x.
- [36] J. I. Jiménez, B. Miñambres, J. L. García, and E. Díaz, “Genomic analysis of the aromatic catabolic pathways from *Pseudomonas putida* KT2440,” *Environ. Microbiol.*, vol. 4, no. 12, pp. 824–841, Dec. 2002, doi: <https://doi.org/10.1046/j.1462-2920.2002.00370.x>.
- [37] K. E. Nelson *et al.*, “Complete genome sequence and comparative analysis of the metabolically versatile *Pseudomonas putida* KT2440,” *Environ. Microbiol.*, vol. 4, no. 12, pp. 799–808, Dec. 2002, doi: 10.1046/j.1462-2920.2002.00366.x.
- [38] E. Belda *et al.*, “The revisited genome of *Pseudomonas putida* KT2440 enlightens its value as a robust metabolic chassis,” *Environ. Microbiol.*, vol. 18, no. 10, pp. 3403–3424, Oct. 2016, doi: <https://doi.org/10.1111/1462-2920.13230>.
- [39] W.-J. Li *et al.*, “Unraveling 1,4-Butanediol Metabolism in *Pseudomonas putida* KT2440,” *Front. Microbiol.*, vol. 11, p. 382, 2020, doi: 10.3389/fmicb.2020.00382.
- [40] J. A. Duine, “The PQQ story,” *J. Biosci. Bioeng.*, vol. 88, no. 3, pp. 231–236, 1999, doi: [https://doi.org/10.1016/S1389-1723\(00\)80002-X](https://doi.org/10.1016/S1389-1723(00)80002-X).
- [41] M. Naveed, K. Tariq, and H. Sadia, “The Life History of Pyrroloquinoline Quinone (PQQ): A Versatile Molecule with Novel Impacts on Living Systems,” no. January, 2017, doi: 10.15406/ijmboa.2016.01.00005.
- [42] H. Toyama, “Pyrroloquinoline Quinone (PQQ),” *Industrial Biotechnology of Vitamins, Biopigments, and Antioxidants*. pp. 367–388, Mar. 28, 2016, doi: <https://doi.org/10.1002/9783527681754.ch13>.
- [43] J. G. Hauge, “Glucose Dehydrogenase of *Bacterium anitratum*: an Enzyme with a Novel Prosthetic Group,” *J. Biol. Chem.*, vol. 239, no. 11, pp. 3630–3639, 1964, doi: [https://doi.org/10.1016/S0021-9258\(18\)91183-X](https://doi.org/10.1016/S0021-9258(18)91183-X).
- [44] J. S. Pober, J. White, and H. Bayley, “A novel coenzyme from bacterial primary alcohol dehydrogenases,” vol. 280, no. August, 1979.
- [45] H. Toyama, A. Fujii, K. Matsushita, E. Shinagawa, M. Ameyama, and O. Adachi, “Three distinct quinoprotein alcohol dehydrogenases are expressed when *Pseudomonas putida* is grown on different alcohols,” *J. Bacteriol.*, vol. 177, no. 9, pp. 2442–2450, May 1995, doi: 10.1128/jb.177.9.2442-2450.1995.
- [46] H. Toyama, F. S. Mathews, O. Adachi, and K. Matsushita,

References

- “Quinohemoprotein alcohol dehydrogenases: structure, function, and physiology,” *Arch. Biochem. Biophys.*, vol. 428, no. 1, pp. 10–21, 2004, doi: <https://doi.org/10.1016/j.abb.2004.03.037>.
- [47] B. Mennenga and C. W. M. Kay, “Quinoprotein ethanol dehydrogenase from *Pseudomonas aeruginosa*: the unusual disulfide ring formed by adjacent cysteine residues is essential for efficient electron transfer to cytochrome c 550,” vol. 550, pp. 361–367, 2009, doi: 10.1007/s00203-009-0460-4.
- [48] O. Adachi, Y. Ano, H. Toyama, and K. Matsushita, “Biooxidation with PQQ- and FAD-Dependent Dehydrogenases,” *Modern Biooxidation*. pp. 1–41, Jul. 18, 2007, doi: <https://doi.org/10.1002/9783527611522.ch1>.
- [49] P. R. Afolabi *et al.*, “Site-Directed Mutagenesis and X-ray Crystallography of the PQQ-Containing Quinoprotein Methanol Dehydrogenase and Its Electron Acceptor, Cytochrome cL,” *Biochemistry*, vol. 40, no. 33, pp. 9799–9809, Aug. 2001, doi: 10.1021/bi002932l.
- [50] M. Wikström, V. Sharma, V. R. I. Kaila, J. P. Hosler, and G. Hummer, “New Perspectives on Proton Pumping in Cellular Respiration,” *Chem. Rev.*, vol. 115, no. 5, pp. 2196–2221, Mar. 2015, doi: 10.1021/cr500448t.
- [51] M. L. Björck and P. Brzezinski, “Control of transmembrane charge transfer in cytochrome c oxidase by the membrane potential,” *Nat. Commun.*, vol. 9, no. 1, p. 3187, 2018, doi: 10.1038/s41467-018-05615-5.
- [52] M. Leopoldini, N. Russo, and M. Toscano, “The Preferred Reaction Path for the Oxidation of Methanol by PQQ-Containing Methanol Dehydrogenase: Addition–Elimination versus Hydride-Transfer Mechanism,” *Chem. – A Eur. J.*, vol. 13, no. 7, pp. 2109–2117, Feb. 2007, doi: <https://doi.org/10.1002/chem.200601123>.
- [53] Y.-J. Zheng, Z. Xia, Z. Chen, F. S. Mathews, and T. C. Bruice, “Catalytic mechanism of quinoprotein methanol dehydrogenase: A theoretical and x-ray crystallographic investigation,” *Proc. Natl. Acad. Sci.*, vol. 98, no. 2, pp. 432 LP – 434, Jan. 2001, doi: 10.1073/pnas.98.2.432.
- [54] A. Jongejan, J. A. Jongejan, and W. R. Hagen, “Direct hydride transfer in the reaction mechanism of quinoprotein alcohol dehydrogenases: a quantum mechanical investigation,” *J. Comput. Chem.*, vol. 22, no. 15, pp. 1732–1749, Nov. 2001, doi: <https://doi.org/10.1002/jcc.1128>.
- [55] S. Arias, E. R. Olivera, M. Arcos, G. Naharro, and J. M. Luengo, “Genetic analyses and molecular characterization of the pathways involved in the conversion of 2-phenylethylamine and 2-phenylethanol into phenylacetic acid in *Pseudomonas putida* U,” vol. 10, pp. 413–432, 2008, doi:

References

- 10.1111/j.1462-2920.2007.01464.x.
- [56] F. Chu and E. Lidstrom, "XoxF Acts as the Predominant Methanol Dehydrogenase in the Type I Methanotroph *Methylomicrobium buryatense*," vol. 198, no. 8, pp. 1317–1325, 2016, doi: 10.1128/JB.00959-15.Editor.
- [57] T. Keitel, A. Diehl, T. Knaute, and J. J. Stezowski, "X-ray Structure of the Quinoprotein Ethanol Dehydrogenase from *Pseudomonas aeruginosa* : Basis of Substrate Specificity," 2000, doi: 10.1006/jmbi.2000.3603.
- [58] X. Robert and P. Gouet, "Deciphering key features in protein structures with the new ENDscript server," *Nucleic Acids Res.*, vol. 42, no. W1, pp. W320–W324, Jul. 2014, doi: 10.1093/nar/gku316.
- [59] P. Reichmann and H. Gorisch, "Cytochrome c550 from *Pseudomonas aeruginosa*," *Biochem. J.*, vol. 289, no. 1, pp. 173–178, 1993, doi: 10.1042/bj2890173.
- [60] E. Arslan, H. Schulz, R. Zufferey, P. Künzler, and L. Thöny-Meyer, "Overproduction of the *Bradyrhizobium japonicum* c-Type Cytochrome Subunits of the *cbb3* Oxidase in *Escherichia coli*," *Biochem. Biophys. Res. Commun.*, vol. 251, no. 3, pp. 744–747, 1998, doi: <https://doi.org/10.1006/bbrc.1998.9549>.
- [61] P. Reichmann and H. Görisch, "Cytochrome c550 from *Pseudomonas aeruginosa*," *Biochem. J.*, vol. 289 (Pt 1, no. Pt 1, pp. 173–178, Jan. 1993, doi: 10.1042/bj2890173.
- [62] N. C. Martinez-gomez, "Lanthanide-dependent alcohol dehydrogenases require an essential aspartate residue for metal coordination and enzymatic function," *J. Biol. Chem.*, vol. 295, no. 24, pp. 8272–8284, 2020, doi: 10.1074/jbc.RA120.013227.
- [63] B. Ø. Ø. Jahn *et al.*, "Similar but Not the Same : First Kinetic and Structural Analyses of a Methanol Dehydrogenase Containing a Europium Ion in the Active Site," pp. 1147–1153, 2018, doi: 10.1002/cbic.201800130.
- [64] Y. W. Deng, S. Y. Ro, and A. C. Rosenzweig, "Structure and function of the lanthanide-dependent methanol dehydrogenase XoxF from the methanotroph *Methylomicrobium buryatense* 5GB1C.," *J. Biol. Inorg. Chem. JBIC a Publ. Soc. Biol. Inorg. Chem.*, vol. 23, no. 7, pp. 1037–1047, Oct. 2018, doi: 10.1007/s00775-018-1604-2.
- [65] Z. Xia, W. Dai, Y. Zhang, S. A. White, G. D. Boyd, and F. S. Mathews, "Determination of the Gene Sequence and the Three-dimensional Structure at 2.4 Å Resolution of Methanol Dehydrogenase from *Methylophilus W3A1*," pp. 480–501, 1996.

References

- [66] A. Oubrie, J. Rozeboom, K. H. Kalk, E. G. Huizinga, and B. W. Dijkstra, "Crystal Structure of Quinohemoprotein Alcohol Dehydrogenase from *Comamonas testosteroni*," vol. 277, no. 5, pp. 3727–3732, 2002, doi: 10.1074/jbc.M109403200.
- [67] M. A. Culpepper and A. C. Rosenzweig, "Structure and protein-protein interactions of methanol dehydrogenase from *Methylococcus capsulatus* (Bath).," *Biochemistry*, vol. 53, no. 39, pp. 6211–6219, Oct. 2014, doi: 10.1021/bi500850j.
- [68] S. Sinnecker, A. Rajendran, A. Klamt, M. Diedenhofen, and F. Neese, "Calculation of solvent shifts on electronic g-tensors with the conductor-like screening model (COSMO) and its self-consistent generalization to real solvents (direct COSMO-RS)," *J. Phys. Chem. A*, vol. 110, no. 6, pp. 2235–2245, 2006.
- [69] A. L. Allred, "Electronegativity values from thermochemical data," *J. Inorg. Nucl. Chem.*, vol. 17, no. 3, pp. 215–221, 1961, doi: [https://doi.org/10.1016/0022-1902\(61\)80142-5](https://doi.org/10.1016/0022-1902(61)80142-5).
- [70] J. E. Huheey, E. A. Keiter, R. L. Keiter, and O. K. Medhi, *Inorganic chemistry: principles of structure and reactivity*. 2013.
- [71] M. Nojiri, D. Hira, K. Yamaguchi, T. Okajima, K. Tanizawa, and S. Suzuki, "Crystal structures of cytochrome c(L) and methanol dehydrogenase from *Hyphomicrobium denitrificans*: structural and mechanistic insights into interactions between the two proteins.," *Biochemistry*, vol. 45, no. 11, pp. 3481–3492, Mar. 2006, doi: 10.1021/bi051877j.
- [72] J. Huang, Z. Yu, J. Groom, J. C. Angela, T. Yasuo, and L. Chistoserdova, "Rare earth element alcohol dehydrogenases widely occur among globally distributed, numerically abundant and environmentally important microbes," *ISME J.*, pp. 2005–2017, 2019, doi: 10.1038/s41396-019-0414-z.
- [73] T. Keitel, A. Diehl, T. Knaute, J. J. Stezowski, W. Höhne, and H. Görisch, "X-ray structure of the quinoprotein ethanol dehydrogenase from *Pseudomonas aeruginosa*: basis of substrate specificity.," *J. Mol. Biol.*, vol. 297, no. 4, pp. 961–974, Apr. 2000, doi: 10.1006/jmbi.2000.3603.
- [74] M. Flores-Encarnación, M. Sánchez-Cuevas, and F. Ortiz-Gutiérrez, "[The PQQ-dehydrogenases. A novel example of bacterial quinoproteins].," *Rev. Latinoam. Microbiol.*, vol. 46, no. 1–2, pp. 47–59, 2004.
- [75] R. Paul, "Systematics and surprises in lanthanide coordination chemistry," *Coord. Chem. Rev.*, 2021, doi: 10.1016/j.ccr.2017.01.011.

References

- [76] I. Dokmanic, “research papers Metals in proteins : correlation between the metal-ion type , coordination number and the amino-acid residues involved in the coordination research papers,” pp. 257–263, 2008, doi: 10.1107/S090744490706595X.
- [77] A. A. Yaroshevsky, “Abundances of chemical elements in the Earth’s crust,” *Geochemistry Int.*, vol. 44, no. 1, pp. 48–55, 2006, doi: 10.1134/S001670290601006X.
- [78] N. M. Good, R. S. Moore, C. J. Suriano, and N. C. Martinez-gomez, “methanol oxidation activities of lanthanide-dependent alcohol dehydrogenases XoxF1 and ExaF from *Methylobacterium extorquens*,” *Sci. Rep.*, no. October 2018, pp. 1–12, 2019, doi: 10.1038/s41598-019-41043-1.
- [79] S. Lena and J. Daumann, “As featured in : Dalton,” 2018, doi: 10.1039/c8dt01238e.
- [80] S. Tsushima, “Lanthanide-induced conformational change of methanol dehydrogenase involving coordination change of cofactor pyrroloquinoline quinone †,” pp. 21979–21983, 2019, doi: 10.1039/c9cp03953h.
- [81] Z. Chen *et al.*, “° Resolution of a Structure at 1 . 9 Å Quinohemoprotein Alcohol Dehydrogenase from *Pseudomonas putida* HK5,” vol. 10, no. 02, pp. 837–849, 2002.
- [82] E. Weber, R. Gruetzner, S. Werner, C. Engler, and S. Marillonnet, “Assembly of designer TAL effectors by Golden Gate cloning,” *PLoS One*, vol. 6, no. 5, pp. e19722–e19722, 2011, doi: 10.1371/journal.pone.0019722.
- [83] S. Marillonnet and R. Grütznier, “Synthetic DNA Assembly Using Golden Gate Cloning and the Hierarchical Modular Cloning Pipeline,” *Curr. Protoc. Mol. Biol.*, vol. 130, no. 1, p. e115, Mar. 2020, doi: <https://doi.org/10.1002/cpmb.115>.
- [84] Y.-C. Chen, L.-A. Chen, S.-J. Chen, M.-C. Chang, and T.-L. Chen, “A modified osmotic shock for periplasmic release of a recombinant creatinase from *Escherichia coli*,” *Biochem. Eng. J.*, vol. 19, no. 3, pp. 211–215, 2004, doi: <https://doi.org/10.1016/j.bej.2004.03.001>.
- [85] A. Daudi and J. A. O’Brien, “Detection of Hydrogen Peroxide by DAB Staining in *Arabidopsis* Leaves,” *Bio-protocol*, vol. 2, no. 18, p. e263, 2012, [Online]. Available: <https://pubmed.ncbi.nlm.nih.gov/27390754>.
- [86] M. W. Bowler *et al.*, “MASSIF-1: a beamline dedicated to the fully automatic characterization and data collection from crystals of biological macromolecules,” *J. Synchrotron Radiat.*, vol. 22, no. 6, pp. 1540–1547,

- 2015.
- [87] M. Cianci *et al.*, “P13, the EMBL macromolecular crystallography beamline at the low-emittance PETRA III ring for~high- and low-energy phasing with variable beam focusing,” *J. Synchrotron Radiat.*, vol. 24, no. 1, pp. 323–332, Jan. 2017, doi: 10.1107/S1600577516016465.
- [88] U. Mueller *et al.*, “The macromolecular crystallography beamlines at BESSY II of the Helmholtz-Zentrum Berlin: Current status and perspectives,” *Eur. Phys. J. Plus*, vol. 130, no. 7, pp. 1–10, 2015.
- [89] W. Kabsch, “XDS.,” *Acta Crystallogr. D. Biol. Crystallogr.*, vol. 66, no. Pt 2, pp. 125–132, Feb. 2010, doi: 10.1107/S0907444909047337.
- [90] A. J. McCoy, R. W. Grosse-Kunstleve, P. D. Adams, M. D. Winn, L. C. Storoni, and R. J. Read, “Phaser crystallographic software,” *J. Appl. Crystallogr.*, vol. 40, no. 4, pp. 658–674, 2007.
- [91] P. Emsley and K. Cowtan, “Coot: model-building tools for molecular graphics,” *Acta Crystallogr. Sect. D Biol. Crystallogr.*, vol. 60, no. 12, pp. 2126–2132, 2004.
- [92] P. D. Adams *et al.*, “PHENIX: a comprehensive Python-based system for macromolecular structure solution,” *Acta Crystallogr. Sect. D Biol. Crystallogr.*, vol. 66, no. 2, pp. 213–221, 2010.
- [93] L. Schrödinger, “The {PyMOL} Molecular Graphics Development Component, Version~ 1.3.” Nov, 2010.
- [94] S. G. Balasubramani *et al.*, “TURBOMOLE: Modular program suite for ab initio quantum-chemical and condensed-matter simulations,” *J. Chem. Phys.*, vol. 152, no. 18, p. 184107, May 2020, doi: 10.1063/5.0004635.
- [95] M. G. Medvedev, I. S. Bushmarinov, J. Sun, J. P. Perdew, and K. A. Lyssenko, “Density functional theory is straying from the path toward the exact functional,” *Science (80-.)*, vol. 355, no. 6320, pp. 49–52, 2017.
- [96] A. Schäfer, H. Horn, and R. Ahlrichs, “Fully optimized contracted Gaussian basis sets for atoms Li to Kr,” *J. Chem. Phys.*, vol. 97, no. 4, pp. 2571–2577, Aug. 1992, doi: 10.1063/1.463096.
- [97] J. P. Perdew, M. Ernzerhof, and K. Burke, “Rationale for mixing exact exchange with density functional approximations,” *J. Chem. Phys.*, vol. 105, no. 22, pp. 9982–9985, Dec. 1996, doi: 10.1063/1.472933.
- [98] F. Weigend and A. Baldes, “Segmented contracted basis sets for one- and two-component Dirac–Fock effective core potentials,” *J. Chem. Phys.*, vol. 133, no. 17, p. 174102, Nov. 2010, doi: 10.1063/1.3495681.

References

- [99] D. Figgen, G. Rauhut, M. Dolg, and H. Stoll, "Energy-consistent pseudopotentials for group 11 and 12 atoms: adjustment to multi-configuration Dirac–Hartree–Fock data," *Chem. Phys.*, vol. 311, no. 1–2, pp. 227–244, 2005.
- [100] B. Metz, H. Stoll, and M. Dolg, "Small-core multiconfiguration-Dirac–Hartree–Fock-adjusted pseudopotentials for post-d main group elements: Application to PbH and PbO," *J. Chem. Phys.*, vol. 113, no. 7, pp. 2563–2569, 2000.
- [101] M. Dolg, H. Stoll, A. Savin, and H. Preuss, "Energy-adjusted pseudopotentials for the rare earth elements," *Theor. Chim. Acta*, vol. 75, no. 3, pp. 173–194, 1989.
- [102] A. Moritz, X. Cao, and M. Dolg, "Quasirelativistic energy-consistent 5f-in-core pseudopotentials for divalent and tetravalent actinide elements," *Theor. Chem. Acc.*, vol. 118, no. 5, pp. 845–854, 2007.
- [103] A. Klamt and G. Schüürmann, "COSMO: a new approach to dielectric screening in solvents with explicit expressions for the screening energy and its gradient," *J. Chem. Soc. Perkin Trans. 2*, no. 5, pp. 799–805, 1993.
- [104] M. Jerabek-Willemsen *et al.*, "MicroScale Thermophoresis: Interaction analysis and beyond," *J. Mol. Struct.*, vol. 1077, pp. 101–113, 2014, doi: <https://doi.org/10.1016/j.molstruc.2014.03.009>.
- [105] M. Jerabek-Willemsen, C. J. Wienken, D. Braun, P. Baaske, and S. Duhr, "Molecular Interaction Studies Using Microscale Thermophoresis," *Assay Drug Dev. Technol.*, vol. 9, no. 4, pp. 342–353, Aug. 2011, doi: 10.1089/adt.2011.0380.
- [106] T. E. Wales, K. E. Fadgen, G. C. Gerhardt, and J. R. Engen, "High-Speed and High-Resolution UPLC Separation at Zero Degrees Celsius," *Anal. Chem.*, vol. 80, no. 17, pp. 6815–6820, Sep. 2008, doi: 10.1021/ac8008862.
- [107] S. J. Geromanos *et al.*, "The detection, correlation, and comparison of peptide precursor and product ions from data independent LC-MS with data dependant LC-MS/MS.," *Proteomics*, vol. 9, no. 6, pp. 1683–1695, Mar. 2009, doi: 10.1002/pmic.200800562.
- [108] G.-Z. Li, J. P. C. Vissers, J. C. Silva, D. Golick, M. V Gorenstein, and S. J. Geromanos, "Database searching and accounting of multiplexed precursor and product ion spectra from the data independent analysis of simple and complex peptide mixtures.," *Proteomics*, vol. 9, no. 6, pp. 1696–1719, Mar. 2009, doi: 10.1002/pmic.200800564.

References

- [109] M. Osorio-Valeriano *et al.*, “ParB-type DNA Segregation Proteins Are CTP-Dependent Molecular Switches.,” *Cell*, vol. 179, no. 7, pp. 1512-1524.e15, Dec. 2019, doi: 10.1016/j.cell.2019.11.015.

7. Appendix

7.1. Supporting tables

Table S 1. List of oligonucleotides

oligonucleotide	Sequence (5'-3')
252_PedE_BsaHis_fwd	ttaa ggtctc ccatgg gccaccatcaccatcaccatgccagcacaccccgtg
253_PedE_XBsa_rev	ttaaggtcctctcagagtaacgttgatgagctctgtgtcccag
254_PedE_D194G_fwd	ttaaggtctc cggcgaattcggcgtggtcggcc
255_PedE_D194G_rev	ttaaggtctc tcgccccggagctccgtgga
256_PedE_E195D_fwd	ttaaggtctctgatttcggcgtggtcggcc
257_PedE_E195D_rev	ttaaggtctcaaatcatcgccggagctgccg
15_PedE_XhoI_Rv	ttaa ctcgag tta acgttgatgagctctgtgtccc
16_pedE_His6_XhoI_RV	ttaactcgagttagtggtgatggtgatgatgacgttgatgagctctgtgtccc
25_pedE_S295D_Fw	cccaacgatgcctgggacttcgacggcaacaacagagctggtgct
26_pedE_S295D_RV	gaagtcaccaggcatcgttggg
17_PedH_NcoI_FW	ttaacatggctgtcagcaatgaagaaatcctccag
18_pdeH_NcoI_6His_FW	ttaacatgggccaccatcaccatcaccatgctgtcagcaatgaagaaatcctccag
19_pedH_XhoI_Rv	ttaactcgagttatggcttgacgcttgccgtttgc
20_PedH_6His_XhoI_RV	ttaactcgagttagtggtgatggtgatgatgagcttgatgagcttgccgtttgc
166_PedH_E199G_fwd	ttaa ggtctc ggc ggc ttcggcgtggtggcaag
167_PedH_E199G_rev	ttaa ggtctc gcc gccgccggcaacgcctgt
15_PedE_XhoI_Rv	ttaa ctcgag tta acgttgatgagctctgtgtccc
16_pedE_His6_XhoI_RV	ttaactcgagttagtggtgatggtgatgatgacgttgatgagctctgtgtccc
252_PedE_BsaHis_fwd	ttaa ggtctc ccatgg gccaccatcaccatcaccatgccagcacaccccgtg
253_PedE_XBsa_rev	ttaaggtcctctcagagtaacgttgatgagctctgtgtcccag
254_PedE_D194G_fwd	ttaaggtctc cggcgaattcggcgtggtcggcc
255_PedE_D194G_rev	ttaaggtctc tcgccccggagctccgtgga
256_PedE_E195D_fwd	ttaaggtctctgatttcggcgtggtcggcc
257_PedE_E195D_rev	ttaaggtctcaaatcatcgccggagctgccg
258_PedH_BsaI_fwd	ttaa ggtctc ccatgg ctgtcagcaatgaagaaatcctcca
259_PedH_HBsaI_rev	ttaaggtcctctcagagttagtggtgatggtgatgatgagcttgatgagcttgccg
260_PedH_G198D_fwd	ttaaggtctc gau gagttcggcgtggtggcaag
261_PedH_G198D_rev	ttaaggtcctctcatcgccggcaacgcctgt
262_PedH_E199D_fwd	ttaaggtctcggcgauttcggcgtggtggcaag
263_PedH_E199D_rev	ttaaggtctcatcgccggcaacgcctgt
264_PedH_D325S_fwd	ttaaggtctcttcagcggcgtcaacagctgatctcg
265_PedH_D325S_rev	ttaaggtctcgtgaagtcccagccgtcatgcg
100_PedH_W521S_fwd	ttaa ggtctc tcg ggcggcgggtgccgctg
101_PedH_W521S_rev	ttaa ggtctc gcc cga gccggagactaccga

Appendix

102_PedH_W521A_fwd	ttaa ggtctc gcg ggcggcgcggtgccgctg
103_PedH_W521A_rev	ttaa ggtctc gcc cgc gccggagactaccga
104_PedH_W521Q_fwd	ttaa ggtctc cag ggcggcgcggtgccgctg
105_PedH_W521Q_rev	ttaa ggtctc gcc ctg gccggagactaccga
106_PedH_F375I_Fwd	ttaa ggtctc gtg atc gtcgcccggccttctc
107_PedH_F375I_rev	ttaa ggtctc gat caccgagctgcccttggc
108_PedH_F375V_Fwd	ttaa ggtctc gtg gtc gtcgcccggccttctc
109_PedH_F375V_rev	ttaa ggtctc gac caccgagctgcccttggc
110_PedH_F412V_fwd	ttaa ggtctc gtc ctcggcgccaagaactggatg
111_PedH_F412V_rev	ttaa ggtctc gag gac ggccggcgcgacgaa
112_PedH_F412I_fwd	ttaa ggtctc atc ctcggcgccaagaactggatg
113_PedH_F412I_rev	ttaa ggtctc gag gat ggccggcgcgacgaa
114_PedH_W561A_fwd	ttaa ggtctc gcg ggcggcggaagtggcctaacgg
115_PedH_W561A_rev	ttaa ggtctc gcc cgc cagcggcaccgcgcc
116_PedH_W561S_Fwd	ttaa ggtctc tcg ggcggcggaagtggcctaacgg
117_PedH_W561S_rev	ttaa ggtctc gcc cga cagcggcaccgcgcc
118_PedH_W561Q_Fwd	ttaa ggtctc cag ggcggcggaagtggcctaacgg
119_PedH_W561Q_rev	ttaa ggtctc gcc ctg cagcggcaccgcgcc
120_PedH_W561A_rev	ttaa ggtctc gcc cgc cagcggcaccgcgcc gccc
121_PedH_W561S_rev	ttaa ggtctc gcc cga cagcggcaccgcgcc gccc
447_PedH_C131S_fwd	ttaa ggtctc agctgcgacgtaatcaaccgcggcg
122_PedH_W561Q_rev	ttaa ggtctc gcc ctg cagcggcaccgcgcc gccc
448_PedH_C131S_rev	ttaa ggtctc gctgcagggcggtatgcatccg
449_PedH_C132S_fwd	ttaa ggtctc tgcagcgcgtaatcaaccgcggcg
450_PedH_C132S_rev	ttaa ggtctc gcagctggggcggtatgcatccg
451_PedH_C131S_C132S_fwd	ttaa ggtctc agcagcgcgtaatcaaccgcggcg
452_PedH_C131S_C132S_rev	ttaa ggtctc gctgctggggcggtatgcatccg
453_Pp_pedF_B_fwd	ttaa ggtctc cca tgg gc catggcaatgtagtcccacag
454_Pp_pedF_B_rev	ttaaggtctcctcgagtactctcgcagtgcaagc
133_Pp_pedF_Bsal_fwd	ttaa ggtctc c atg ggc catggcaacgtggtgcccc
134_Pp_pedF_Bsal_H6_fwd	ttaa ggtctc c atg ggc caccatcaccatcaccat catggcaacgtggtgcccc
135_Pp_pedF_Bsal_H6_rev	ttaa ggtctc ctcgag tta gtggtgatggtgatgatg ctctcgcagtgcaagc
471_PedH_L560W_W561A_fwd	ttaa ggtctc tgggccccggcggaagtggcc
472_PedH_L560W_W561A_rev	ttaa ggtctc cccccacggcaccgcgcgcccc
473_PedH_L560R_W561A_fwd	ttaa ggtctc cgcgcggcgcggaagtggcc
474_PedH_L560R_W561A_rev	ttaa ggtctc cgcgcggcgaccgcgcgcccc
475_PedH_F459W_fwd	ttaa ggtctc tgg accatcaagccgtcaatgaagac
476_PedH_F459W_rev	ttaa ggtctc ggtccagccggcaccgaggaacgccgc
477_PedH_F459R_fwd	ttaa ggtctc cgaccatcaagccgtcaatgaagac
478_PedH_F459R_rev	ttaaggtctcggcgccggcaccgaggaacgccgc
479_PedH_L455R_fwd	ttaaggtctcggcggtgccgctcaccatcaagcc
480_PedH_L455R_rev	ttaaggtctcaccgccaacgcggcacccttcttataggcg
480_PedH_L455R_rev	ttaaggtctcaccgccaacgcggcacccttcttataggcg

Table S 2. List of Plasmids.

Plasmid	Vector	Insert*	Tag
EE0009	pET-24d(+)	<i>pedE</i>	N-His ₆
EE0010	pET-24d(+)	<i>pedE</i>	C-His ₆
EE0011	pET-24d(+)	<i>pedH</i>	N-His ₆
EE0012	pET-24d(+)	<i>pedH</i>	C-His ₆
EE0017	pET-24d(+)	<i>pedE</i> (S295D)	N-His ₆
EE0018	pET-24d(+)	<i>pedE</i> (S295D)	C-His ₆
EE0053	pET-24d(+)	<i>pedE_D194G_S334D</i>	N-His ₆
EE0054	pET-24d(+)	<i>pedE_D194G</i>	N-His ₆
EE0055	pET-24d(+)	<i>pedE_E195D</i>	N-His ₆
EE0056	pET-24d(+)	<i>pedH_G198D_D325S</i>	C-His ₆
EE0057	pET-24d(+)	<i>pedH_D325S</i>	C-His ₆
EE0058	pET-24d(+)	<i>pedH_G198D</i>	C-His ₆
EE0059	pET-24d(+)	<i>pedH_E199D</i>	C-His ₆
EE0067	pET-24d(+)	<i>pedH_F412V_W561A</i>	C-His ₆
EE0068	pET-24d(+)	<i>pedH_C131S</i>	C-His ₆
EE0069	pET-24d(+)	<i>pedH_C132S</i>	C-His ₆
EE0070	pET-24d(+)	<i>pedH_C131_C132S</i>	C-His ₆
EE0073	pET-24d(+)	<i>pedH_F412V_W561A_L560W</i>	C-His ₆
EE0074	pET-24d(+)	<i>pedH_F412V_W561A_L560R</i>	C-His ₆
EE0075	pET-24d(+)	<i>pedH_F412V_W561A_F459W</i>	C-His ₆
EE0076	pET-24d(+)	<i>pedH_F412V_W561A_F459R</i>	C-His ₆
EE0077	pET-24d(+)	<i>pedH_F412V_W561A_L455R</i>	C-His ₆
EE0080	pEC-86	<i>Ccm</i> cluster genes	-

Appendix

EE0084	pET-22b(+)	<i>pedF</i>	N-His ₆
EE0085	pET-22b(+)	<i>pedF</i>	C-His ₆
EE0088	pET-24d(+)	<i>pedH_F412V_W561A_F459W_L560R</i>	C-His ₆
EE0089	pET-24d(+)	<i>pedH_F412V_W561A_G198D_D325S</i>	C-His ₆

* represents encoding genes without the nucleotides corresponding for the signal peptide (1-34, 1-28, and 1-24 in case of *pedE*, *pedH*, and *pedF*, respectively).

7.2. Supporting Figures

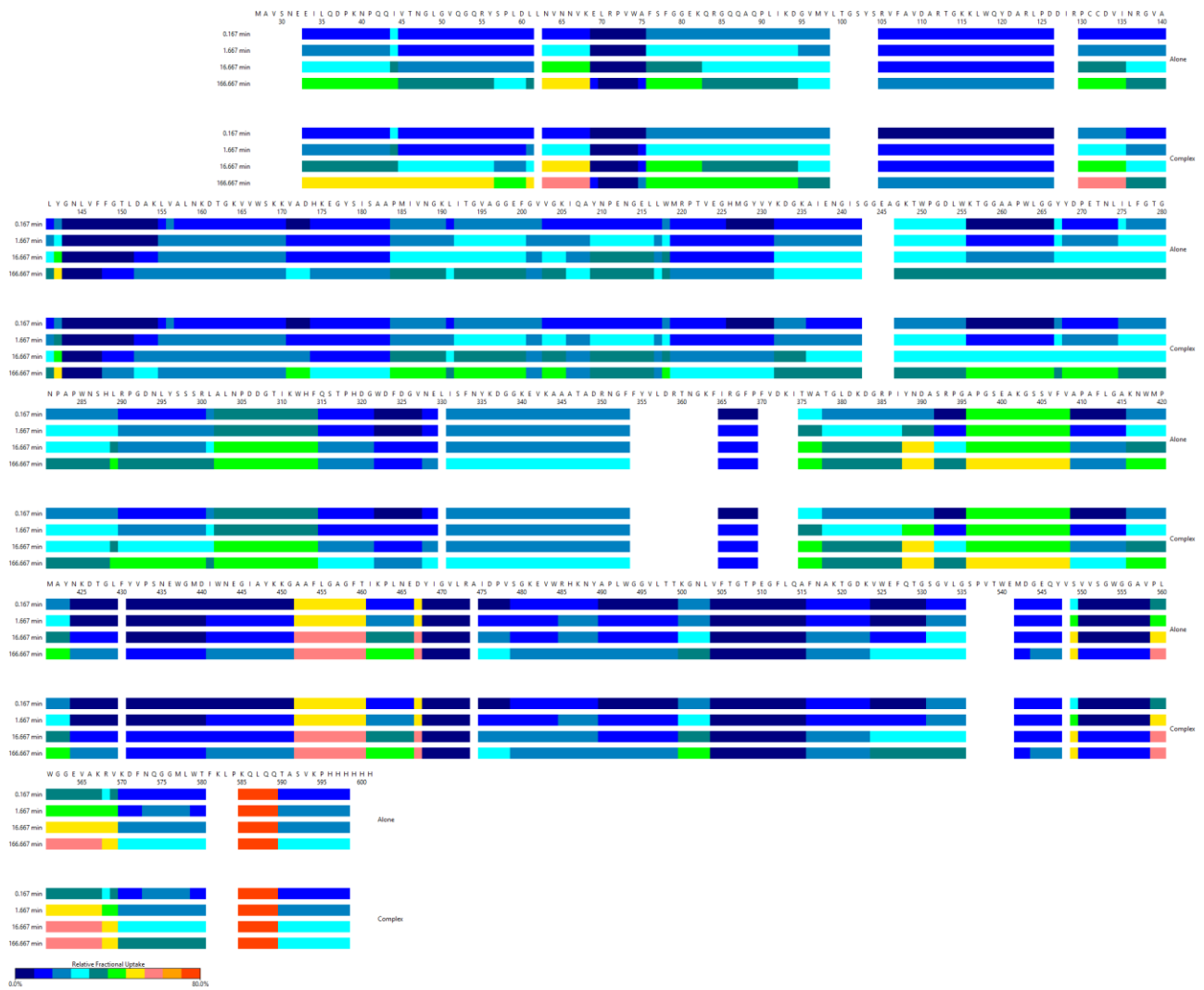


Figure S 1. Relative HDX of PedH. D-incorporation of PedH colored in rainbow from blue (0%) to red (80% D-incorporation).

Appendix

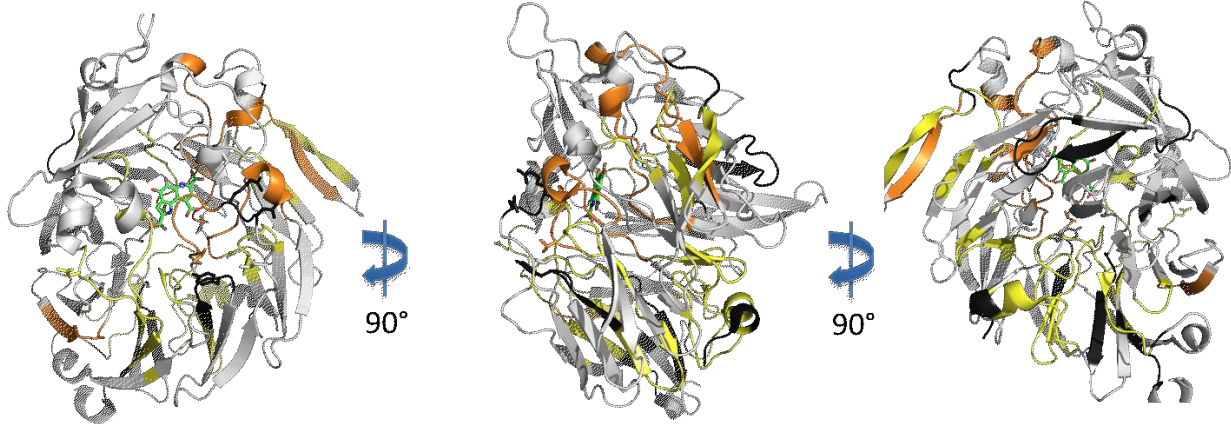
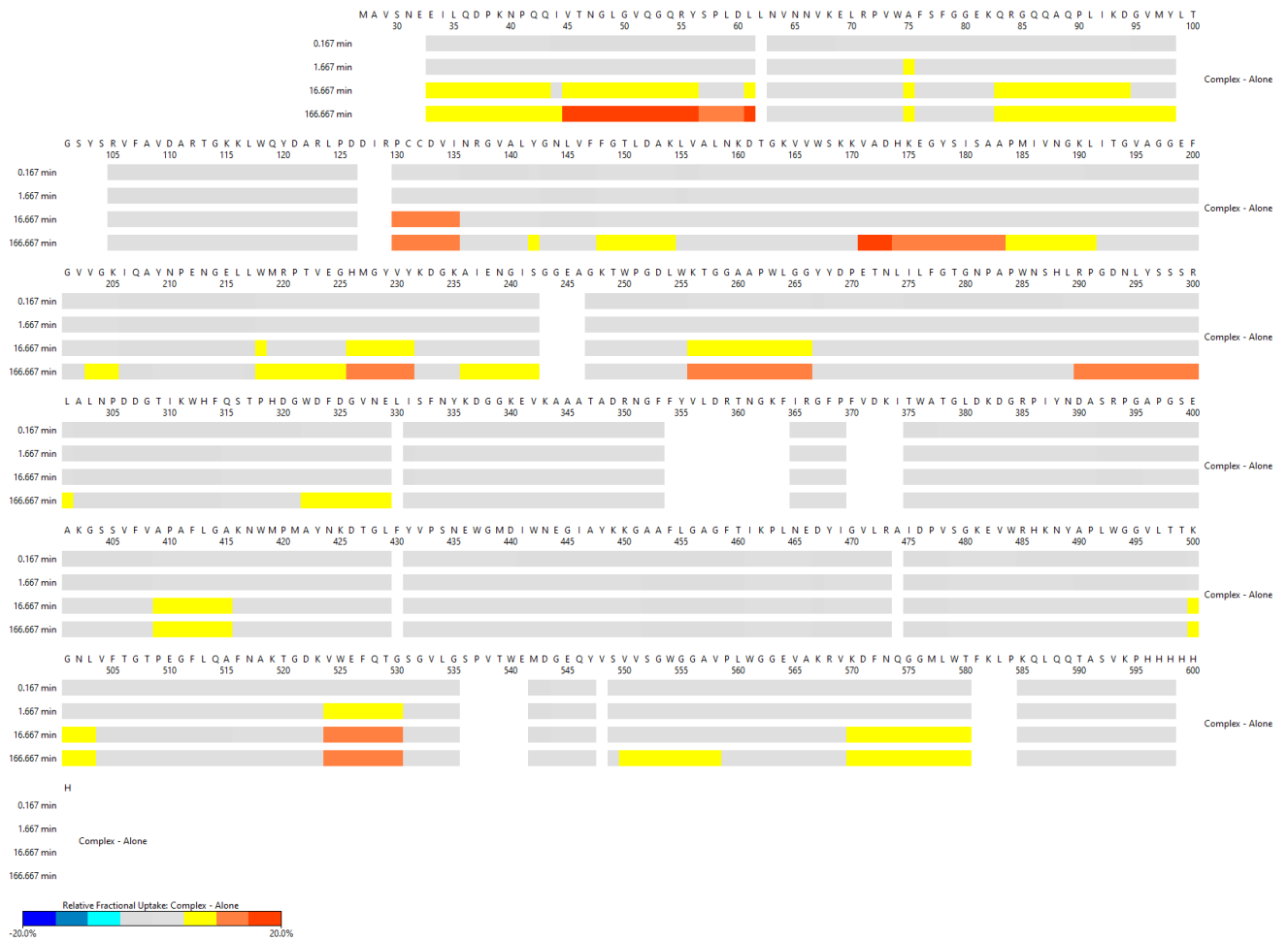


Figure S 2. Difference in HDX between PedH/PedF and PedH alone. Blue regions mark lower D-incorporation of PedH when in complex with PedF. Red regions mark higher D-incorporation of PedH when in complex with PedF.

Appendix

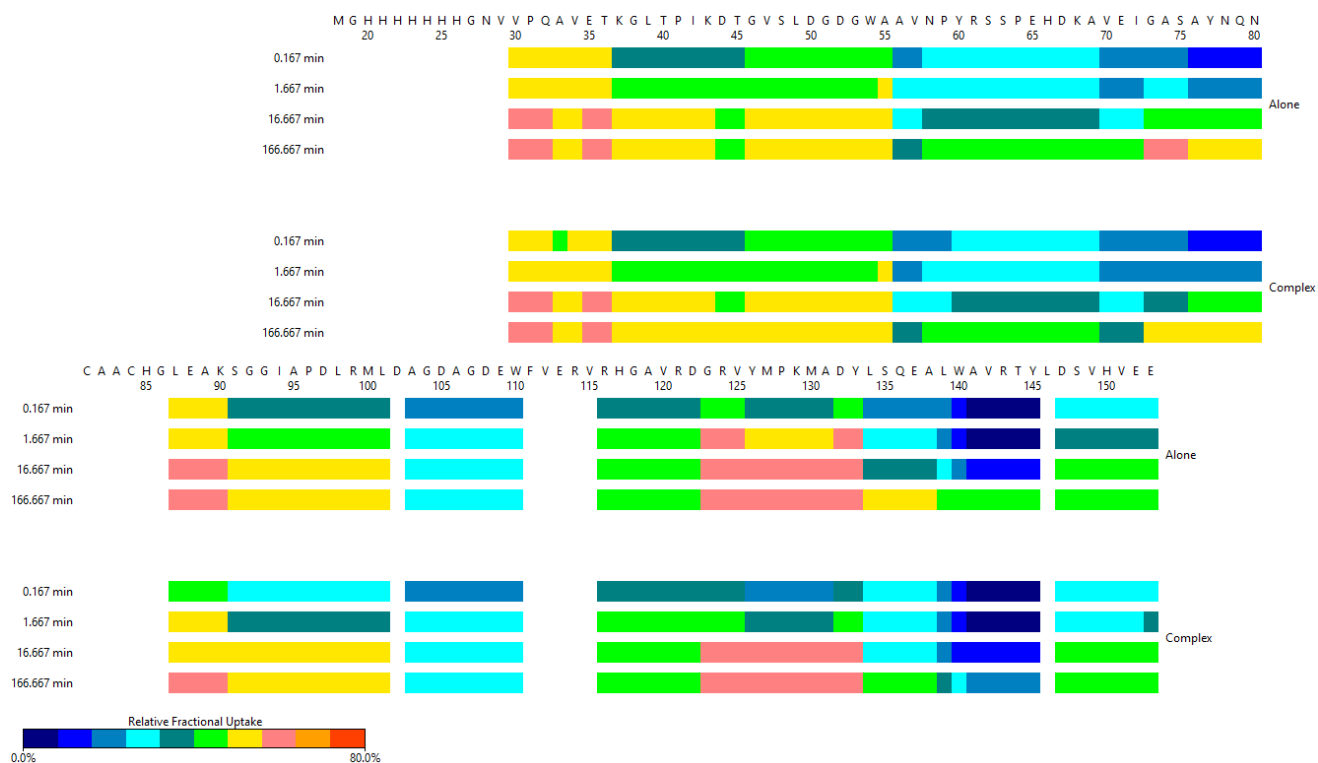


Figure S 3. Relative HDX of PedF. D-incorporation of PedF colored in rainbow from blue (0%) to red (80% D-incorporation).

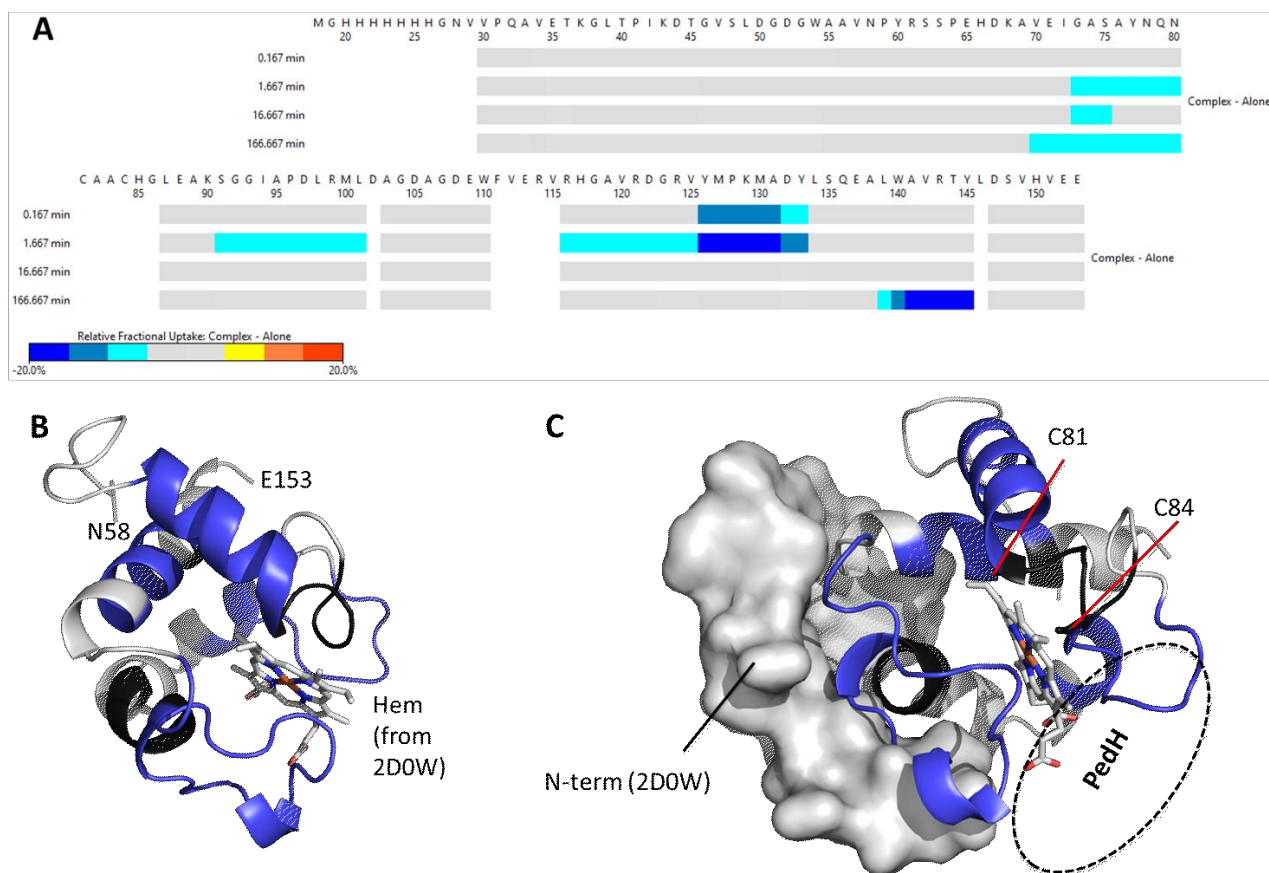


Figure S 4. Difference in HDX between PedH/PedF and PedF alone. Blue regions mark lower D-incorporation of PedF when in complex with PedH. Red regions mark higher D-incorporation of PedF when in complex with PedH.

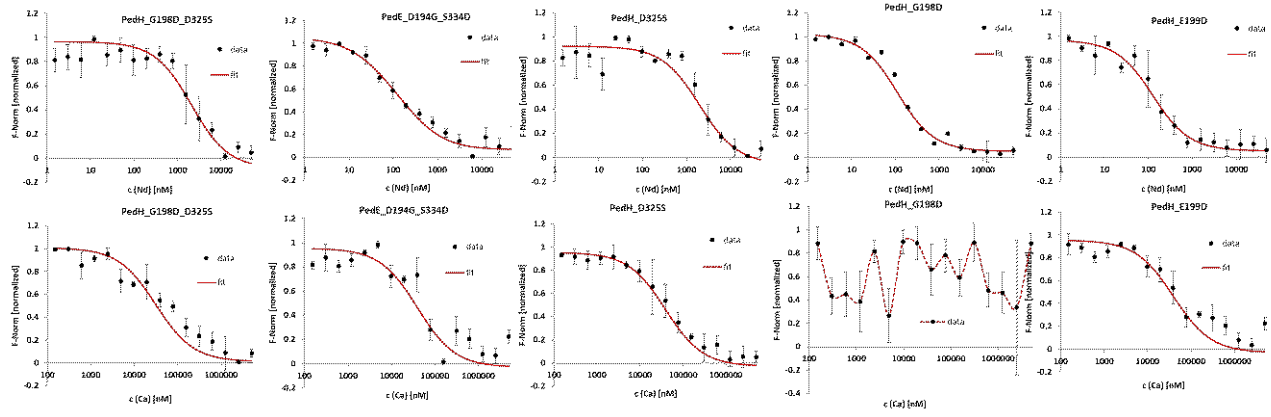


Figure S 5. Binding affinity of PedH and PedE variants towards calcium (Ca) and Neodymium (Nd) using MST. The affinity in terms of dissociation constant (K_d) values shown in figure 32 and are calculated from the MST fitted curves that plot normalized fluorescence against concentration of metal of interest.

Part II.

**Engineered PQQ-Dependent Alcohol Dehydrogenase for the oxidation
of 5-(Hydroxymethyl)furoic Acid.**

1. Scientific contribution report

This chapter represents a publication related to this thesis. An abstract as well as author contribution are given.

Title: Engineered PQQ-Dependent Alcohol Dehydrogenase for the Oxidation of 5-(Hydroxymethyl)furoic Acid

Matthias Wehrmann[#], Eslam M. Elsayed[#], Sebastian Köbbing, Laura Bendz, Alexander Lepak, Johannes Schwabe, Nick Wierckx, Gert Bange, and Janosch Klebensberger.

ACS Catalysis 2020 10 (14), 7836-7842

DOI: 10.1021/acscatal.0c01789

1.1. Abstract

Enzymatic and whole-cell biocatalysts are of immense significance for biotechnological processes, as they provide options to establish biosynthetic routes to medically and industrially relevant products using readily available bulk chemicals or renewable resources. The diverse oxidoreductases family are undoubtedly one of the most popular biocatalysts for the oxidation of alcohols. PQQ-dependent ADHs are of particular interest for various biotechnological applications, due to its high catalytic efficiency, periplasmic localization, the irreversibility of the oxidation reaction and the independence of a cofactor regeneration system.

In this publication, we have established a novel screening platform for engineering substrate specificity of PQQ-ADHs. With this platform, two active site residues

were found that are crucial for expanding the substrate specificity of PedH to 5-(hydroxymethyl)furfural (HMF) and 5-(hydroxymethyl)furoic acid (HMFA), resulting in the production of 5-formylfuroic acid. 5-Formylfuroic acid can be converted to furan-2,5-dicarboxylic acid, which is a chemical with potential to replace terephthalic acid in the production of polymers. Crystal structures of wild type and mutant enzymes show that the amino acid changes remodel the narrow substrate channel of the enzyme into a much wider one, which is not shielded by the “lid-loop”.

1.2. Author contributions.

In collaboration with 2 research groups, Dr. Janosch Klebensberger and Matthias Wehrmann from Institute of Biochemistry and Technical Biochemistry, University of Stuttgart, Germany and Prof. Dr. Nick Wierckx and Sebastian Köbbing from Institute of Bio- and Geosciences IBG-1: Biotechnology, Forschungszentrum Jülich, Germany, we aimed into a combinatorial approach of bioinformatic driven rational design, directed evolution, molecular microbiology, and biochemistry to engineer PedH from *P. putida* KT2440 to alter its substrate scope.

I was involved in molecular cloning of the genes encoded the wild type (WT) PedH and the different variants involved in the study. I have performed the expression, and purification of the proteins of interest. Furthermore, I conducted the kinetics of the enzymes towards the different substrates. Moreover, I have crystallized the WT PedH and the variant of interest. Then, I have collected, processed the datasets, modelled, and validated the crystal structures. I helped in manuscript and all graphs, as well as the main and supplementary data figures preparation.

Engineered PQQ-Dependent Alcohol Dehydrogenase for the Oxidation of 5-(Hydroxymethyl)furoic Acid

Matthias Wehrmann,[#] Eslam M. Elsayed,[#] Sebastian Köbbing, Laura Bendz, Alexander Lepak, Johannes Schwabe, Nick Wierckx, Gert Bange,* and Janosch Klebensberger*



Cite This: *ACS Catal.* 2020, 10, 7836–7842



Read Online

ACCESS |



Metrics & More



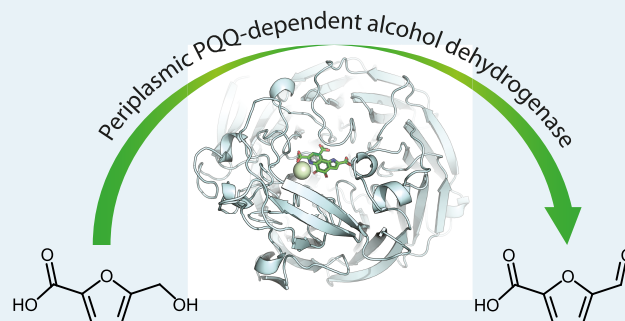
Article Recommendations



Supporting Information

ABSTRACT: Furan-2,5-dicarboxylic acid (FDCA) is a bio-based platform chemical with the potential to replace terephthalic acid in the production of polymers. A critical step for enzymatic and whole-cell production of FDCA from 5-(hydroxymethyl)furfural (HMF) is the transformation of 5-(hydroxymethyl)furoic acid (HMFA) into 5-formylfuroic acid (FFA). Here, we establish periplasmic pyrroloquinoline quinone (PQQ)-dependent alcohol dehydrogenases (ADHs) as biocatalytic tools for the oxidation of HMFA, HMF, and 5-formylfurfural (FFF). Further, we identify several amino acid residues including the “lid loop” of the substrate channel as promising targets for future engineering steps toward a fully periplasmic oxidation pathway to FDCA.

KEYWORDS: protein engineering, lanthanides, 5-(hydroxymethyl)furfural, biocatalysis, pyrroloquinoline quinone, furan-2,5-dicarboxylic acid, alcohol dehydrogenases, *Pseudomonas putida*



In 2019, worldwide plastic production was about 360 million metric tons, with over 98% of it originating from fossil carbon sources.¹ Carbon dioxide emissions from plastic production and incineration strongly contribute to global warming and climate change. Thus, transitioning toward a bio-based production of plastics based on renewable feedstock and using less energy-demanding production processes are essential steps to reach the goal of net-zero greenhouse gas emissions by 2050.²

Furan-2,5-dicarboxylic acid (FDCA) is a promising plant-derived platform chemical which could replace terephthalic acid for the production of polyethylene terephthalate and other polymers.^{3,4} FDCA can be synthesized by the oxidation of 5-(hydroxymethyl)furfural (HMF), which itself is easily accessible from lignocellulose, the most abundant biomass on earth.^{4,5} As today's chemical synthesis of FDCA typically is highly energy-demanding due to metal catalysts operating at high temperature and pressure, more sustainable routes are sought after.⁶ Consequently, various biocatalytic routes to FDCA have been presented.^{7–14} These routes start with an oxidation step of HMF, leading either to 5-(hydroxymethyl)furoic acid (HMFA) or 5-formylfurfural (FFF) followed by a second oxidation step toward 5-formylfuroic acid (FFA), before finally being oxidized into FDCA (Figure 1A). To the best of our knowledge, one of these routes that employs *Pseudomonas putida* as a biocatalyst has recently been established for industrial production.^{15–17}

In *P. putida*, as well as in many other organisms, furanic aldehydes are rapidly oxidized by native enzymes.^{18,19} In contrast, the oxidation of HMFA cannot be performed by cells of the *P. putida* wild type^{12,18,20} or other strains that have been used to produce HMFA from HMF, such as *Gluconobacter oxidans*²¹ or *Comamonas testosteroni*.²² For FDCA production, the oxidation of HMFA to FFA is crucial and requires the specific HMF oxidase HmfH. Different variants of this enzyme have been heterologously expressed in the cytoplasm of *P. putida* to enable the production of >80 g L⁻¹.^{10,12,14,18,23} However, the use of oxidases in whole-cell biotransformations is generally problematic for two reasons: (i) they require equimolar amounts of molecular oxygen as a cosubstrate, which is a limiting factor in high-density cultures,²⁴ and (ii) the associated cytoplasmic formation of equimolar amounts of cytotoxic hydrogen peroxide as a byproduct.²⁵ Although *P. putida* as a microbial catalyst has a high tolerance toward such stresses, the stress response itself is energy-demanding²⁶ and thus reduces the overall yield of the process.¹⁸

Pyrroloquinoline quinone (PQQ)-dependent alcohol dehydrogenases (ADHs) could overcome the above-mentioned

Received: April 21, 2020

Revised: June 2, 2020

Published: June 9, 2020

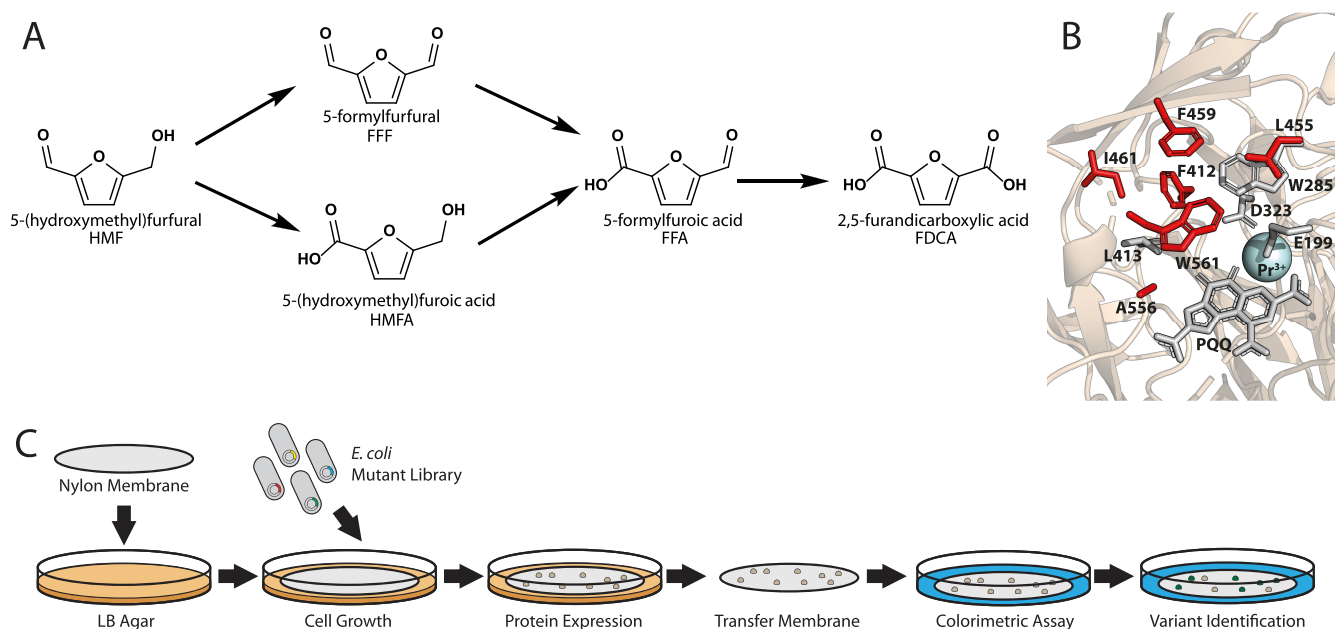


Figure 1. (A) Schematic representation of the oxidation pathways from HMF to FDCA. HMF is oxidized either at the aldehyde group to yield HMFA or at the alcohol group to yield FFF. Upon further oxidation, both routes proceed via FFA to FDCA. (B) View of the active site of PedH with PQQ cofactor as well as active site residues that were not included in mutant libraries shown as gray sticks. Residues that were selected for combinatorial random mutagenesis are depicted as red sticks. Pr^{3+} metal cofactor is displayed as blue sphere. (C) Schematic representation of a solid-phase screening assay. Nylon membranes loaded on LB agar plates were inoculated with *Escherichia coli* cells expressing PedH variants. After growth and protein production, membranes were transferred into a colored reaction solution, and colonies expressing active variants were identified by a surrounding white halo.

drawbacks as they are functional in the periplasmic space and do not form hydrogen peroxide. PQQ-ADHs are a class of enzymes that rely on calcium or lanthanide ions as well as PQQ as cofactors to oxidize a broad spectrum of alcohol and aldehyde substrates.^{27–30} They transfer the electrons derived from the oxidation reaction via *c*-type cytochromes to the cytochrome *c* oxidase complex.^{31–34} Subsequently, the cytochrome *c* oxidase efficiently uses four electrons (the equivalent of two substrate oxidation steps) to reduce one molecule of O_2 and additionally generates a source of electrochemical energy in the form of the proton motif force.³⁵ In a whole-cell process, this not only provides energy to fulfill maintenance demand³⁶ but also halves the consumption of oxygen due to the stoichiometry of this transfer. Alternatively, bioelectrochemical systems using PQQ-dependent enzymes, based on either *P. putida* cells or as isolated entities, could operate even in the absence of molecular oxygen.^{37–39} PQQ-ADHs catalyze the oxidation in an irreversible fashion, leading to unhindered accumulation of the products outside of the cells. Their periplasmic localization would avoid the rate-limiting transport across the cytoplasmic membrane and the associated need for coexpression of the *hmfT1* transporter in a whole-cell biotransformation.^{15,18} In addition, the cytoplasmic accumulation of furanic aldehydes, which are known for their strong bactericidal properties, could be reduced.^{40,41} Lastly, PQQ-ADHs can readily be engineered for increased stability at high temperatures as well as in the presence of organic solvents.⁴²

Based on these characteristics, we propose that a biocatalytic route based on PQQ-ADHs would be highly beneficial for the production of FDCA. In the present study, we describe the first and crucial step for a successful realization of such a pathway by engineering a lanthanide-dependent PQQ-ADH from *P.*

putida KT2440 (PedH) for oxidation of the pathway intermediates HMF, FFF, and HMFA (Figure 1A).

Initial experiments demonstrated that purified PedH exhibits no enzymatic activity toward HMFA (data not shown). However, marginal activity with HMF ($0.13 \pm 0.02 \text{ U mg}^{-1}$) was observed. In order to expand the substrate specificity toward the oxidation of HMFA to FFA—a key reaction within the biocatalytic route toward FDCA production—a set of 12 small focused mutant libraries was generated (Figure 1B and Table S1). Each mutant library consisted of a pair of NNK-randomized active site positions in order to increase the chances of identifying potentially synergistic combinations of mutations.⁴³ To minimize the creation of inactive variants, no active site residues that are directly involved in the catalytic mechanism were included.⁴⁴ To further reduce the screening effort, two additional constraints based on structure–sequence relationships were applied. These were derived from a 3DM database consisting of >1300 sequences of PQQ-ADHs that show structural similarity to PedH.⁴⁵ First, no positions of low sequence variability in the 3DM database were included. Second, only residues with a high correlation score in the 3DM database (Table S2), meaning that two positions show a high degree of natural coevolution,⁴⁶ were chosen for combinatorial NNK mutagenesis.

To screen these combinatorial libraries, we developed a colony screen, based on a previously established whole-cell assay (Figure 1C).⁴² For this, *E. coli* cells transformed with the combinatorial libraries grew on nylon membranes placed on LB agar plates. The transfer of the membrane onto rhamnose-containing LB agar subsequently induced plasmid-borne protein production. After incubation of the membranes in a colorimetric assay solution, colonies with enzymatic activity toward HMFA were identified by a white halo (Figure 1C).

In the initial screening, more than 30,000 clones were tested, and 15 clones showing apparent enzymatic activity toward HMFA were identified. Re-evaluation of the novel enzymatic activity and subsequent sequencing revealed three different variants with activity toward HMFA, namely, PedH^{F412I/W561S}, PedH^{F412V/W561A}, and PedH^{F412I/W561Q} (Table 1). To exclude

Table 1. Specific Enzyme Activities with HMFA^a

variant	specific activity (U mg ⁻¹)
PedH	nd
F412I/W561S	0.12 ± 0.02
F412I/W561Q	0.35 ± 0.01
F412V/W561A	1.04 ± 0.05

^aActivities were determined with purified enzymes and 10 mM HMFA as substrate. Values represent the average of three individual measurements with corresponding standard deviation. Activities below detection limit are indicated (nd).

potential host-specific effects, activities for all variants were evaluated using enzymes purified by affinity chromatography (IMAC). The variants PedH^{F412I/W561S} and PedH^{F412I/W561Q} showed a specific activity with HMFA of 0.12 ± 0.02 and 0.35 ± 0.01 U mg⁻¹, respectively. PedH^{F412V/W561A} exhibited by far the highest specific activity of 1.04 ± 0.05 U mg⁻¹. Notably, all variants are combinatorial mutants derived from the same mutant library PedH^{F412X/W561X}, suggesting that a single-point mutation at position F412 or W561 is not sufficient to alter the substrate specificity toward HMFA.

To identify the reaction product, biotransformations using purified enzymes and the artificial electron mediator/terminal acceptor pair, PMS/DCPIP, were performed (Table 2).

Table 2. Biotransformations of HMFA^a

time (h)	FFA (mM)		
	control	PedH	PedH ^{F412V/W561A}
0	nd	nd	0.28 ± 0.01
1	nd	nd	1.24 ± 0.15
24	nd	nd	1.40 ± 0.11

^aBiotransformations were performed with purified enzymes or enzyme-free control and PMS/DCPIP as an artificial electron acceptor pair. Samples were taken at several time points after substrate addition. Values represent the average of two individual measurements with corresponding standard deviation. Enzymatic reaction without detectable product formation is indicated (nd).

Whereas no product formation was detected with PedH or in control experiments without enzyme addition, FFA was identified as the single reaction product (1.40 ± 0.11 mM in 24 h) in conversions using PedH^{F412V/W561A}. Further oxidation to FDCA was not detected.

To verify the screening results and gain mechanistic insights, we purified PedH and its F412V/W561A variant using His affinity followed by size-exclusion chromatography. Kinetic parameters of PedH and PedH^{F412V/W561A} were derived from specific activities determined under a slightly modified protocol compared to the initial screens to reach saturating substrate concentrations (≥50 mM HMFA). Under these conditions, the kinetic values of PedH^{F412V/W561A} with HMFA (Figure 2E,G) were similar to those of previously characterized proteins with activity toward HMFA, namely, the 5-(hydroxymethyl)furfural oxidase HmfO of *Methylovorus* sp.

strain MP688 ($k_{\text{cat}} = 8.5 \text{ s}^{-1}$, $K_{\text{M}} = 73 \text{ mM}$, $k_{\text{cat}}/K_{\text{M}} = 0.12 \text{ mM}^{-1} \text{ s}^{-1}$) and the aryl alcohol oxidase AAO of *Pleurotus eryngii* ($k_{\text{cat}} = \text{nd}$, $K_{\text{M}} = \text{nd}$, $k_{\text{cat}}/K_{\text{M}} = 0.017 \pm 0.002 \text{ mM}^{-1} \text{ s}^{-1}$).^{8,47}

Consistent with our initial observations, PedH showed no activity with HMFA (Figure 2E). Additionally, both PedH and PedH^{F412V/W561A} oxidized ethanol (Figure 2A,B). However, PedH^{F412V/W561A} exhibited a K_{M} value approximately 525-fold higher than that of PedH, whereas the maximal velocity appeared to be unchanged (Figure 2F,G). This suggests that the oxidative capability of the PedH^{F412V/W561A} variant is unaffected by the amino acid changes, and only the substrate binding is modulated.

In addition to HMFA, PedH^{F412V/W561A} also oxidized HMF and FFF. In comparison to HMFA, the turnover numbers with HMF and FFF as substrates were about 4-fold and 3-fold higher, respectively (Figure 2C–E,G). Notably, the PedH wild type enzyme showed no activity with FFF. In contrast to our initial findings, PedH also displayed no activity with HMF as the substrate. This discrepancy can most likely be explained by the change of the enzymatic assay conditions, which caused overall lower specific activities compared to the initial screening conditions. Enzymatic assays with PedH^{F412V/W561A} confirmed that FFA does not serve as a substrate under these conditions as, even with substrate concentrations as high as 100 mM, no enzyme activity could be detected. This sheds new light on the previously perceived importance of PQQ-ADHs in HMF oxidation to FDCA.¹⁸

Taken together, these findings show that the PedH^{F412V/W561A} variant is capable of oxidizing not only HMFA but also HMF and FFF, whereas it is not able to oxidize FFA. Aldehyde oxidation by PQQ-ADHs is believed to proceed via the hydrated aldehyde, and the stability and/or formation of these *gem*-diols is therefore crucial for activity.⁴⁴

The degree of hydration of the aldehyde group of FFA in aqueous solution is dramatically lower in comparison to that of FFF.^{7,48} Additionally, the carboxylic group of HMFA negatively influences the substrate affinity. The lack of activity toward FFA can therefore most likely be explained by a combination of the low effective concentration of the *gem*-diol substrate and the reduced substrate affinity of the variant toward carboxylated furan compounds. Future engineering efforts would consequently need to improve substrate binding to enable the conversion of this furan aldehyde.

To determine the molecular basis of these findings, we determined the structures of PedH and PedH^{F412V/W561A} bound to PQQ and praseodymium to resolutions of 1.7 and 1.6 Å, respectively (Table S3). The crystal structures show the typical beta propeller fold consisting of eight four-stranded β-blades (W1–W8) as the core structural element with three additional strands inserted after W5 (named “roof sheet”) (Figure 3A). Two small α-helices are inserted between the strands B and C of W8 (named “lid loop”). The active site containing the PQQ cofactor and the praseodymium ion localizes in a hydrophobic cradle close to the surface of the β-propeller. Here, PQQ is coordinated by Q87, I135, R137, S181, R350, L413, N417, W418, and W493 (Figure S1A). The side chains of W263 and the vicinal disulfide bond between C131 and C132 provide additional stacking interactions with PQQ (Figure S1B). The praseodymium ion coordination is highly conserved and achieved by the amino acid side chains of E199, N281, D323, and D325 and the O5 and O7A atoms of the PQQ cofactor (Figure S1A). Structural comparison of PedH and

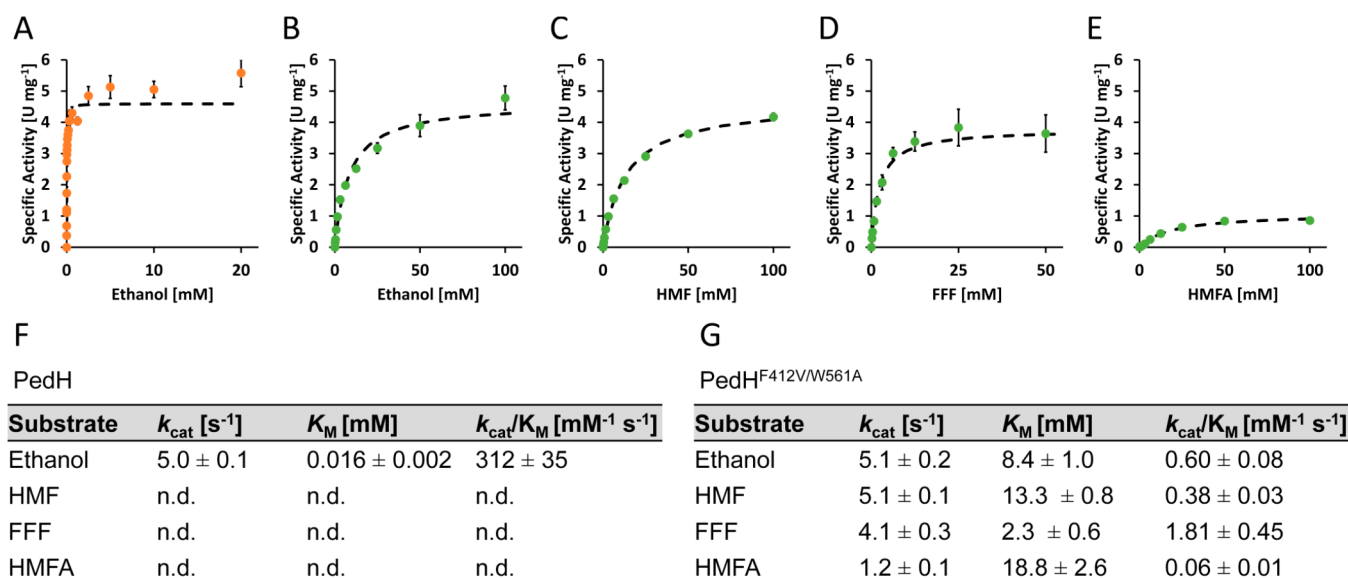


Figure 2. Kinetic parameter determination. (A–E) Michaelis–Menten plot showing the specific enzyme activities of PedH wild type (A) and PedH^{F412V/W561A} variant (B–E) with different concentrations of ethanol (A,B), HMF (C), FFF (D), or HMFA (E). Kinetic parameters of PedH (F) and PedH^{F412V/W561A} (G) derived by fitting specific enzyme activities at different substrates to the Michaelis–Menten model of single-substrate enzyme kinetics.

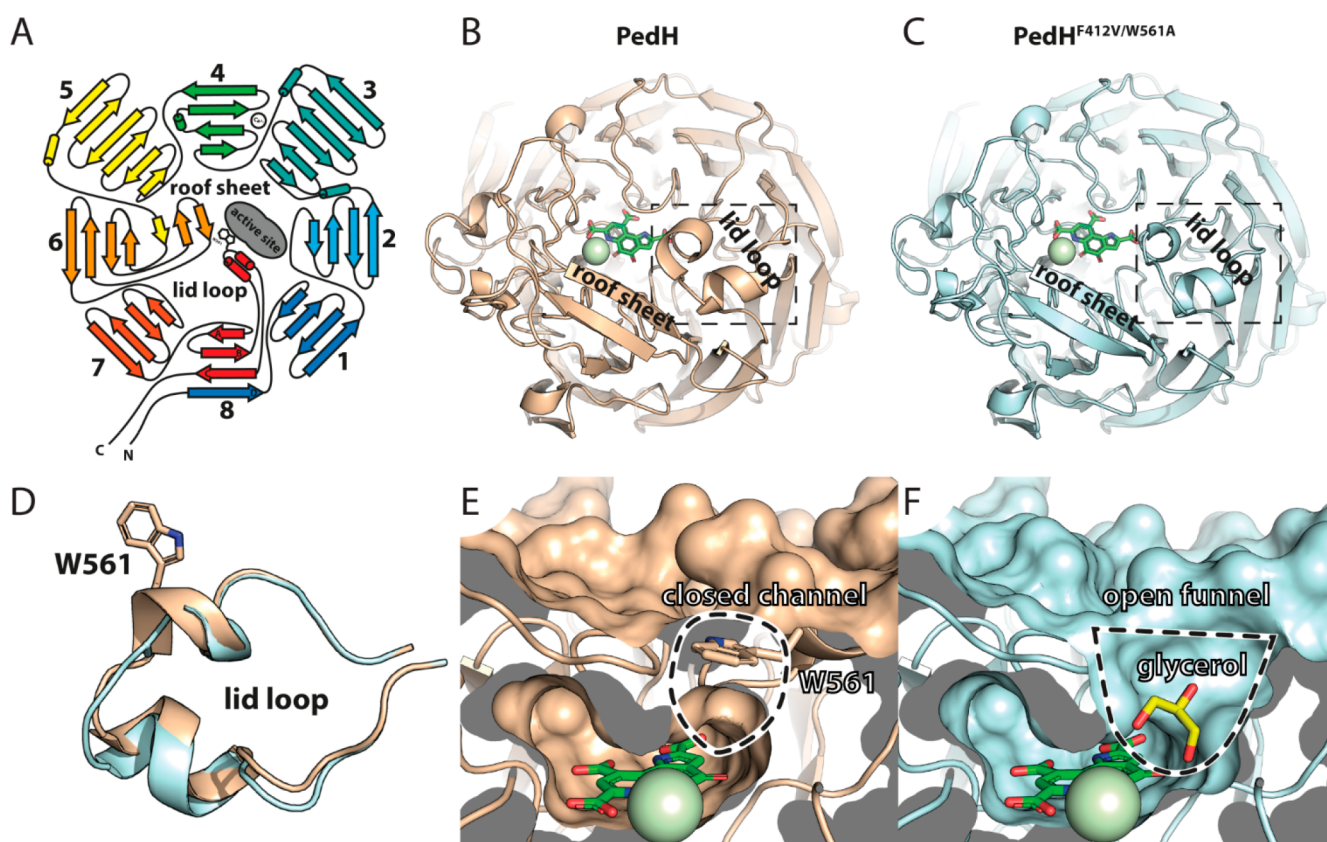


Figure 3. (A) Schematic representation of the β -propeller and position of the active site. Top view of PedH wild type (B) and PedH^{F412V/W561A} (C), showing the position of the roof sheet and the lid loop. (D) Overlay of the lid loop in PedH wild type (wheat) and PedH^{F412V/W561A} (blue) and relative position of W561. Cut-away of the active site in PedH wild type (E) and PedH^{F412V/W561A} variant (F). Glycerol as the substrate mimic in the active site of the PedH^{F412V/W561A} variant is depicted in yellow.

PedH^{F412V/W561A} shows that neither the PQQ nor the metal binding environment is changed. However, our comparison also shows significant differences between both structures (Figure 3B,C). Access to the PQQ/praseodymium-containing

active site is provided through a substrate channel of about 4 Å in diameter (lined by F412 and L413) and a length of 9 Å (shortest distance from the metal ion to the PedH surface). In PedH, W561 within the “lid loop” restricts this substrate

channel reminiscent of a diaphragm and hampers the entrance of bulkier substrates. In PedH^{F412V/W561A}, W561 is replaced by alanine, which leads to an opening of the substrate channel. In PedH, F412 lines the inner surface of the substrate channel and serves to position the “lid loop” relative to the center of the substrate channel (Figure 3D–F). In the structure of PedH^{F412V/W561A}, the replacement of F412 with the “smaller” valine not only widens the substrate channel at its bottom but also leads to a remodeling and repositioning of the “lid loop”, including the amino acid positions 559–566 effectively moving the loop backbone about 2.5 Å away from the channel entrance (Figure 3B–D).

In summary, our structural analysis shows that the amino acid changes remodel the narrow substrate channel of PedH into a much wider one in PedH^{F412V/W561A}, which is not shielded from substrate entry by the “lid loop”. In accordance with these structural changes, we found electron density for a glycerol in the active site of PedH^{F412V/W561A}. This molecule might illustrate how the similarly sized HMFA, HMF, and FFF easily pass through the widened channel in PedH^{F412V/W561A} compared to the impeded access in the PedH enzyme (compare Figures 3E,F and S2A). These observations are consistent with the increased activities of PedH^{F412V/W561A} toward HMF and the newly gained activity toward HMFA as well as FFF and further explain the massively increased K_M value of PedH^{F412V/W561A} for ethanol. Additionally, an overlay of the glycerol molecule with HMFA indicates that in an active binding conformation the apolar residue L560 of the lid loop as well as L455 and the phenol rings of W285 and F459 point toward the negatively charged carboxyl group of HMFA (Figure S2B). This might not only explain the decreased K_M of PedH^{F412V/W561A} for HMFA in comparison with the uncharged HMF or FFF but also reveals promising targets for the engineering of FFA activity.

In conclusion, our work established a novel screening platform for engineered PQQ-ADHs. With this platform, two active site residues that are crucial to expand the substrate scope of PedH toward HMFA were found. The best double mutant exhibited activities similar to those of known HMFA oxidizing enzymes and could serve as an alternative to currently employed oxidases. Structural analysis of the variant revealed significant changes to the geometry and composition of several active site and substrate channel features. In addition, we identified several amino acid residues—including one in the “lid loop”—as attractive targets for further optimizing activity toward carboxylated furanic compounds, such as FFA. With these, a whole-cell biocatalyst with a completely periplasmic production route from HMF to FDCA can be envisioned. Such a route would avoid the intracellular formation of toxic byproducts or intermediates such as hydrogen peroxide and furanic aldehydes. Consequently, the stress-associated maintenance for the cell would be reduced, while electrons from the oxidation reaction would be efficiently channeled into the cellular energy metabolism, allowing the efficient production of FDCA. In general, our study shows that PQQ-dependent ADH enzymes can be engineered into useful tools for biocatalysis and paves the way for their application in bio-based plastic production.

■ ASSOCIATED CONTENT

SI Supporting Information

The Supporting Information is available free of charge at <https://pubs.acs.org/doi/10.1021/acscatal.0c01789>.

Experimental details; mutant library composition; correlated mutation analysis; crystallographic data collection and refinement statistics; structure of PQQ coordination in the active site of PedH; cutaway of the active site of PedH^{F412V/W561A} with HMFA superimposed onto glycerol (PDF)

Accession Codes

Coordinates and structure factors have been deposited at the Protein Data Bank (PDB) under the accession codes: 6ZCW (wild type PedH) and 6ZCV (PedH^{F412V/W561A}).

■ AUTHOR INFORMATION

Corresponding Authors

Gert Bange – SYNMIKRO Research Center and Department of Chemistry, Philipps-University Marburg, 35043 Marburg, Germany; Email: gert.bange@synmikro.uni-marburg.de

Janosch Klebensberger – Institute of Biochemistry and Technical Biochemistry, University of Stuttgart, 70569 Stuttgart, Germany; orcid.org/0000-0003-2740-3769; Email: janosch.klebensberger@itb.uni-stuttgart.de

Authors

Matthias Wehrmann – Institute of Biochemistry and Technical Biochemistry, University of Stuttgart, 70569 Stuttgart, Germany

Eslam M. Elsayed – SYNMIKRO Research Center and Department of Chemistry, Philipps-University Marburg, 35043 Marburg, Germany; Department of Microbiology and Immunology, Faculty of Pharmacy, Zagazig University, 44519 Zagazig, Egypt

Sebastian Köbbing – Institute of Applied Microbiology-iAMB, RWTH Aachen University, 52074 Aachen, Germany; orcid.org/0000-0002-4606-4961

Laura Bendz – Institute of Biochemistry and Technical Biochemistry, University of Stuttgart, 70569 Stuttgart, Germany

Alexander Lepak – SYNMIKRO Research Center and Department of Chemistry, Philipps-University Marburg, 35043 Marburg, Germany; Max Planck Institute for Terrestrial Microbiology, 35043 Marburg, Germany

Johannes Schwabe – SYNMIKRO Research Center and Department of Chemistry, Philipps-University Marburg, 35043 Marburg, Germany

Nick Wierckx – Institute of Applied Microbiology-iAMB, RWTH Aachen University, 52074 Aachen, Germany; Institute of Bio- and Geosciences IBG-1: Biotechnology, Forschungszentrum Jülich, 52425 Jülich, Germany

Complete contact information is available at: <https://pubs.acs.org/10.1021/acscatal.0c01789>

Author Contributions

[#]M.W. and E.M.E. contributed equally to this work. J.K. and M.W. conceptualized the work and wrote the original draft of the manuscript. All authors contributed to writing, reviewing, and editing of the manuscript as well as data analysis and visualization. J.K. and G.B. acquired the financial support for the project, and J.K., G.B., and N.W. supervised the work. M.W., E.M.E., S.K., L.B., A.L., and J.S. conducted the research.

Funding

The work of M.W. and J.K. was supported by an individual research grant from the Deutsche Forschungsgemeinschaft (KL 2340/2-1). We thank the Jameel Education Foundation Scholarship Fund Programme for the financial support of E.M.E. S.K. acknowledges funding from the European Union's

Horizon 2020 Research and Innovation Programme under Grant Agreement No. 633962 for the project P4SB. N.W. acknowledges funding from the German Federal Ministry of Education and Research (BMBF, FKZ 031B0852A).

Notes

The authors declare no competing financial interest.

ACKNOWLEDGMENTS

We thank the LOEWE initiative of the state of Hesse for excellent support (to G.B.). We acknowledge beamline support from the Deutsche Elektronen Synchrotron (DESY, Hamburg). We kindly acknowledge Harald Ruijsenaars (Corbion Biochem BV) for providing analytical standards of HMF derivatives, and Bernhard Hauer and Lars M. Blank for their continuous support.

ABBREVIATIONS

PQQ, pyrroloquinoline quinone; PQQ-ADH, pyrroloquinoline quinone dependent alcohol dehydrogenase; REE, rare earth element; FDCA, furan-2,5-dicarboxylic acid; HMFA, 5-(hydroxymethyl)furoic acid; FFF, 5-(formyl)furfural; HMF, 5-(hydroxymethyl)furfural; FFA, 5-formylfuroic acid

REFERENCES

- (1) European Bioplastics. www.european-bioplastics.org (accessed 2020-04-02).
- (2) European Parliament [Press Release]. The European Parliament Declares Climate Emergency. <https://www.europarl.europa.eu/news/en/press-room/20191121IPR67110/the-european-parliament-declares-climate-emergency> (accessed 2019-11-29).
- (3) Werpy, T.; Petersen, G. *Top Value Added Chemicals from Biomass: Vol. I—Results of Screening for Potential Candidates from Sugars and Synthesis Gas*; U.S. Department of Energy: Golden, CO, 2004; Vol. II.
- (4) Yuan, H.; Liu, H.; Du, J.; Liu, K.; Wang, T.; Liu, L. Biocatalytic Production of 2,5-Furandicarboxylic Acid: Recent Advances and Future Perspectives. *Appl. Microbiol. Biotechnol.* **2020**, *104* (2), 527–543.
- (5) Rosatella, A. A.; Simeonov, S. P.; Frade, R. F. M.; Afonso, C. A. M. 5-Hydroxymethylfurfural (HMF) as a Building Block Platform: Biological Properties, Synthesis and Synthetic Applications. *Green Chem.* **2011**, *13* (4), 754–793.
- (6) Delidovich, I.; Hausoul, P. J. C.; Deng, L.; Pfützenreuter, R.; Rose, M.; Palkovits, R. Alternative Monomers Based on Lignocellulose and Their Use for Polymer Production. *Chem. Rev.* **2016**, *116* (3), 1540–1599.
- (7) Dijkman, W. P.; Groothuis, D. E.; Fraaije, M. W. Enzyme-Catalyzed Oxidation of 5-Hydroxymethylfurfural to Furan-2,5-Dicarboxylic Acid. *Angew. Chem., Int. Ed.* **2014**, *53* (25), 6515–6518.
- (8) Carro, J.; Ferreira, P.; Rodríguez, L.; Prieto, A.; Serrano, A.; Balcells, B.; Ardá, A.; Jiménez-Barbero, J.; Gutiérrez, A.; Ullrich, R.; Hofrichter, M.; Martínez, A. T. 5-Hydroxymethylfurfural Conversion By Fungal Aryl-Alcohol Oxidase and Unspecific Peroxygenase. *FEBS J.* **2015**, *282* (16), 3218–3229.
- (9) McKenna, S. M.; Leimkühler, S.; Herter, S.; Turner, N. J.; Carnell, A. J. Enzyme Cascade Reactions: Synthesis of Furandicarboxylic Acid (FDCA) and Carboxylic Acids Using Oxidases in Tandem. *Green Chem.* **2015**, *17* (6), 3271–3275.
- (10) Koopman, F.; Wierckx, N.; de Winde, J. H.; Ruijsenaars, H. J. Efficient Whole-Cell Biotransformation of 5-(Hydroxymethyl)-Furfural into FDCA, 2,5-Furandicarboxylic Acid. *Bioresour. Technol.* **2010**, *101* (16), 6291–6296.
- (11) Yuan, H.; Li, J.; Shin, H.-d.; Du, G.; Chen, J.; Shi, Z.; Liu, L. Improved Production of 2,5-Furandicarboxylic Acid by Over-expression of 5-Hydroxymethylfurfural Oxidase and 5-Hydroxyme-thylfurfural/Furfural Oxidoreductase in *Raoultella Ornithinolytica* BF60. *Bioresour. Technol.* **2018**, *247*, 1184–1188.
- (12) Hsu, C.-T.; Kuo, Y.-C.; Liu, Y.-C.; Tsai, S.-L. Green Conversion of 5-Hydroxymethylfurfural to Furan-2,5-Dicarboxylic Acid by Heterogeneous Expression of 5-Hydroxymethylfurfural Oxidase in *Pseudomonas putida* S12. *Microb. Biotechnol.* **2020**, DOI: 10.1111/1751-7915.13564.
- (13) Dijkman, W. P.; Binda, C.; Fraaije, M. W.; Mattevi, A. Structure-Based Enzyme Tailoring of 5-Hydroxymethylfurfural Oxidase. *ACS Catal.* **2015**, *5* (3), 1833–1839.
- (14) Pham, N. N.; Chen, C.; Li, H.; Nguyen, M. T. T.; Nguyen, P. K. P.; Tsai, S.; Chou, J.; Ramli, T. C.; Hu, Y. Engineering Stable *Pseudomonas putida* S12 by CRISPR for 2,5-Furandicarboxylic Acid (FDCA) Production. *ACS Synth. Biol.* **2020**, *9* (5), 1138–1149.
- (15) Wierckx, N.; Elink Schuurman, T. D.; Kuijper, S.; Ruijsenaars, H. J. Genetically Modified Cell and Process for Use of Said Cell. Patent Appl. WO 2012064195 A2, 2012.
- (16) Ruijsenaars, H. J.; Wierckx, N.; Koopman, F.; Straathof, A.; De Winde, J. H. Polypeptides Having Oxidoreductase Activity And Their Uses. Patent Appl. WO 2011026913, 2010.
- (17) Sajid, M.; Zhao, X.; Liu, D. Production of 2,5-Furandicarboxylic Acid (FDCA) from 5-Hydroxymethylfurfural (HMF): Recent Progress Focusing on the Chemical-Catalytic Routes. *Green Chem.* **2018**, *20* (24), 5427–5453.
- (18) Wierckx, N.; Elink Schuurman, T. D.; Blank, L. M.; Ruijsenaars, H. J. Whole-Cell Biocatalytic Production of 2,5-Furandicarboxylic Acid. In *Molecular Microbiology*; Kamm, B., Ed.; Microbiology Monographs; Springer: Berlin, 2015; Vol. 26, pp 207–223.
- (19) Hu, L.; He, A.; Liu, X.; Xia, J.; Xu, J.; Zhou, S.; Xu, J. Biocatalytic Transformation of 5-Hydroxymethylfurfural into High-Value Derivatives: Recent Advances and Future Aspects. *ACS Sustainable Chem. Eng.* **2018**, *6* (12), 15915–15935.
- (20) Xu, Q.; Zheng, Z.; Zou, L.; Zhang, C.; Yang, F.; Zhou, K.; Ouyang, J. A Versatile *Pseudomonas putida* KT2440 with New Ability: Selective Oxidation of 5-Hydroxymethylfurfural to 5-Hydroxymethyl-2-Furancarboxylic Acid. *Bioprocess Biosyst. Eng.* **2020**, *43* (1), 67–73.
- (21) Sayed, M.; Pyo, S.-H.; Rehnberg, N.; Hatti-Kaul, R. Selective Oxidation of 5-Hydroxymethylfurfural to 5-Hydroxymethyl-2-Furancarboxylic Acid Using *Gluconobacter oxydans*. *ACS Sustainable Chem. Eng.* **2019**, *7* (4), 4406–4413.
- (22) Zhang, X. Y.; Zong, M. H.; Li, N. Whole-Cell Biocatalytic Selective Oxidation of 5-Hydroxymethylfurfural to 5-Hydroxymethyl-2-Furancarboxylic Acid. *Green Chem.* **2017**, *19* (19), 4544–4551.
- (23) Koopman, F.; Wierckx, N.; De Winde, J. H.; Ruijsenaars, H. J. Identification and Characterization of the Furfural and 5-(Hydroxymethyl)Furfural Degradation Pathways of *Cupriavidus basilensis* HMF14. *Proc. Natl. Acad. Sci. U. S. A.* **2010**, *107* (11), 4919–4924.
- (24) Baldwin, C. V. F.; Woodley, J. On Oxygen Limitation in a Whole Cell Biocatalytic Baeyer–Villiger Oxidation Process. *Biotechnol. Bioeng.* **2006**, *95* (3), 362–369.
- (25) Linley, E.; Denyer, S. P.; McDonnell, G.; Simons, C.; Maillard, J.-Y. Use of Hydrogen Peroxide as a Biocide: New Consideration of Its Mechanisms of Biocidal Action. *J. Antimicrob. Chemother.* **2012**, *67* (7), 1589–1596.
- (26) Kim, J.; Park, W. Oxidative Stress Response in *Pseudomonas putida*. *Appl. Microbiol. Biotechnol.* **2014**, *98* (16), 6933–6946.
- (27) Keltjens, J. T.; Pol, A.; Reimann, J.; Op den Camp, H. J. M. PQQ-Dependent Methanol Dehydrogenases: Rare-Earth Elements Make a Difference. *Appl. Microbiol. Biotechnol.* **2014**, *98* (14), 6163–6183.
- (28) Wehrmann, M.; Billard, P.; Martin-Meriadec, A.; Zegeye, A.; Klebensberger, J. Functional Role of Lanthanides in Enzymatic Activity and Transcriptional Regulation of Pyrroloquinoline Quinone-Dependent Alcohol Dehydrogenases in *Pseudomonas putida* KT2440. *mBio* **2017**, *8* (3), e00570.
- (29) Good, N. M.; Vu, H. N.; Suriano, C. J.; Subuyuj, G. A.; Skovran, E.; Martinez-Gomez, N. C. Pyrroloquinoline Quinone

Ethanol Dehydrogenase in *Methylobacterium extorquens* AM1 Extends Lanthanide-Dependent Metabolism to Multicarbon Substrates. *J. Bacteriol.* **2016**, *198* (22), 3109–3118.

(30) Jahn, B.; Pol, A.; Lumpe, H.; Barends, T. R. M.; Dietl, A.; Hogendoorn, C.; Op den Camp, H. J. M.; Daumann, L. Similar but Not the Same: First Kinetic and Structural Analyses of a Methanol Dehydrogenase Containing a Europium Ion in the Active Site. *ChemBioChem* **2018**, *19* (11), 1147–1153.

(31) Zheng, Y.; Huang, J.; Zhao, F.; Chistoserdova, L. Physiological Effect of XoxG(4) on Lanthanide-Dependent Methanotrophy. *mBio* **2018**, *9* (2), e02430-17.

(32) Versantvoort, W.; Pol, A.; Daumann, L. J.; Larrabee, J. A.; Strayer, A. H.; Jetten, M. S. M.; van Niftrik, L.; Reimann, J.; Op den Camp, H. J. M. Characterization of a Novel Cytochrome c as the Electron Acceptor of XoxF-MDH in the Thermoacidophilic Methanotroph *Methylacidiphilum Fumariolicum* SolV. *Biochim. Biophys. Acta, Proteins Proteomics* **2019**, *1867* (6), 595–603.

(33) Schobert, M.; Görisch, H. Cytochrome C550 Is an Essential Component of the Quinoprotein Ethanol Oxidation System in *Pseudomonas aeruginosa*: Cloning and Sequencing of the Genes Encoding Cytochrome C550 and an Adjacent Acetaldehyde Dehydrogenase. *Microbiology* **1999**, *145* (2), 471–481.

(34) Goodwin, P. M.; Anthony, C. The Biochemistry, Physiology and Genetics of PQQ and PQQ-Containing Enzymes. *Advances in Microbial Physiology*; Elsevier: Amsterdam, 1998; Vol. 40, pp 1–80.

(35) García-Horsman, J. A.; Barquera, B.; Rumbley, J.; Ma, J.; Gennis, R. B. The Superfamily of Heme-Copper Respiratory Oxidases. *J. Bacteriol.* **1994**, *176* (18), 5587–5600.

(36) Hardy, G. Energy Conservation by Pyrroloquinoline Quinol-Linked Xylose Oxidation in *Pseudomonas putida* NCTC 10936 during Carbon-Limited Growth in Chemostat Culture. *FEMS Microbiol. Lett.* **1993**, *107* (1), 107–110.

(37) Yu, S.; Lai, B.; Plan, M. R.; Hodson, M. P.; Lestari, E. A.; Song, H.; Krömer, J. Improved Performance of *Pseudomonas putida* in a Bioelectrochemical System through Overexpression of Periplasmic Glucose Dehydrogenase. *Biotechnol. Bioeng.* **2018**, *115* (1), 145–155.

(38) Lai, B.; Yu, S.; Bernhardt, P. V.; Rabaey, K.; Viridis, B.; Krömer, J. Anoxic Metabolism and Biochemical Production in *Pseudomonas putida* F1 Driven by a Bioelectrochemical System. *Biotechnol. Biofuels* **2016**, *9* (1), 39.

(39) Takeda, K.; Matsumura, H.; Ishida, T.; Samejima, M.; Igarashi, K.; Nakamura, N.; Ohno, H. The Two-Step Electrochemical Oxidation of Alcohols Using a Novel Recombinant PQQ Alcohol Dehydrogenase as a Catalyst for a Bioanode. *Bioelectrochemistry* **2013**, *94*, 75–78.

(40) Heer, D.; Sauer, U. Identification of Furfural as a Key Toxin in Lignocellulosic Hydrolysates and Evolution of a Tolerant Yeast Strain. *Microb. Biotechnol.* **2008**, *1* (6), 497–506.

(41) Zaldivar, J.; Martinez, A.; Ingram, L. O. Effect of Selected Aldehydes on the Growth and Fermentation of Ethanologenic *Escherichia coli*. *Biotechnol. Bioeng.* **1999**, *65* (1), 24–33.

(42) Wehrmann, M.; Klebensberger, J. Engineering Thermal Stability and Solvent Tolerance of the Soluble Quinoprotein PedE from *Pseudomonas putida* KT2440 with a Heterologous Whole-Cell Screening Approach. *Microb. Biotechnol.* **2018**, *11* (2), 399–408.

(43) Reetz, M. T.; Bocola, M.; Carballeira, J. D.; Zha, D.; Vogel, A. Expanding the Range of Substrate Acceptance of Enzymes: Combinatorial Active-Site Saturation Test. *Angew. Chem., Int. Ed.* **2005**, *44* (27), 4192–4196.

(44) Oubrie, A.; Rozeboom, H. J.; Kalk, K. H.; Huizinga, E. G.; Dijkstra, B. W. Crystal Structure of Quinohemoprotein Alcohol Dehydrogenase from *Comamonas testosteroni*: Structural Basis for Substrate Oxidation and Electron Transfer. *J. Biol. Chem.* **2002**, *277* (5), 3727–3732.

(45) Kuipers, R.; Joosten, H. J.; van Berkel, W. J. H.; Leferink, N. G. H.; Rooijen, E.; Ittmann, E.; van Zimmeren, F.; Jochens, H.; Bornscheuer, U.; Vriend, G.; Martins dos Santos, V. A. P.; Schaap, P. J. 3DM: Systematic Analysis of Heterogeneous Superfamily Data to

Discover Protein Functionalities. *Proteins: Struct., Funct., Genet.* **2010**, *78* (9), 2101–2113.

(46) Kuipers, R.; Joosten, H. J.; Verwiël, E.; Paans, S.; Akerboom, J.; Van Der Oost, J.; Leferink, N. G. H.; Van Berkel, W. J. H.; Vriend, G.; Schaap, P. J. Correlated Mutation Analyses on Super-Family Alignments Reveal Functionally Important Residues. *Proteins: Struct., Funct., Genet.* **2009**, *76* (3), 608–616.

(47) Dijkman, W. P.; Fraaije, M. W. Discovery and Characterization of a 5-Hydroxymethylfurfural Oxidase from *Methylovoros* Sp. Strain MP688. *Appl. Environ. Microbiol.* **2014**, *80* (3), 1082–1090.

(48) Bell, R. P. The Reversible Hydration of Carbonyl Compounds. *Advances in Physical Organic Chemistry Volume 4*; Elsevier: Amsterdam, 1966; Vol. 60, pp 1–29.

Supporting Information

An Engineered PQQ-Dependent Alcohol Dehydrogenase for the Oxidation of 5-(Hydroxymethyl)furoic Acid

Matthias Wehrmann^{af}, Eslam M. Elsayed^{bt}, Sebastian Köbbing^c, Laura Bendz^a,
Alexander Lepak^{b,d}, Johannes Schwabe^b, Nick Wierckx^{c,e}, Gert Bange^{b*}, Janosch
Klebensberger^{a*}

^aUniversity of Stuttgart, Institute of Biochemistry and Technical Biochemistry, 70569
Stuttgart, Germany

^bPhilipps-University Marburg, SYNMIKRO Research Center and Department of Chemistry,
35043 Marburg, Germany

^cRWTH Aachen University, Institute of Applied Microbiology-iAMB, 52074 Aachen, Germany

^dMax Planck Institute for Terrestrial Microbiology, 35043 Marburg, Germany

^eForschungszentrum Jülich, Institute of Bio- and Geosciences IBG-1: Biotechnology, 52425
Jülich, Germany

[†]Authors contributed equally

*Correspondence should be addressed to janosch.klebensberger@itb.uni-stuttgart.de and gert.bange@synmikro.uni-marburg.de

Materials and Methods

Bacterial strains and growth conditions. For cloning and expression *Escherichia coli* BL21 (DE3) was used and if not stated otherwise, cells were routinely grown in liquid LB medium at 37°C and 180 rpm shaking in a rotary shaker.¹ For plasmid maintenance and selection 40 µg/ml of kanamycin were supplemented to the growth media.

Library construction and evaluation. DNA-fragments of the *pedH* gene containing ends homologous to the SrfI and HindIII digested expression vector pMW10² were and NNK randomization at the desired positions (see **Figure 1b**) were synthesized by an external supplier (Synbio Technologies, USA). For library construction the pedMW10 vector was digested using SrfI and HindIII, purified and joined with the NNK-randomized DNA fragments using one-step isothermal assembly.³ The reaction product was subsequently transformed into *E. coli* BL21(DE3) cells and plated on LB-agar. A minimum of 2500 clones per library were subsequently suspended in LB-medium and stored as glycerol stocks (30% v/v) at -80°C until further usage. To evaluate library quality the plasmids from 56 individual clones were purified and the correctness was verified using Sanger sequencing. As around 20 % of the sequenced clones did not contain the correct insert, the screening size was increased accordingly.

Solid-phase screening assay. The solid phase screening assay to detect PQQ-ADH activity in cell colonies grown on nylon membranes was based on a previously developed screening assay for PQQ-ADHs in liquid cell cultures.⁴ In the final protocol 200 µL of a *E. coli* BL21(DE3) cell suspension ($OD_{600} = 3 \times 10^6$) were spread on a nylon membrane (pore size 0.45 µm, GVS Life Sciences) loaded LB_{Kan} agar plate supplemented with 100 µM PrCl₃. Upon incubation for 16 h at 37°C protein production

was induced by transferring the membranes were transferred onto new LB_{Kan} agar plates supplemented with 100 μ M PrCl₃, 10 μ M PQQ and 0.2% rhamnose. Upon incubation for 24 h at 16°C the membranes were washed placing them for 10 min on a round filter (Rotilabo Type 113A, Carl Roth GmbH) soaked in 3 ml 100 mM Tris buffer (pH 8). Upon drying on cellulose paper for 5 min, the washed membranes were transferred onto a new round filter that was immersed in 3 ml of a colorimetric enzyme activity assay solution (100 mM Tris buffer pH 8, 5 μ M PQQ, 5 μ M PrCl₃, 500 μ M phenazine methosulfate, 25 mM imidazole, 30 mM KCN, 10 mM substrate) and incubated in darkness under the hood for 1 – 24 h. Cell colonies producing PQQ-ADHs with activity towards the tested substrate were identified by a white halo.

Library screening. To guarantee with 80% certainty that each variant of the library is tested at least once, at least 1978 colonies (32 [NNK] x 32 [NNK] x 1.2 [correction for vectors without insert] x 1.61 [oversampling factor])⁵ per mutant library were screened for activity with 10 mM HMFA using the solid-phase activity assay (see solid-phase screening assay). Colonies that showed activity with HMFA were isolated on LB_{Kan} agar plates and reevaluated in triplicates in a second round of screening. Therefore one colony per identified clone was resuspended in 20 μ L H₂O and 3x 2 μ L were spotted in ~5 mm distance from each other on a nylon membrane loaded LB_{Kan} agar plate supplemented with 100 μ M PrCl₃. For comparison, also 3 x 2 μ L of PedH as well as EGFP producing cells were spotted on the same membranes. Cell growth, protein production and PQQ-ADH activity screening with 10 mM HMFA as substrate were performed as described above. Subsequently the plasmids were isolated from clones that showed increased activity with 10 mM HMFA in comparison to the PedH reference colonies and submitted for sequencing. The final evaluation of the identified clones was performed using the colorimetric enzyme activity assay with purified enzymes.

Molecular cloning for structural analysis and determination of kinetic parameters. The gene encoding PedH (PP_2679) was PCR amplified from genomic DNA of *Pseudomonas putida* KT2440 without the signal peptide (PedH28-595) using the following forward primer (5'- ttaaggtctcccatgGCTGTCAGCAATGAAGAAATCCTCCA-3') and reverse primer (5'- ttaaggtctcctcgagTTAgtggtgatggtgatgatgTGGCTTGACGCTTGCCG-3') containing a *NcoI* and *XhoI* restriction site and the coding sequence for a c-terminal hexa-histidine tag. The fragment was digested with *NcoI* and *XhoI* and cloned into pET24d(+) (Novagen) yielding in pET24d-PedH. Mutants have been cloned using Golden Gate Mutagenesis. The mutant fragments were amplified from pET24d-PedH using forward and reverse primers having the desired mutation and *BsaI* restriction site. All Golden Gate reactions were performed in a total volume of 15 µl. The final reaction volume contained 1-fold concentrated T4 ligase buffer (Promega, Madison, US). Prepared reaction mixtures (ligase buffer, acceptor plasmid, insert(s)) were adjusted to 13.5 µl with ddH₂O. In a final step, the corresponding enzymes were quickly added. First, a volume of 0.5 µl of *BsaI*-HF@v2 (10 units; New England Biolabs, Ipswich, US) and then 1 µl (1-3 units) of T4 ligase (Promega, Madison, US) was added. Golden Gate reactions were carried out by default under following conditions: a) Enzymatic restriction 37 °C (2 min); b) Ligation 16 °C (5 min) [10 passes each] and c) enzyme inactivation: 80 °C (20 min).

Protein production and purification. For initial screening of enzyme activity as well as biotransformation experiments, protein production and purification was performed as described elsewhere.² For enzyme kinetics and crystallography protein production and purification was performed as follows. Briefly; constructs were transformed in *E. coli* BL21 (DE3) (Novagen) for overexpression. Cells were grown in lysogeny-broth

(LB) medium, supplemented with 1 % lactose and kanamycin (50 mg/l). Cells were incubated at 30 °C overnight under rigorous shaking (180 rpm). Cells were harvested by centrifugation (3,500 x g, 20 min, 4 °C) and resuspended in 20 ml buffer A (20 mM HEPES-Na, pH 8.0, 500 mM NaCl, 20 mM KCl, 20 mM MgCl₂, 40 mM imidazole) before lysis in a M-110L Microfluidizer (Microfluidics). The lysate was cleared at 47,850 x g for 20 min at 4 °C and the supernatant was applied onto 5 ml HisTrap FF columns (GE Healthcare) for NiNTA affinity chromatography. After a wash step with 15 column volumes (CV) of buffer A, proteins were eluted with three CV of buffer B (20 mM HEPES-Na, pH 8.0, 500 mM NaCl, 20 mM KCl, 20 mM MgCl₂, 500 mM imidazole). Protein eluted fractions were pooled and treated with a final concentration of 100 mM EDTA prior to concentration in Amicon Ultra-10K centrifugal filters to 2.5 ml and further purified by size-exclusion chromatography (SEC). PedH was purified using a HiLoad 26/600 Superdex 200 column (GE Healthcare) equilibrated in buffer SEC (20 mM HEPES-Na, pH 7.5, 500 mM NaCl). Fractions containing PedH were pooled and concentrated for crystallization experiments.

Screening of enzyme activity

Initial enzyme activity measurements were performed in 96-well plates using 10 mM of substrate and 1 – 20 µg/ml enzyme following an established protocol with minor changes.² To represent the screening conditions, 5 µM PQQ instead of 1 µM PQQ and 5 µM PrCl₃ instead of 1 µM PrCl₃ were used.

Enzyme kinetics measurements. To be able to reach saturating substrate concentrations, a modified protocol was used to determine specific enzyme activities for the analysis of kinetic enzyme parameters. Shortly, 1 ml of assay solution containing 20 mM HEPES-Na (pH 8), 500 µM phenazine methosulfate (PMS), 150 µM

2,6-dichlorophenol indophenol (DCPIP), 25 mM imidazole, 50 μ M PrCl₃, 0.1 mM PQQ, and 0.2 μ M of enzyme. Addition of the enzyme to the reaction mixture started the measurement. Enzyme activity was calculated based on the change in OD₆₀₀ within the first minute upon substrate addition. Assays were performed in two (PedH^{F412V/W561A}/FFF) or three replicates (PedH/Ethanol, PedH^{F412V/W561A}/Ethanol, PedH^{F412V/W561A}/HMF, PedH^{F412V/W561A}/HMFA) and data are presented as the mean value with error bars representing the corresponding standard deviation. Kinetic parameters were obtained by fitting the enzyme activities at different substrate concentrations to the Michaelis-Menten equation. Kinetic values are presented as mean value with corresponding standard error.

Crystallization and structure determination. Crystallization was performed by the sitting-drop method at 20 °C in 0.5 μ l drops consisting of equal parts of protein and precipitation solutions. PedH wild type was co-crystallized at 250 μ M concentration with equimolar concentration of PQQ and metal of interest in 0.1 M sodium acetate pH 4.6 and 30 % (w/v) PEG 2000 MME. PedH^{F412V/W561A} was co-crystallized at 250 μ M concentration with equimolar concentration of PQQ and metal of interest within 24 h in 0.2 M Lithium sulfate, 0.1 M sodium cacodylate pH = 6.5, 30 % PEG 400. Prior data collection, crystals were flash-frozen in liquid nitrogen employing a cryo-solution that consisted of mother-liquor supplemented with 30 % (v/v) glycerol. Data were collected under cryogenic conditions at the DESY at beamline P14. Data were integrated and scaled with XDS and merged with XSCALE. Structures were determined by molecular replacement with PHASER, manually built in COOT⁶, and refined with PHENIX⁷. The structure of the PedH-PQQ-Metal complex was determined by molecular replacement using the crystal structures of ExaA of *Pseudomonas aeruginosa* (PDB-ID: 1FLG) as search models. Figures were prepared with PYMOL (Version 2.4.0).

Biotransformations and compound analysis. Biotransformations were performed as duplicates with 500 μ L reaction solution in sealed 1.5 ml reaction vials at 30°C and 180 rpm shaking. The reaction solution contained 100 mM Tris-HCl (pH 8), 5 μ M PQQ, 5 μ M PrCl₃, 150 μ M DCPIP, 500 μ M PMS, 25 mM Imidazol, 10 mM HMFA (substrate) as well as purified PedH or PedH^{F412V/W561A} protein ($c_{\text{end}} = 20 \mu\text{g/ml}$). Control reactions were performed without protein. In this setup, electrons are transferred from the active site of the enzyme to the electron mediator PMS and eventually to DCPIP, which itself is slowly re-oxidized by oxygen.⁸ Probes were incubated in the dark to reduce light-induced decomposition of PMS.⁹ Samples were collected at several time points, filtered and stored at -80°C before product analysis. Furan quantification was performed by HPLC analysis using a Beckman System Gold 126 Solvent module with a 168 diode 201 array detector (Beckman Coulter, Brea; USA) and a SUPELCOSIL™ LC-8-DB HPLC column (Supelco, Bellefonte, USA). Column was tempered to 40°C. As eluent, a binary mix of 100% acetonitrile and 20 mM KH₂PO₄ with 1% acetonitrile (adjusted pH = 7.0, degassed) was used at a flow rate of 0.8 mL min⁻¹. Elution started with an increasing gradient of acetonitrile from 0% to 5% within 3.5 minutes. Acetonitrile gradient increased again from 5% to 40% in the next 2.5 minutes. Afterwards the column was flushed with 20 mM KH₂PO₄ with 1% acetonitrile (adjusted pH = 7.0, degassed) for 2 minutes. UV detection was performed at 230 nm. If needed each compound was detected at distinct wavelengths to separate overlapping peak areas. FDCA shows a signal 264 nm, HMFA at 251nm, FFA at 289 nm, 2,5-Bis(hydroxymethyl)furan (HMFOH) at 225 nm and HMF at 285 nm. Retention times of furan compounds were 2.62 minutes, 2.83 minutes and 2.13 minutes for HMFA, FFA and FDCA, respectively. Further compounds HMF and HMFOH had retention times of 5.35 minutes and 4.4 minutes.

Table S1: Composition of the individual screened PedH mutant libraries.

Library	Mutated residues
1	A556 + W561
2	F412 + W561
3	F412 + A556
4	L455 + W561
5	F412 + L455
6	F459 + W561
7	F412 + F459
8	I461 + F412
9	I461 + L455
10	I461 + F459
11	I461 + A556
12	I461 + W561

Table S2: Correlation matrix of active site and substrate channel residues extracted from 3DM-database of PQQ-dependent alcohol dehydrogenases ($1 \triangleq 100\%$ and $0 \triangleq 0\%$ coevolution of two distinct alignment positions in 3DM-database). Combinations of residues that were selected for mutant library generation are colored in red.

Position	W285	F412	L413	L455	F459	I461	A556	W561
W285	-	0.14	0.11	0.19	0.15	0.24	0.18	0.19
F412	0.14	-	0.36	0.77	0.74	0.88	0.92	0.79
L413	0.11	0.36	-	0.32	0.29	0.39	0.36	0.32
L455	0.19	0.77	0.32	-	0.71	0.84	0.84	0.74
F459	0.15	0.74	0.29	0.71	-	0.78	0.76	0.74
I461	0.24	0.88	0.39	0.84	0.78	-	0.93	0.78
A556	0.18	0.92	0.36	0.84	0.76	0.93	-	0.79
W561	0.19	0.79	0.32	0.74	0.74	0.78	0.79	-

Table S3: Crystallographic data collection and refinement statistics for PedH and PedH^{F412V/W561A}.

	PedH	PedH ^{F412V/W561A}
Data collection		
Space group	P4 ₃ 2 ₁ 2	P4 ₃ 2 ₁ 2
Resolution range (Å)	47.81 - 1.648 (1.707 - 1.648)	46.71 - 1.704 (1.765 - 1.704)
Unit cell parameters		
<i>a</i> , <i>b</i> , <i>c</i> (Å)	105.28, 105.28, 187.13	105.53, 105.53, 186.88
α , β , γ (°)	90, 90, 90	90, 90, 90
<i>R</i> _{merge}	0.2083 (3.522)	0.175 (2.196)
Average <i>I</i> / σ (<i>I</i>)	14.23 (1.11)	15.92 (1.66)
No. of total reflections	3378794 (330606)	3110956 (307001)
Completeness (%)	99.84 (98.85)	99.97 (99.91)
CC _{1/2} (%)	0.999 (0.492)	0.999 (0.677)
Refinement		
<i>R</i> _{work}	0.1473 (0.2669)	0.1420 (0.2431)
<i>R</i> _{free}	0.1592 (0.2833)	0.1606 (0.2683)
No. of atoms		
Overall	5028	4958
Protein	4384	4341
Ligands	26	32
Water	618	585
Average B-factor(Å²)		
Overall	27.6	24.40
Protein	25.98	22.96
Ligands	19.51	23.26
Water	39.38	35.17
Root-mean-square deviation		
Bond lengths (Å)	0.011	0.017
Bond angles (°)	1.42	1.41
Ramachandran plot (%)		
Favored	95.89	96.07
Allowed	3.57	3.39
Outliers	0.54	0.54

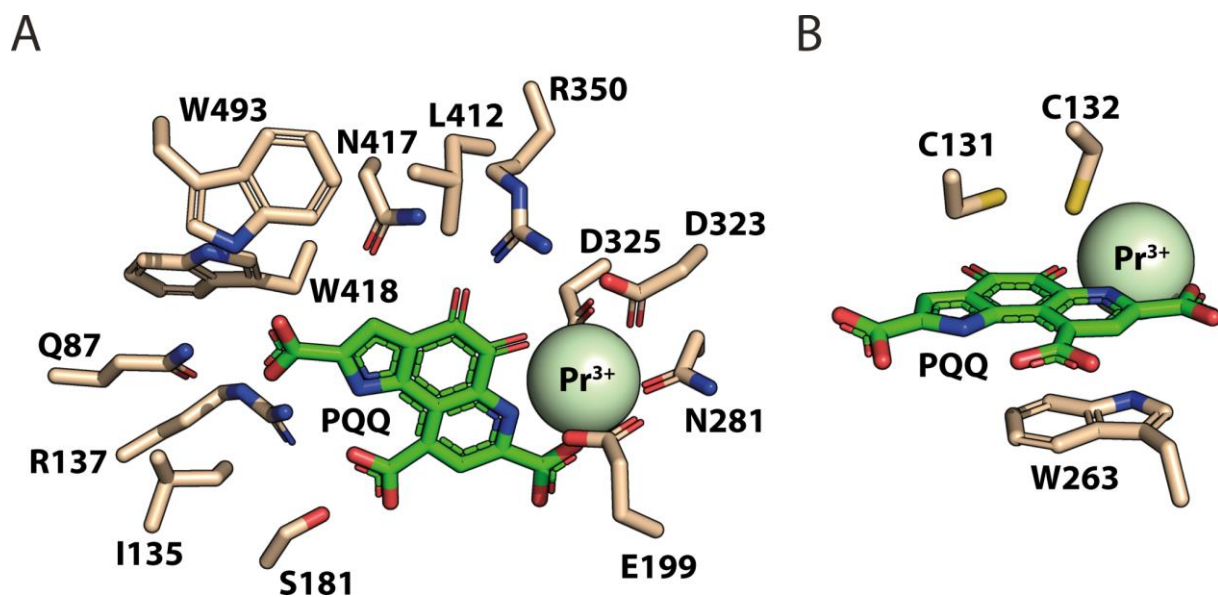


Figure S1: Coordination of PQQ in the active site of PedH. **A)** Top view depicting residues in the same plane as PQQ and the 4 residues coordinating the metal praseodymium. **B)** Side view depicting the stacking of PQQ between W263 and the disulfide bridge between C131 and C132.

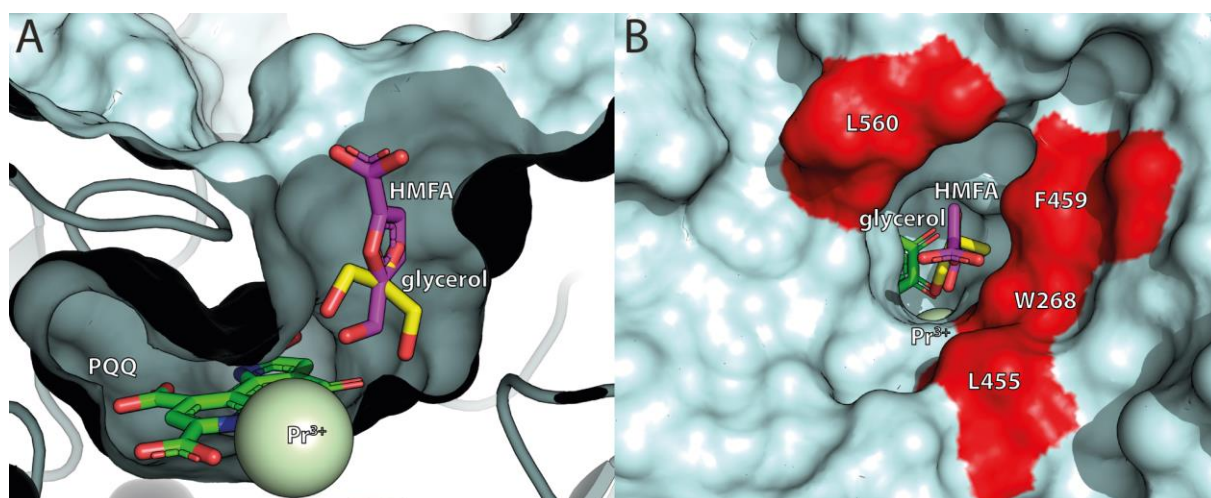


Figure S2: **A)** Cutaway of the active site of PedH^{F412V/W561A}. HMFA (purple) is superimposed onto glycerol (yellow) and would fit into the widened substrate channel of the variant. **B)** Top-view of the active site of PedH^{F412V/W561A} with HMFA (purple) superimposed onto glycerol (yellow). Surface of amino acid residues pointing to the carboxyl group of HMFA that are not part of the catalytic mechanism are colored in red.

References

- (1) Maniatis, T.; Fritsch, E.; Sambrook, J.; Laboratory, C. S. H. *Molecular Cloning: A Laboratory Manual*; Cold Spring Harbor, N.Y. Cold Spring Harbor Laboratory, 1982.
- (2) Wehrmann, M.; Billard, P.; Martin-Meriadec, A.; Zegeye, A.; Klebensberger, J. Functional Role of Lanthanides in Enzymatic Activity and Transcriptional Regulation of Pyrroloquinoline Quinone-Dependent Alcohol Dehydrogenases in *Pseudomonas Putida* KT2440. *MBio* **2017**, *8* (3), e00570-17. <https://doi.org/10.1128/mBio.00570-17>.
- (3) Gibson, D. G. Enzymatic Assembly of Overlapping DNA Fragments. *Methods Enzymol.* **2011**, *498*, 349–361. <https://doi.org/10.1016/B978-0-12-385120-8.00015-2>.
- (4) Wehrmann, M.; Klebensberger, J. Engineering Thermal Stability and Solvent Tolerance of the Soluble Quinoprotein PedE from *Pseudomonas Putida* KT2440 with a Heterologous Whole-Cell Screening Approach. *Microb. Biotechnol.* **2018**, *11* (2), 399–408. <https://doi.org/10.1111/1751-7915.13036>.
- (5) Reetz, M. T.; Kahakeaw, D.; Lohmer, R. Addressing the Numbers Problem in Directed Evolution. *ChemBioChem* **2008**, *9* (11), 1797–1804. <https://doi.org/10.1002/cbic.200800298>.
- (6) Emsley, P.; Cowtan, K. Coot: Model-Building Tools for Molecular Graphics. *Acta Crystallogr. D. Biol. Crystallogr.* **2004**, *60* (Pt 12 Pt 1), 2126–2132. <https://doi.org/10.1107/S0907444904019158>.
- (7) Adams, P. D.; Afonine, P. V.; Bunkóczi, G.; Chen, V. B.; Davis, I. W.; Echols, N.; Headd, J. J.; Hung, L.-W.; Kapral, G. J.; Grosse-Kunstleve, R. W.; McCoy, A. J.;

- Moriarty, N. W.; Oeffner, R.; Read, R. J.; Richardson, D. C.; Richardson, J. S.; Terwilliger, T. C.; Zwart, P. H. PHENIX: A Comprehensive Python-Based System for Macromolecular Structure Solution. *Acta Crystallogr. D. Biol. Crystallogr.* **2010**, 66 (Pt 2), 213–221. <https://doi.org/10.1107/S0907444909052925>.
- (8) Naumann, R.; Mayer, D.; Bannasch, P. Voltammetric Measurements of the Kinetics of Enzymatic Reduction of 2,6-Dichlorophenolindophenol in Normal and Neoplastic Hepatocytes Using Glucose as Substrate. *Biochim. Biophys. Acta - Mol. Cell Res.* **1985**, 847 (1), 96–100. [https://doi.org/10.1016/0167-4889\(85\)90158-2](https://doi.org/10.1016/0167-4889(85)90158-2).
- (9) Jahn, B.; Jonasson, N. S. W.; Hu, H.; Singer, H.; Pol, A.; Good, N. M.; Op den Camp, H. J. M.; Cecilia, D. C. N.; Gomez, M.; Daumann, L. Understanding the Chemistry of the Artificial Electron Acceptors PES , PMS , DCPIP and Wurster ' s Blue in Methanol Dehydrogenase Assays. *JBIC J. Biol. Inorg. Chem.* **2020**, No. 0123456789. <https://doi.org/10.1007/s00775-020-01752-9>.